SLAC – 294
UC – 34D
(E)

MEASUREMENTS OF CHARGED TWO–PARTICLE EXCLUSIVE STATES IN PHOTON–PHOTON INTERACTIONS*

Robert Preston Johnson

Stanford Linear Accelerator Center
Stanford University
Stanford, California 94305

March 1986

Prepared for the Department of Energy
under contract number DE-AC03-76SF00515

Printed in the United States of America. Available from the National Technical Information Service, U.S. Department of Commerce, 5285 Port Royal Road, Springfield, Virginia 22161. Price: Printed Copy A12, Microfiche A01.

* Ph.D. Dissertation.

Abstract

A description is given of an experiment performed at the *PEP* electron-positron storage ring, using the DELCO detector, to measure the formation of charged particle pairs from interactions of pairs of virtual photons radiated from the colliding electron beams. The final states which are measured are electron-positron pairs, charged pion pairs, charged kaon pairs, and proton pairs.

Electron-positron pairs are separated from other data by use of gas Čerenkov counters. The shapes of all kinematic distributions are found to agree with predictions of quantum electrodynamics. These data also are used as an accurate normalization for subtraction of the muon-pair background and for measurement of the cross sections of the three hadronic channels.

Pion pairs are measured in the mass range from 0.6 to 2.0 GeV, where production of the $f\,(1270)$ resonance is observed to interfere with significant continuum production. The continuum is well described by single-pion exchange, allowing a measurement of the f two-photon partial width of $3.47 \pm 0.37\,\mathrm{keV}$. No *a priori* assumption is made about the ratio of helicity amplitudes, and the phenomenological model used in fitting the data is constrained to satisfy elastic unitarity. If unitarity is not required, then the fitted partial width is a factor of 0.83 lower than the quoted value. The Q^2 dependence of the cross section is found to be consistent with predictions of the Generalized Vector Dominance Model.

Kaon pairs and proton pairs are identified by time-of-flight measurements. Kaon pairs are measured in the mass range from 1.3 to 2.0 GeV, where production of the $f'\,(1520)$ resonance is observed. The continuum background is estimated by extrapolation, allowing a measurement of the f' two-photon partial width of $0.07 \pm 0.04\,\mathrm{keV}$. The ratio of the f and f' two-photon partial widths is found to be consistent with $SU(3)$ quark model predictions with a mixing angle of 28 ± 4 degrees. Twenty-three proton pairs are observed, and the average cross section for their production from photon-photon collisions in the mass range from 2.2 to 2.9 GeV is measured over the angular range $-0.6 < \cos\theta < 0.6$ to be $1.2 \pm 0.5\,\mathrm{nb}$.

Acknowledgements

The experiment described in this thesis has been made possible by the combined efforts of many people. The DELCO collaboration consists of 38 physicists in addition to myself: W.B. Atwood, P.H. Baillon, B.C. Barish, G.R. Bonneaud, A. Courau, H. DeStaebler, G.J. Donaldson, R. Dubois, M.M. Duro, E.E. Elsen, S.G. Gao, Y.Z. Huang, G.M. Irwin, H. Kichimi, J. Kirkby, D.E. Klem, D.E. Koop, J Ludwig, G.B. Mills, A. Ogawa, T. Pal, D. Peret-Galix, R. Pitthan, D.L. Pollard, C.Y. Prescott, L.Z. Rivkin, L.S. Rochester, W. Ruckstuhl, M. Sakuda, S.S. Sherman, E.J. Siskind, R. Stroynowski, R.E. Taylor, S.Q. Wang, S.G. Wojcicki, H. Yamamoto, W.G. Yan, and C.C. Young. I thank all of these individuals for their efforts and devotion to the experiment, for helping me with many problems that I have encountered, and in general for the pleasant experience I have had working with them at SLAC. I would like to give special thanks to Bill Atwood for his unfailing enthusiasm for the experiment and associated physics analyses and for the special efforts he has made to assist me; to Hobie DeStaebler for many helpful discussions at points of impasse in my work; and to Eckhard Elsen for all the help and encouragement he has given me and for a very special friendship. I am especially grateful to my thesis advisor, Prof. Charles Prescott, for steering me toward this thesis topic, for his encouragement and guidance during difficult times, and for seeing my graduate work through to completion.

I would like to acknowledge the support for DELCO by the technical staffs of SLAC, groups A and G, and CalTech: B. Bricaud, A. Johnson, O. Saxton, S. Sund, J. Zingheim, D. Chambers, D. Ouimette, C. Pierce, D. Porat, M Susskind, A. Tillman, R. Cooper, L. Cronk, R. Decker, H. Grau, J. Hanson, L. Mossbarger, D. Sell, S. Sondergaard, and J. Ungerer. Without their work, this experiment would not have been possible. I am equally indebted to the *PEP* Storage Ring Division for providing the hundreds of hours of stable colliding beams necessary for successful data taking.

The DELCO experiment is supported through CalTech and SLAC by the

U.S. Department of Energy and the National Science Foundation. The data have been analyzed with the IBM computers of SLAC Computing Services. Most of the figures were made with the program *Top Drawer* by R.B. Chaffee, and the typesetting was accomplished with the TEX typesetting program of Donald E. Knuth, using the PSIZZL macros of Arthur Ogawa for the format.

This work would not have been possible without the initiative and experience of André Courau, who as a visitor from *Laboratoire de l'Accelerateur Lineaire* of France launched the DELCO analysis of two-photon channels and guided me in my work up through the time of publication of our first results. I also give special thanks to Gerard Bonneaud and Steve Sherman, who contributed directly to the analysis of two-photon channels and assisted me in many ways, to Prof. Frederick Gilman for several useful discussions about theoretical aspects of two-photon interactions, and to René Ong for helping to proofread the manuscript.

Finally, I would like to thank all of my friends who have made my time at Stanford a most pleasant experience. I especially thank my parents for their continual support and encouragement and my wife, Mayumi, and son, Kent, for the love and joy that they have given to me during the course of this work.

Table of Contents

List of Tables

List of Figures

1. The Two-Photon Particle Production Process

1.1 Introduction

The quantum theory of electrodynamics (QED) predicts that photons, the quanta of the electromagnetic field, will interact with each other through the exchange of virtual electron pairs—a phenomenon which necessarily is absent in the classical field theory of Maxwell. However, such processes are not observed from usual sources of electromagnetic radiation because the cross sections are prohibitively small except at photon energies well above the electron mass. But in the energy realm of modern accelerators, interest in photon-photon interactions goes well beyond the relatively simple QED processes. Photons interact with many particles other than electrons, so at high energies many possibilities are expected for two-photon interactions, with hadrons as well as leptons in the final state.

Unfortunately, there are no sources of free, massless photons in the energy ranges of interest to high energy particle physics which are intense enough to produce observable photon-photon collisions. Instead, such collisions always have been studied indirectly as interactions of virtual photons. The first methods to be used, such as the Primakov effect for two-photon production of π^0 and η, involve the interaction of high energy photons with stationary atoms. An incident photon interacts with a virtual photon from the electromagnetic field around the atomic nucleus to produce a π^0, for example. A more recent method, and the one most widely used, involves the use of the high intensity electron-positron colliding beams available in present-day storage rings.

The most simple process by which two oppositely charged electrons can interact to produce a hadronic final state is through annihilation into a single virtual photon with an energy equal to twice the beam energy. That is contrasted with the process of interest to two-photon physics, in which a photon is radiated by each beam. Schematic diagrams for both processes are shown in Fig. 1.1. The second is of higher order in the small electron-photon coupling than the first, but the cross sections for two-photon processes can be very large in spite of that.

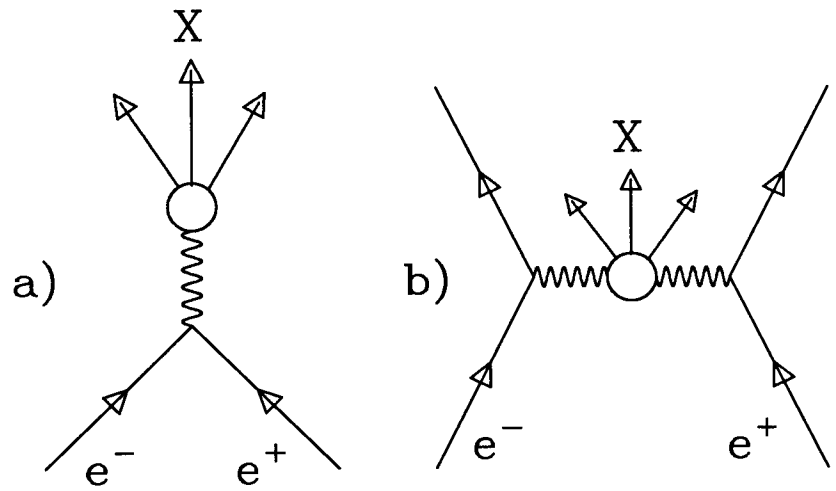

Figure 1.1. Production of non-leptonic final states in e^+e^- collisions. Two possibilities: (a) single-photon production and (b) two-photon production.

The reason is that single-photon production requires a spacelike photon with a mass equal to twice the beam energy, while the two-photon process proceeds with timelike photons of generally lower energy and very low mass. Thus the two-photon processes can have relatively large cross sections in certain kinematic regions. In particular, the two-photon process favors the production of states X which have much lower energies than are available in single-photon annihilation. Also, the two processes produce states with differing quantum numbers, so they are in many respects complimentary. For example, the two-photon states have positive C-parity, while for single-photon production the C-parity is negative. Also, a single photon always has spin-one and parity negative, while two photons can couple to resonances with a variety of spin-parity combinations.

Since two-photon collisions at e^+e^- storage rings are dominated by interactions of photons of low invariant mass (small Q^2), they resemble the interaction of two real photons. The electron beams act essentially as intense sources of bremsstrahlung radiation, which interact as would two beams of high energy photons. This line of thought is developed mathematically in Chapter 2, where we

calculate the spectrum of colliding photon pairs expected from an e^+e^- storage ring and thereby justify the statements made here regarding the scales of Q^2 and energy involved in the photon-photon collisions.

DELCO is an experiment which has taken data at the *PEP* electron-positron storage ring of the Stanford Linear Accelerator Center (SLAC). The emphasis of the detector is on tracking and identification of charged particles. In the momentum range pertinent to two-photon physics, electrons are identified by a threshold gas Čerenkov counter, and charged kaons and protons are identified by time-of-flight measurements. For both identification methods, a measurement of the particle momentum is essential, and that is made by drift chambers positioned within a magnetic field. A more complete description of the detector and its performance is given in Chapter 3.

The detector components used for particle tracking and identification cover about 60% of the solid angle, in a region centered about a plane perpendicular to the beam line. That is not sufficient for studies of inclusive particle production, especially since the two-photon state is preferentially boosted along the direction of the beam, causing most of the particles to escape out the ends of the detector. The detector is suitable for studies of exclusive states of low multiplicity, where all of the particles produced from the two-photon interaction are detected and identified. In particular, the ability of the detector to identify low momentum electrons gives special advantages in the study of two-photon interactions which produce only two stable particles in the final state. In this thesis, the reaction channels which are studied are

$$e^+e^- \rightarrow e^+e^-e^+e^-,$$
$$e^+e^- \rightarrow e^+e^-\pi^+\pi^-,$$
$$e^+e^- \rightarrow e^+e^-K^+K^-,$$
$$\text{and} \quad e^+e^- \rightarrow e^+e^-p\bar{p}.$$

For the QED channel, the kinematic distributions measured from data are compared in shape with theoretical calculations. Also, the QED channel is used as

an accurate normalization for subtraction of the $e^+e^- \to e^+e^-\mu^+\mu^-$ background from the remaining data and for measurements of the cross sections of the hadronic channels. In the $\pi^+\pi^-$ channel the two-photon partial width of the $f\,(1270)$ resonance is measured, and in the K^+K^- channel the two-photon partial width of the $f'\,(1525)$ is measured. As the measurements of these partial widths is a principle object of this research, this chapter concentrates on discussing the meaning of the two-photon partial width and its theoretical significance. Chapter 7 elaborates at length on the specific theoretical models used in the analysis of the $\pi^+\pi^-$ channel.

1.2 Hadron Production from Photon-Photon Interactions

Since hadrons are believed to be composed of point-like charged quarks, the interactions of photons with hadrons should ultimately be described by a QED type of coupling of photons to spin-$\frac{1}{2}$ point fermions. The interactions of the quarks among themselves should then be described by Quantum Chromodynamics (QCD), in which the strong interactions are mediated by vector bosons called gluons, with additional small contributions from electromagnetic and weak effects. However, we know that hadrons are tightly bound within regions with dimensions smaller than $1\,\text{fermi} = 5\,\text{GeV}^{-1}$. Therefore, it is clear than a photon must have an energy much greater than 0.2 GeV before it could effectively resolve any of the detailed structure of a hadron.† Otherwise, it may be best to consider a physical description of photons coupling to point hadrons, with the addition of some form factor to describe deviations from point-like behavior. In principle, the form factor might be calculable from QCD; however, all that is possible at this point in time is to calculate perturbative expansions which are valid only at very short distances in space-time. Thus it is consistent to calculate scattering amplitudes in which photons couple to quarks and quarks interact through gluon exchange, but only if

† That is not to say that the hadron structure cannot have a large effect on the strength of the coupling to photons. In fact, it is important, especially when the hadron is neutral, as we will see in Section 1.5.

all of that takes place on a very small time and distance scale. What that means is that the wavelengths of the photons must be small on the scale of a hadron, and there must be a large momentum transfer between photons and quarks.

Even then, after such a hard-scattering interaction occurs, the quarks remaining in the final state continue to interact over a long time interval, and the interaction, in fact, grows stronger as they separate from the point of collision with the photons. So one can not get away from the fact that the low-energy non-perturbative strong interaction effects must be modeled phenomenologically. The best that one can hope for is a factorization of the hard-scattering effects from the non-perturbative part, so that they may be dealt with separately, and even measured separately to some extent. That has been done for the production of hadron pairs by two real photons by Brodsky and Lepage[1] and extended to include virtual photons by Gunion, Millers, and Sparks.[2] If the hadron pairs are observed at large angles with respect to the incoming beams, which is experimentally necessary for most present experiments, anyway, then for sufficiently large two-photon invariant mass, the photon energies and the momentum transfer are large enough that the perturbation expansion and factorization make sense. The first available experimental results indicate agreement, of low statistical precision, with the theory for pion pairs[3,4] and kaon pairs,[5] for pair masses as low as 1.5 GeV for kaons and 2.0 GeV for pions.

In any case, DELCO is restricted by its methods of particle identification to pair masses below 2 GeV (or 3 GeV for proton pairs). Therefore, in the DELCO data neither do the photons have enough energy to finely resolve hadronic structure nor is QCD perturbation theory valid. Instead, the hadrons and hadron resonances must be considered to be the elementary particles, and their couplings to photons and to other hadrons are described according to phenomenology which is well known from low-energy (by today's standards) hadron physics. For the $\pi^+\pi^-$ final state, the relevant phenomenology is presented in Chapter 7.

1.3 Resonance Formation

The energy range accessible to DELCO is, in fact, dominated by resonant effects from the $f\,(1270)$ in the $\pi^+\pi^-$ channel and the $f'\,(1525)$ in the K^+K^- channel. These resonances both represent tensor mesons of zero isospin and have been studied extensively in purely hadronic interactions. They are closely related to an isovector tensor meson called the A_2 (1320). Some of the information already known about the three is shown in Table 1.1.

Table 1.1. Particle properties for the tensor mesons. The data are taken from Ref. 6 and represent averages of many experimental results, except for the f' branching ratio to $\gamma\gamma$, which is from Ref. 7, the only published measurement to date. No DELCO results are included.

Particle	$I^G(J^P)C$	Mass (MeV)	Width (MeV)	Decay mode	Fraction %
f	$0^+(2^+)+$	1274	178	$\pi\pi$	84.3±1.2
		±5	±20	$\pi^+\pi^-\pi^+\pi^-$	2.9±0.4
				$K\overline{K}$	2.9±0.2
				$\gamma\gamma$	0.0015±0.0002
A_2	$1^-(2^+)+$	1318	110	$\rho\pi$	70.1±2.2
		±5	±5	$\eta\pi$	14.5±1.2
				$\omega\pi\pi$	10.6±2.5
				$K\overline{K}$	4.9±0.8
				$\pi\gamma$	0.27±0.06
				$\gamma\gamma$	0.00075±0.00016
f'	$0^+(2^+)+$	1525	70	$K\overline{K}$	dominant
		±5	±10	$\gamma\gamma$	0.00016±0.00006

The cross section for producing a resonance X from two photons is proportional to its two-photon partial width $\Gamma_{\gamma\gamma}$. Also, the probability for a resonance to decay into two photons is proportional to $\Gamma_{\gamma\gamma}$. So if the total width of the

resonance is represented by Γ, then the two-photon partial width is related to the branching ratio to two photons by $\Gamma_{\gamma\gamma} = \mathrm{BR}(X \to \gamma\gamma) \cdot \Gamma$. Thus the two-photon partial widths of the tensor mesons are, according to Table 1.1,

$$\begin{aligned} \Gamma_{f\to\gamma\gamma} &= 2.7 \ \pm 0.3 \ \text{keV} \\ \Gamma_{A_2\to\gamma\gamma} &= 0.82 \pm 0.18\,\text{keV} \\ \Gamma_{f'\to\gamma\gamma} &= 0.11 \pm 0.05\,\text{keV}. \end{aligned} \tag{1.1}$$

These values all have been measured by two-photon production at e^+e^- storage rings, so they all suffer from the same kinds of systematic effects as do the DELCO measurements. For example,

- The measurements are made with virtual photons, so an extrapolation must be made to $Q^2 = 0$. We will see that for the usual experimental situation this effect is small.
- Generally the resonance is not produced in isolation. Usually there is substantial continuum production which interferes with the resonant effects, and it must be modeled properly in order to extract the resonant cross section.
- The tensor mesons have widths which are large on the scale of the typical experimental resolution. Therefore, the energy dependence of the cross section must be appropriately modeled, leading to partial widths which are not constant with energy. One must be careful to understand how the final number given for the partial width is defined. This is closely related to the previous point—interference with a background would be no problem if the width were negligibly small.
- A tensor meson may be produced from photon pairs with a total helicity of either zero or two with respect to the axis along which the photons travel in the center-of-mass system. Therefore, the angular distribution of the decay products is not known *a priori* but depends on dynamics of the production. This problem is discussed at length in the following section.

- Most experiments have not been optimized for studying the relatively low energy two-photon production processes. This complicates the always difficult problem of understanding the detection efficiency.

1.4 Angular Distributions of Tensor Meson Decays

Consider a spin-2 meson in its rest frame with spin component $\lambda = 0, \pm 1, \pm 2$ in the z direction. When it decays into two spin-0 mesons, the angular distributions are given by the squares of d-functions, $d^J_{\lambda 0}(\theta)$, where θ is the angle between the momentum of one of the decay products and the z axis. Figure 1.2 shows plots of the three angular distributions, using

$$\begin{aligned} d^2_{00}(\theta) &= \tfrac{3}{2}\cos^2\theta - \tfrac{1}{2} \\ d^2_{10}(\theta) &= -\sqrt{\tfrac{3}{2}}\sin\theta\cos\theta \\ d^2_{20}(\theta) &= \tfrac{\sqrt{6}}{4}\sin^2\theta\,. \end{aligned} \tag{1.2}$$

Also shown is the shape of the experimental acceptance for pairs produced at the angle θ in the meson rest system, assuming that the mesons are produced by $\gamma\gamma$ collisions in an e^+e^- storage ring and observed by a detector with a laboratory acceptance of $\cos\theta_{\rm lab} < 0.6$ (appropriate for DELCO).

If the experiment is done with photons which are almost real, as is usually the case, then tensor mesons can be produced only with helicity $\lambda = 0$ or 2, assuming an axis of quantization parallel to the photon momenta in the center-of-mass system. Unfortunately, the angular distributions for these two possibilities are rather similar in shape in the experimental region of greatest acceptance, so the experiment is severely limited in determining the fraction of each component in the data. If that fraction is incorrect, then it is clear that an extrapolation to the full solid angle, which is necessary to determine the two-photon partial width of the meson, can be greatly in error, since the two angular distributions are not at all similar near $\cos\theta = \pm 1$. Therefore, it is useful to have some knowledge of

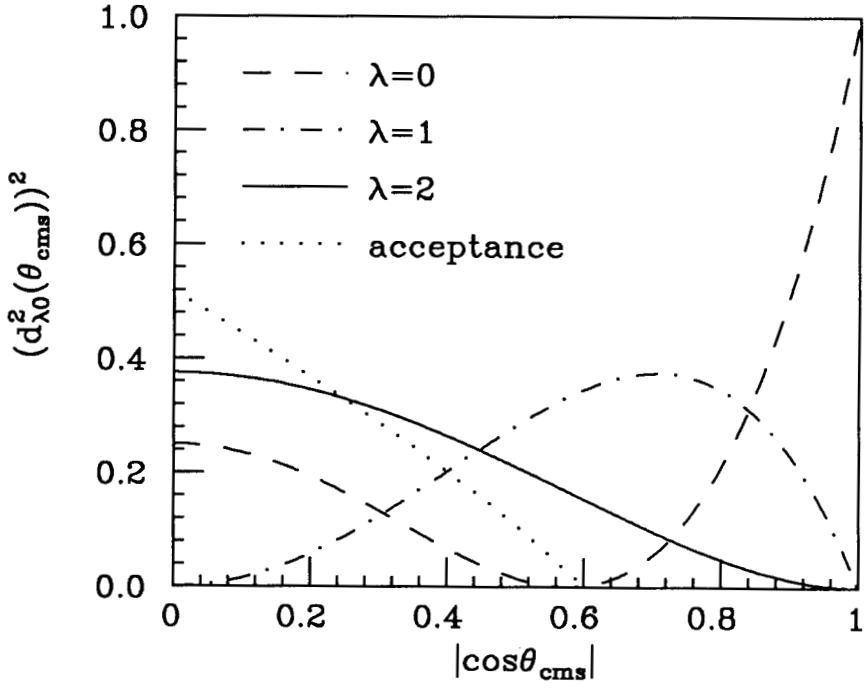

Figure 1.2. Angular distributions for the decay of a tensor meson into two spin-zero mesons for helicities $\lambda = 0, 1, 2$. Also shown is the shape of the acceptance of the DELCO detector.

the ratio of the helicity amplitudes either from theory or from other experiments with greater angular acceptance.

The Crystal Ball collaboration, using a detector with a maximum acceptance of 98% of the solid angle, measured the angular distribution for $\gamma\gamma \to f \to \pi^0\pi^0$ within the limit $|\cos\theta| < 0.9$ and determined that[9]

$$\frac{\Gamma^{\lambda=0}_{\gamma\gamma}}{\Gamma^{\lambda=2}_{\gamma\gamma}} = 0.12 \pm 0.39\,. \tag{1.3}$$

Theoretical limits are even more stringent. In Ref. 10, elastic $\gamma\gamma$ scattering is considered, and a sum rule is derived from fixed-t dispersion relations by invoking crossing symmetry. When partial wave expansions are inserted into the sum rule, with the partial wave amplitudes approximated by a series of narrow resonance

contributions, then the following inequality is obtained:

$$\sum_T \frac{g^2_{T\to\gamma\gamma}(\lambda=2)}{m_T^8} \geq 6\sum_T \frac{g^2_{T\to\gamma\gamma}(\lambda=0)}{m_T^8} + \text{positive } J^P = 4^+ \text{ contributions,} \tag{1.4}$$

where the sums are over all of the tensor mesons. Because of the factors of $1/m_T^8$, only the f, f', and the A_2^0 contribute significantly, and from quark-parton-model predictions, one expects the main contribution to be from the f. Therefore, the f partial width into $\gamma\gamma$ with helicity-zero is expected to be suppressed by at least a factor of six relative to the helicity-two partial width.

The authors of Ref. 8 and Ref. 5 claim that a six-to-one suppression of the helicity-zero amplitude may be calculated from Clebsch-Gordan vector coupling coefficients. They show that *if* the $\gamma\gamma$ system is presumed to have an angular momentum given by only the sum of the photon spins, then the $J = 2$, $M = 0$ component of the $\gamma\gamma$ system is six times smaller than the $J = 2$, $M = 2$ component. But that says nothing about how strongly the meson couples to the two helicity amplitudes. The two-photon width is a dynamical quantity related to the tensor meson structure.

We describe the photon pair and pseudoscalar-meson pair by helicity states because that is a proper and convenient description of a pair of relativistic particles. For $J = 2$ there are five such states, but symmetry requires that the coupling be the same for $+\lambda$ as for $-\lambda$, leaving only three independent amplitudes for an interaction. In a nonrelativistic case, one might find it convenient to make an LS decomposition and describe the two-particle state by the total spin s and the orbital angular momentum l, such that $\vec{J} = \vec{s} + \vec{l}$. One easily can see that for $J = 2$ there are five possible combinations of s and l. Symmetry must again reduce the number of independent couplings to three, but it no longer is so obvious. Hence we talk in this case of some sort of orbital angular momentum amplitudes rather than helicity amplitudes. One could make the *dynamical* assumption that only $l = 0$ contributes, but some sort of justification must be given. Then the

number of amplitudes would be reduced to one. But when the relativistic regime is approached, it does not seem to be of any greater advantage to make an *ad hoc* assumption that $l = 0$ than to assume that $\lambda = 2$. Furthermore, it is a fact that an LS decomposition cannot be made for a pair of massless particles such as photons (see Section 7.1).

Finally, let us consider what modifications of these ideas are necessary for an experiment done with virtual photons. We wish to measure the two-photon widths of tensor mesons for real photons, which requires a small extrapolation of the result obtained from scattering of photons generated by colliding electron beams. For real photons, the helicity-one amplitude is exactly zero, but it is possible for experiments done with quasi-real photons to see some contribution from helicity-one *in addition* to the helicity-zero and helicity-two contributions. In making the extrapolation to real photons, one would want to isolate the helicity-one contribution and drop it. We will not be concerned about this problem, though. First of all, the $\gamma\gamma$ collisions observed by DELCO are from photons which are sufficiently close to being real that the helicity-one component must already be negligibly small.† Second, it is clear from Fig. 1.2 that the acceptance of DELCO is small for the helicity-one component, relative to the others, so not much of that component would be observed even if it were produced.

1.5 Unitary Symmetry and the Tensor Meson Nonet

The theoretical importance of the two-photon width of a meson stems from the general utility of electromagnetic probes. At a fundamental level, photons are known to couple only to charged particles, and the nature of the coupling is known in full detail from QED. Therefore, the only missing information about how the meson is produced from photons is the detailed structure of charged currents within the meson. The structure depends upon the composition of the meson and the strong interactions of its constituents, and it is what is of theoretical interest.

† That is, for the untagged experiment (see Chapter 2).

The most basic theoretical model is the quark-parton model, which assumes that each meson is composed of two spin-$\frac{1}{2}$ quarks of flavor u, d, or s. The only dynamical assumption made is that of (slightly broken) $SU(3)$ symmetry under transformations of isospin and hypercharge. The u, d, and s quarks form a $\mathbf{3}$ representation of $SU(3)$, and their antiparticles form a $\overline{\mathbf{3}}$ representation, as shown in the weight diagrams of Fig. 1.3. The mesons are formed from combinations of quark and antiquark. Superimposing the two weight diagrams immediately generates the nine possible combinations of the I and Y quantum numbers, but there is an additional quantum number, spin, which must be considered. Spin singlet states are formed when the quark and antiquark have their spins anti-parallel, yielding the pseudoscalar nonet (η, η', π, K), while the vector nonet $(\phi, \omega, \rho, K^*)$ is formed when the spins are parallel. The intrinsic spin of the quarks should not be the only source of angular momentum, so we expect higher spin states. The $J = 2$ nonet has been observed, and the particles of which it is composed are shown in Fig. 1.3. We can consider these mesons to be composed of massive spin-$\frac{1}{2}$ quarks in a P-wave state of relative angular momentum.

The $\mathbf{3} \otimes \overline{\mathbf{3}}$ representation of Fig. 1.3 may be reduced to a combination of octet and singlet irreducible representations, $\mathbf{8} \oplus \mathbf{1}$. The charge neutral A_2 obviously is a member of the octet. It is represented in terms of the direct product quark-pair states by

$$|A_2, Q = 0\rangle = \frac{1}{\sqrt{2}} \left(|d\bar{d}\rangle - |u\bar{u}\rangle \right) . \tag{1.5}$$

One of the other neutral states is in the octet, while the last forms the singlet. They are respectively

$$\begin{aligned} |f_8\rangle &= \frac{1}{\sqrt{6}} \left(|u\bar{u}\rangle + |d\bar{d}\rangle - 2|s\bar{s}\rangle \right) \\ |f_1\rangle &= \frac{1}{\sqrt{3}} \left(|u\bar{u}\rangle + |d\bar{d}\rangle + |s\bar{s}\rangle \right) . \end{aligned} \tag{1.6}$$

The fact that the mesons of the octet in Fig. 1.3 do not all have the same mass is a clear indication that $SU(3)$ symmetry cannot be exact. The strange mesons

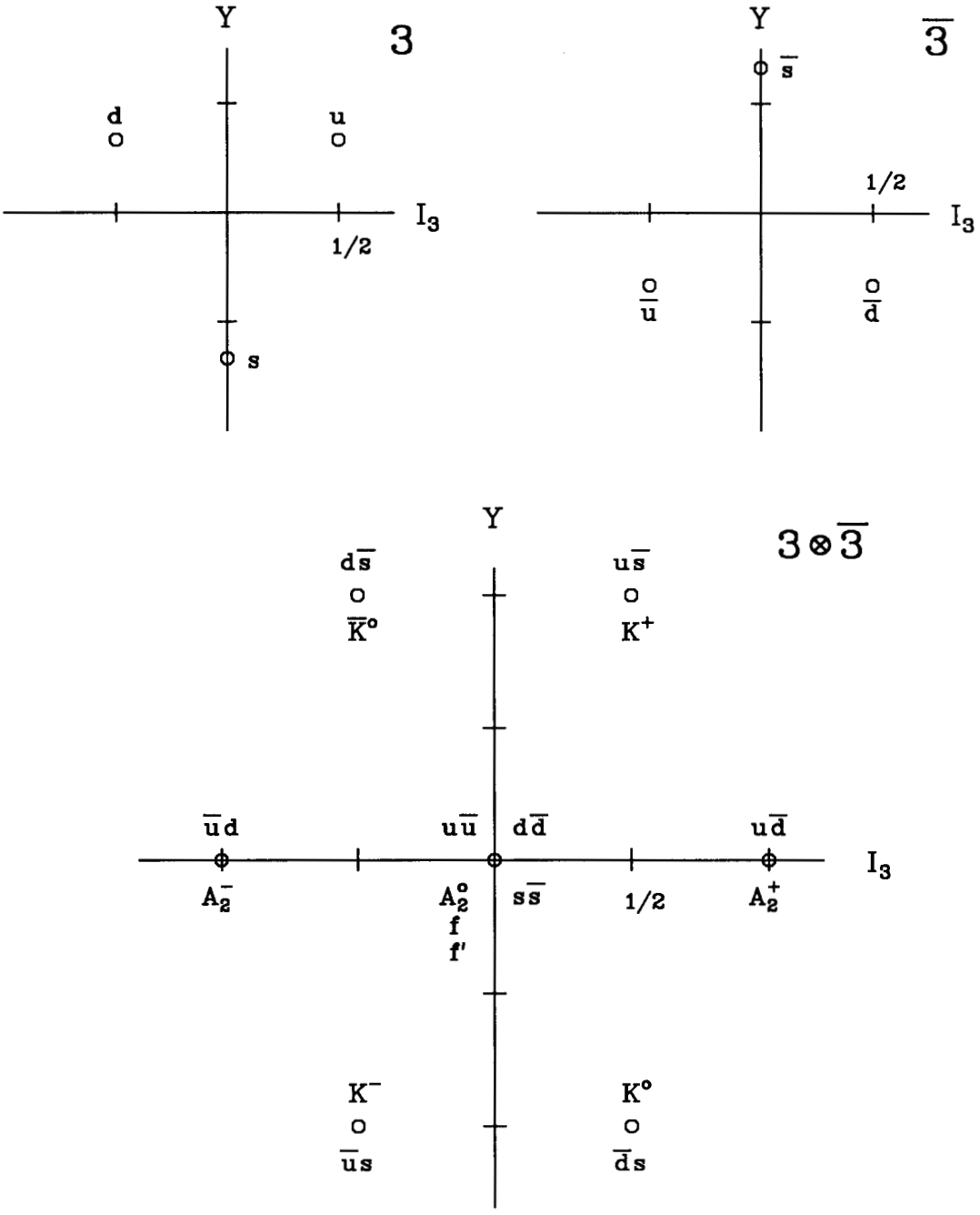

Figure 1.3. $SU(3)$ representations formed by the u, d, s quarks and their antiparticles. I_3 is the third component of isospin, and Y is the hypercharge. The electric charge is given by $Q = I_3 + Y/2$. The K states shown in the octet representation are the $K^*(1430)$.

generally have larger masses than the others, which suggests that the s quark is more massive than the other two. In that case, the symmetric combinations of Eqn. 1.6 are unlikely to be realized in nature. In fact, from the branching ratios to $K\overline{K}$ of the observed mesons f and f', one might guess that the f has almost no s-quark content, while the f' is almost completely composed of s quarks. Let us define these physical states in terms of the f_8 and f_1 through a mixing angle Θ:

$$\begin{aligned} |f\rangle &= \cos\Theta|f_1\rangle + \sin\Theta|f_8\rangle \\ |f'\rangle &= -\sin\Theta|f_1\rangle + \cos\Theta|f_8\rangle. \end{aligned} \tag{1.7}$$

Then the situation called *ideal mixing*, in which the f' is purely $s\bar{s}$, occurs for $\Theta = 35.26°$.

The coupling strength g of $\gamma\gamma$ to a $q\bar{q}$ pair is proportional to the square of the quark charge:[8]

$$\begin{aligned} \langle q\bar{q}\,|\,\gamma\gamma\rangle &\propto e_q^2 \cdot \Psi_q(0) \qquad (S-\text{wave}) \\ \langle q\bar{q}\,|\,\gamma\gamma\rangle &\propto e_q^2 \cdot \Psi'_q(0) \qquad (P-\text{wave}), \end{aligned} \tag{1.8}$$

where $\Psi_q(0)$ and $\Psi'_q(0)$ are the radial quark wave function and its derivative at the origin. Assuming that the $\Psi'_q(0)$ are independent of the $q\bar{q}$ flavor, the $\gamma\gamma$ couplings of the tensor mesons then are proportional to coherent sums, given by equations 1.5 and 1.6, of the squares of the quark charges:

$$\begin{aligned} g(A_2 \to \gamma\gamma) &\propto \tfrac{1}{\sqrt{2}}(e_d^2 - e_u^2) = -1/(3\sqrt{2}) \\ g(f_8 \to \gamma\gamma) &\propto \tfrac{1}{\sqrt{6}}(e_u^2 + e_d^2 - 2e_s^2) = 1/(3\sqrt{6}) \\ g(f_1 \to \gamma\gamma) &\propto \tfrac{1}{\sqrt{3}}(e_u^2 + e_d^2 + e_s^2) = 2/(3\sqrt{3})\,. \end{aligned} \tag{1.9}$$

$SU(3)$ requires that the constant of proportionality in Eqn. 1.9 be the same for the A_2 and f_8. The singlet state is not necessarily related that simply to the octet states, however. If one does assume that the wave functions of the

singlet and octet states are approximately equal, then that implies approximately equal binding energies.[11] That in turn implies, when $SU(3)$ symmetry is broken by the s quark mass, nearly ideal mixing of the f_8 and f_1. That is consistent with the observed tensor meson nonet (but not the pseudoscalar nonet), so it is reasonable to use Eqn. 1.9 along with Eqn. 1.7 to relate the $\gamma\gamma$ widths of all three of the physical mesons. With the widths related to the coupling constants by $\Gamma_{\gamma\gamma} \propto m^3 g^2$, we have†

$$\begin{aligned} \frac{\Gamma(f' \to \gamma\gamma)}{\Gamma(f \to \gamma\gamma)} &= \left(\frac{m_{f'}}{m_f}\right)^3 \left(\frac{\cos\Theta - 2\sqrt{2}\sin\Theta}{\sin\Theta + 2\sqrt{2}\cos\Theta}\right)^2 \\ \frac{\Gamma(f \to \gamma\gamma)}{\Gamma(A_2 \to \gamma\gamma)} &= \frac{1}{3}\left(\frac{m_f}{m_{A_2}}\right)^3 \left(\sin\Theta + 2\sqrt{2}\cos\Theta\right)^2 . \end{aligned} \tag{1.10}$$

These relations give a reasonable fit to the data summarized in Eqn. 1.1, but we postpone any more consideration of them until the results of the DELCO experiment have been presented.

Finally, the importance of the $\gamma\gamma$ width goes well beyond these simple predictions of the quark model. First, one would not expect Eqn. 1.10 to be satisfied to a high degree of accuracy, but any clear deviations from it could provide useful experimental input into the problem of meson structure. Second, the $\gamma\gamma$ width has a better potential of being understood theoretically than most nonperturbative phenomena associated with mesons. In fact, in the case of the π^0, the $\gamma\gamma$ width has been rigorously calculated,[12] due to the fortunate occurrence that it proceeds through a fermion loop, the axial anomaly, which is dominated by large loop momenta. Similar success has not yet been achieved for the tensor mesons—the theoretical predictions for $\Gamma_{f\to\gamma\gamma}$ range from about 1 to 20 keV.[13] Nonetheless, the strength of the $\gamma\gamma$ coupling is an important fundamental parameter of any

† Kolanoski points out in Ref. 8 that there does not appear to be a rigorous proof that this expression for the phase space factor is valid—in some publications the width is taken to be proportional to m, rather than m^3. Fortunately, there is not a large variation of mass in the tensor meson nonet.

resonance, and except for the π^0, the best way to measure it is by $\gamma\gamma$ scattering at e^+e^- storage rings.

2. Two-Photon Interactions at e^+e^- Storage Rings

2.1 KINEMATICS

The object of this research is the study of cross sections for particle production from two-photon collisions. But the photons are produced over a range of momenta by electron beams, so the cross sections of interest always are convolved with a two-photon flux having a continuous energy spectrum. Also, the center of mass of the two-photon state generally is not the laboratory system but is boosted with a range of velocities relative to the laboratory. Thus the kinematics and the cross sections both are complicated, so it is essential to understand fully the scattering of the beam particles and production of the two photons before dealing with the interactions of the photons themselves.

First, some conventions must be established for the notation used to describe the kinematics. Figure 2.1 shows a schematic diagram of the collision with some of the variables to be used, which are listed in greater detail below:†

p_i	four-momenta of the electron beams ($i = 1, 2$).
E	the storage ring beam energy.
p_i'	four-momenta of the scattered electrons.
$E_i' \equiv p_i'^0$	energies of the scattered electrons.
$m_e = p_i^2$	the electron rest mass.
φ	angle between the scattering planes.
	$\cos\varphi = (\vec{p}_1 \times \vec{p}_1') \cdot (\vec{p}_2 \times \vec{p}_2')$
θ_i	polar angles with respect to the beam axis.
ϕ_i	azimuthal angles.
$q_i = p_i - p_i'$	momenta of the virtual photons.
$x_i = q_i^0/E$	energies of photons relative to the beam energy.

† Factors of $\hbar$ and c are omitted from formulas and kinematic expressions, and the electron volt is used as a unit of mass, momentum, energy, and, often, of inverse length. Also, the term *electron* is used to refer to both the electron and its antiparticle, in the same way that the terms *muon* and *pion* commonly are used. Positron, or e^+, is used for the antiparticle when the distinction is important.

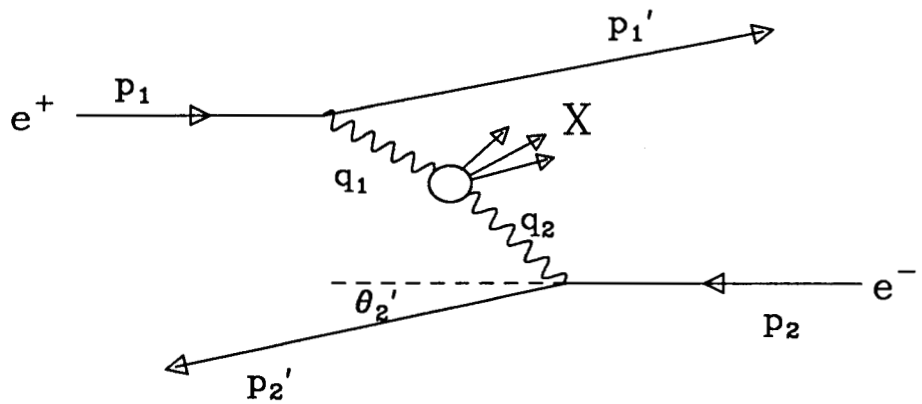

Figure 2.1. A collision of two bremsstrahlung photons. This schematic diagram shows the notation to be used for a description of the kinematics.

$Q_i^2 \equiv -q_i^2$	is always positive.
ε_i	polarization of the photons.
k_j	momenta of the jth particle from the $\gamma\gamma$ system.
$k_\perp = \lvert\vec{k}_{1\perp} + \vec{k}_{2\perp}\rvert$	total transverse momentum of the $\gamma\gamma$ system.
$E_X = \sum_j k_j^0$	total energy of the $\gamma\gamma$ system.
$W = \sqrt{s} = \sqrt{(q_1 + q_2)^2}$	invariant mass of the $\gamma\gamma$ system.
$Z \equiv W/2E$	
$y = \tanh^{-1}\beta$	rapidity of the $\gamma\gamma$ system in the lab frame.
$u_j = \cos\tilde{\theta}_j = \cos\theta_{\rm cms}$	$\tilde{\theta}_j$ is the polar angle of particle j in the $\gamma\gamma$ c.m.s.

The kinematics of the production of the two photons is determined by the four-momenta of the incoming and outgoing electrons. The z axis is defined in the laboratory such that the two incoming beams travel along it with equal and opposite momenta and with energy E (14.5 GeV at *PEP*). The beams at *PEP* are unpolarized, so there can be no overall azimuthal dependence. Also, the polarization of the outgoing electrons is not measured, so the total number of variables to be used to describe the kinematics of the scattered electrons is only

five. These are commonly defined in the laboratory system to be

- two energies, E_1' and E_2', of the scattered electrons,
- two angles, θ_1' and θ_2', that the momenta of the scattered beam electrons make with the beam axis,
- and one angle, φ, between the two scattering planes of the beam electrons.

From these variables, the kinematics of the $\gamma\gamma$ system are readily calculated. The energies of the virtual photons are

$$E_{\gamma_i} = Ex_i = E - E_1' \,, \tag{2.1}$$

and their invariant masses are

$$\begin{aligned} q_i^2 &= (p_i - p_i')^2 \\ &= 2m_e^2 - 2EE_i' \left(1 - \sqrt{1-(m_e/E)^2}\sqrt{1-(m_e/E_i')^2}\,\cos\theta_i'\right) . \end{aligned} \tag{2.2}$$

For all angles θ_i', q_i^2 is less than zero, so the photons have spacelike momenta. Hence it is customary to define the positive quantities $Q_i^2 \equiv -q_i^2$. Since $m_e/E \ll 1$ ($3.5\cdot 10^{-5}$ at *PEP*), most kinematic formulas can be simplified by neglecting terms with it as a factor. One must be careful, though, in the region of very small-angle scattering, where the cross sections are the largest. In that case, $1-\cos\theta_i' \approx \frac{1}{2}\theta_i'^2$ is the order of m_e^2/E^2, so the electron mass cannot be neglected. In fact, substituting $\theta_i' = 0$ into Eqn. 2.2 gives the minimum possible value for Q^2:

$$Q^2_{i\,\mathrm{min}} = m_e^2 \frac{x_i^2}{1-x_i} + \mathcal{O}(m_e^4/E^4) \,. \tag{2.3}$$

On the other hand, if the ith scattered electron is detected at large angle (*tagged*), then it is possible to use the simple formula

$$Q_i^2 = 4E^2(1-x_i)\sin^2(\tfrac{1}{2}\theta_i') \qquad \theta_i' \gg m_e/E \,. \tag{2.4}$$

For both tagged and untagged events, the invariant mass of the $\gamma\gamma$ system can be calculated accurately by neglecting all factors of m_e/E. Using $p_i' = E_i' + \mathcal{O}(m_e^2/E^2)$, we find

$$\begin{aligned} W_{\gamma\gamma}^2 &= (q_1+q_2)^2 = E^2(x_1+x_2)^2 - (\vec{p}_1' + \vec{p}_2')^2 \\ &= 4E^2\left[x_1x_2 - \tfrac{1}{2}(1-x_1)(1-x_2)(1+\hat{p}_1'\cdot\hat{p}_2')\right], \end{aligned} \tag{2.5}$$

where $\hat{p}_1' \cdot \hat{p}_2' = \cos\varphi \sin\theta_1' \sin\theta_2' + \cos\theta_1' \cos\theta_2'$ is the cosine of the angle between the two scattered electrons. Since in most cases the electrons scatter through small angles, yielding photons with small Q^2, a good first approximation for untagged events is to use the simple formula $Z^2 \equiv (W_{\gamma\gamma}/2E)^2 \approx x_1x_2$.

2.2 Cross Sections

The diagram of Fig. 1.1-b divides naturally into three parts, two of which are electron-photon vertices and are understood completely. The well understood factors can be written out explicitly and reduced. Figure 2.2 shows a single electron-photon vertex with the QED Feynman rules included.† It contributes the factor $u(p,s)(-ie\gamma_\mu)\bar{u}(p',s')$ to the scattering amplitude, where $u(p,s)$ is the momentum-space spinor wave function for a free electron with momentum p and spin s. When the amplitude is squared in order to calculate the cross section, and the spins of the unpolarized electrons are summed over, a factor like

$$\rho^{\mu\nu} = \frac{1}{-q^2}\sum_{ss'} \bar{u}(p',s')\gamma^\mu u(p,s)\bar{u}(p,s)\gamma^\nu u(p',s') \tag{2.6}$$

results, where $1/(-q^2)$ is a normalization introduced for later convenience. Using twice the formula

$$\sum_s u_\alpha(p,s)\bar{u}_\beta(p,s) = \left(\frac{\not{p}+m_e}{2m_e}\right)_{\alpha\beta}, \tag{2.7}$$

† The rules may be found in Appendix B of Ref. 14. The conventions used for the metric and other notation associated with field theory are those of Bjorken and Drell.

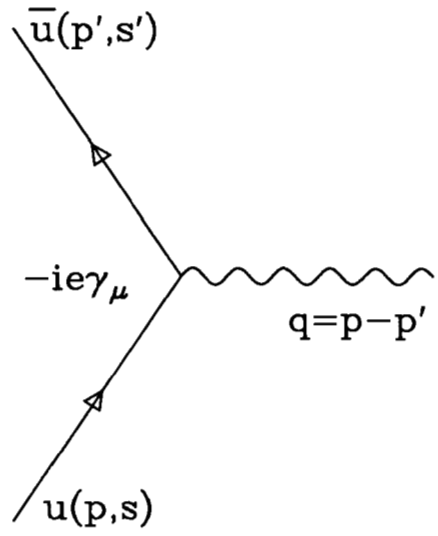

Figure 2.2. An electron-photon vertex with external electron lines.

where $\not{p} \equiv \gamma_\mu p^\mu$, gives the spin density matrix for the virtual photon:

$$\begin{aligned} \rho^{\mu\nu} &= \frac{1}{-2q^2}\mathrm{Tr}[(\not{p}+m_e)\gamma^\mu(\not{p}'+m_e)\gamma^\nu] \\ &= \left(g^{\mu\nu} - \frac{q^\mu q^\nu}{q^2}\right) - \frac{(2p-q)^\mu(2p'-q)^\nu}{q^2}, \end{aligned} \tag{2.8}$$

where $g^{\mu\nu}$ is the metric tensor for flat space-time with trace -2. The density matrix is not diagonal, so the photons are polarized even though the electron beams are not.

Now, consider the full amplitude for the reaction of Fig. 1.1-b. The components are the two electron-photon vertices, the propagators of the virtual photons, and the amplitude for the coupling of two photons to the final state X. The latter is not specified at this point and simply is denoted by $M^{\mu\nu}$, so the expression for the full amplitude becomes

$$S = e^2\bar{u}(p_1',s_1')\gamma^\mu u(p_1,s_1)\left(\frac{-ig^{\mu\alpha}}{q_1^2+i\epsilon}\right)M^{\alpha\beta}\left(\frac{-ig^{\beta\nu}}{q_2^2+i\epsilon}\right)\bar{v}(p_2',s_2')\gamma^\nu v(p_2,s_2), \tag{2.9}$$

where the limit $\epsilon \to 0$ is to be taken. To form the cross section, this amplitude must be squared and summed over all final states relevant to the experiment, averaged

over all initial states, and multiplied by the incident flux. The various initial states are the spins of the unpolarized beam electrons, while the final state consists of a number of free particles, including the scattered beam electrons and the particles resulting from the $\gamma\gamma$ reaction. The latter have continuous spectra of momenta, so the sum over final states becomes an integration, weighted by the density of final states, as well as a discrete sum over the spins. For the normalization we assume for plane-wave particle states, the density of final states for a single particle is E_i^{-1}, and the incident flux is $4[(p_1p_2)^2 - m_1^2m_2^2]^{1/2}/(2\pi)^6$, or to sufficient accuracy for an electron storage ring, simply $\mathcal{F} = 4E^2/(2\pi)^6$. The factor of 4 comes from a sum over all possible electron polarization states. Define $S_{fi} = \delta_{fi} + i\delta^4(P_f - P_i)\,T_{fi}$. Then the cross section for two-photon particle production at an e^+e^- storage ring is given by

$$\begin{aligned}\sigma =& \frac{1}{\mathcal{F}}\frac{1}{VT}\sum_{f\neq i} S_{if}^{\dagger}S_{fi} \\ =& \int \frac{(4\pi\alpha)^2}{q_1^2q_2^2}\rho_1^{\mu\nu}\rho_2^{\alpha\beta}M^{*\nu\beta}M^{\mu\alpha}\frac{(2\pi)^2\delta(q_1+q_2-\sum_i k_i)}{4E^2}\frac{\mathrm{d}^3p_1'\,\mathrm{d}^3p_2'}{E_1'E_2'}\prod_j\frac{\mathrm{d}^3k_j}{E_j}\,,\end{aligned} \tag{2.10}$$

where $4\pi\alpha \equiv e^2$.

As is shown above, the invariant mass and momentum of the $\gamma\gamma$ final state are determined by the momenta of the scattered beam electrons. Therefore, it is useful to differentiate Eqn. 2.10 in order to obtain the distribution of momenta of the scattered electrons. The resulting expression contains the tensor

$$W^{\alpha\beta,\mu\nu} = \tfrac{1}{2}(2\pi)^2\int M^{*\,\alpha\beta}M^{\mu\nu}\delta(q_1+q_2-\textstyle\sum_i k_i)\displaystyle\prod_j\frac{\mathrm{d}^3k_j}{E_j}\,. \tag{2.11}$$

It must be true that $W^{\alpha\beta,\mu\nu}$ can be expanded into a sum of the various products of the available vectors, q_1 and q_2, and the metric tensor, $g^{\mu\nu}$. Budnev *et al.*[15] carry out the expansion in such a way that the result is *explicitly* Lorentz invariant, invariant under time reversal ($\alpha\beta \leftrightarrow \mu\nu$), and gauge invariant ($q_1^{\mu}W^{\alpha\beta,\mu\nu} =$

$q_1^\alpha W^{\alpha\beta,\mu\nu} = q_2^\nu W^{\alpha\beta,\mu\nu} = q_2^\beta W^{\alpha\beta,\mu\nu} = 0$). When multiplied by the density matrices for the two virtual photons and summed over $\alpha\beta\mu\nu$, the differential cross section becomes[16]

$$\begin{aligned} \mathrm{d}\sigma = & \frac{\alpha^2}{16\pi^4 q_1^2 q_2^2} \frac{[(q_1\cdot q_2)^2 - q_1^2 q_2^2]^{\frac{1}{2}}}{E^2} \Big[4\rho_1^{++}\rho_2^{++}\sigma_{TT} \\ & + 2|\rho_1^{+-}\rho_2^{+-}|\tau_{TT}\cos 2\tilde{\varphi} + 2\rho_1^{++}\rho_2^{00}\sigma_{TL} + 2\rho_1^{00}\rho_2^{++}\sigma_{LT} \\ & + \rho_1^{00}\rho_2^{00}\sigma_{LL} - 8|\rho_1^{+0}\rho_2^{+0}|\tau_{TL}\cos\tilde{\varphi}\Big] \frac{\mathrm{d}^3p_1'\,\mathrm{d}^3p_2'}{E_1E_2}\,, \end{aligned} \tag{2.12}$$

where $\tilde{\varphi}$ is the angle between the scattering planes of the two beam electrons in the $\gamma\gamma$ center-of-mass system, and the σ_{ab} are the cross sections for interactions of longitudinal photons ($a, b \equiv L$) and transverse photons ($a, b \equiv T$).† The terms containing τ_{ab} are interference terms arising from polarization of the virtual photons. The quantities ρ_i^{ab}, with superscripts referring to the photon helicities, can be expressed as functions of only the scattered electron momenta, and they are given explicitly in equation 5.13 of Ref. 16. The one which is of special significance for untagged experiments is

$$\rho_1^{++} = \tfrac{1}{2}\left[\frac{(2p_1\cdot q_2 - q_1\cdot q_2)^2}{(q_1\cdot q_2)^2 - q_1^2q_2^2} + 1 + \frac{4m_e^2}{q_1^2}\right]. \tag{2.13}$$

Equation 2.12 shows that the $e^+e^- \to e^+e^-X$ cross section consists of the cross sections for $\gamma\gamma \to X$ convolved with known luminosity functions describing the production of the virtual photons. In the next section, we will see that under certain experimental conditions only σ_{TT} is significant and the luminosity function factors into two parts—one describing each photon.

---

† The term *longitudinal photon* refers to the component of the virtual-photon field with zero helicity (longitudinal polarization of the electromagnetic field), while *transverse photon* refers to the component with helicity ± 1 (transverse polarization).

2.3 The Equivalent Photon Approximation

Because of the factor of $1/q_1^2 q_2^2$ in Eqn. 2.12, it is evident that the cross section is dominated by quasi-real (low Q^2) photons, which are associated with very small scattering angles of the beam electrons. If no requirement is made to tag the scattered electrons at finite angles, then the observed spectra must be dominated by quasi-real photons. In such a case it is advantageous to use an approximate form of the cross section.

Near mass shell, the cross sections for scattering of longitudinal photons vanish;[17] leaving only two terms in Eqn. 2.12. Since the scattered electrons are not tagged in this case, then the azimuthal angles are not known, resulting in an averaging over $\tilde{\varphi}$. Therefore, the interference terms average to zero, and all polarization information is lost. Finally, the approximation $q_i^2 \ll W^2$ simplifies the density-matrix elements, resulting in a factorization of the cross section such that there is a separate factor for each photon:

$$\mathrm{d}\sigma = \sigma_{\gamma\gamma} \mathrm{d}^2 n_1 \mathrm{d}^2 n_2 \,, \tag{2.14}$$

where $\sigma_{\gamma\gamma}$ is the cross section for scattering of two real, unpolarized photons. This is equivalent to an expression for scattering of two beams of real photons with the flux of each given by

$$\mathrm{d}^2 n_i = \frac{\alpha}{\pi} \frac{\mathrm{d}x_i}{x_i} \frac{\mathrm{d}Q_i^2}{Q_i^2} \left[(1 - x_i + \tfrac{1}{2} x_i^2) - (1 - x_i) \frac{Q^2_{i\,\mathrm{min}}}{Q_i^2} \right] . \tag{2.15}$$

What we have arrived at is an equivalent photon approximation (EPA) for two-photon production, in which the electron beams have been replaced by equivalent fluxes of real photons.

Equations 2.14 and 2.15 are intuitively meaningful and are especially useful for doing simple calculations. However, it is important to keep in mind the approximations involved. First, all terms of order Q^2/W^2 in the expressions

describing the kinematics have been neglected. Second, contributions from longitudinal photons have been neglected. For the case of lepton production, $\gamma\gamma \to l^+l^-$, the cross sections are known, and one finds that the ratios σ_{LT}/σ_{TT} and σ_{LL}/σ_{TT} are the order of Q^2/W^2. The third approximation is the neglect of the Q^2 dependence of the $\gamma\gamma$ cross sections. Again, for leptonic final states the variation from the cross section at zero Q^2 is only the order of Q^2/W^2. The relevant cross sections are not known for the case of hadronic final states, but experience with hadronic form factors and $\gamma^* p$ collisions suggests that longitudinal-photon contributions and Q^2 variations become important only when Q^2 becomes the order of the square of the ρ mass.[18]

Therefore, EPA should be good as long as $Q^2 \ll W^2$ and, for hadronic final states, $Q^2 \ll m_\rho^2$. If the events are not tagged, then the vast majority of the observed events will satisfy these criteria. If effective *antitagging* is not available to restrict severely the accepted range of Q^2, then part of the observed cross section may not satisfy the criteria sufficiently well. This part will be small enough in most cases, relative to the peak at minimum Q^2, that distributions which are integrated over the range of Q^2 still will not be strongly affected by the approximation.

In Appendix A some techniques and examples are given on how to numerically integrate $\gamma\gamma$ cross sections with the EPA spectrum over a typical detector acceptance. And in Appendix B there is a discussion of how to do such integrations by Monte Carlo methods over an arbitrarily complicated detector acceptance. There the results from using the EPA spectrum are compared with a Monte Carlo integration of the first-order QED cross section made without any approximations. One finds that for untagged events the results of the two calculations cannot be distinguished within the statistical precision of the DELCO data.

2.4 Luminosity Function for Tagged Events

The equivalent photon approximation of Section 2.3 is expected to be of limited usefulness for tagged events because of the neglect of terms of order

Q^2/W^2. In DELCO, tagged events must have at least one photon with Q^2 greater than about $0.13\,\mathrm{GeV}^2$, so with W as low as $0.6\,\mathrm{GeV}$, factors of Q^2/W^2 are not necessarily small. Therefore, let us consider again the exact differential cross section of Eqn. 2.12. We are not concerned with double-tag events, in which both scattered electrons are observed, because the cross sections are too small to be useful in the present experiment. Therefore, the terms containing $\tau_{TT}\cos 2\tilde{\varphi}$ or $\tau_{TL}\cos\tilde{\varphi}$ both average to zero. As for the rest of the terms, the ρ_i^{ab} are known functions, but that is not so useful unless one also has detailed knowledge of σ_{LT} and σ_{LL} as well as σ_{TT}. Except for purely QED processes, such knowledge is very limited.

One expects that for small angle tags, the σ_{TT} term still dominates. Certainly, if one photon is antitagged, as in the DELCO experiment, then at least terms with σ_{LL} still are heavily suppressed. Thus there are only two relevant luminosity functions, which can be related by $\mathcal{L}_{LT} = \varepsilon\mathcal{L}_{TT}$. The polarization parameter ε may be expressed, for a *single-tag* experiment, as[19]

$$\begin{aligned} \varepsilon &= \frac{\rho_2^{00}}{2\rho_2^{++}} \approx \frac{2(1-y)}{2-2y+y^2}, \\ y &= \frac{q_1 q_2}{p_2 q_1} = 1-(1-x_2)\cos^2(\theta_2/2)\,, \end{aligned} \tag{2.16}$$

where electron number 2 is tagged at an angle θ_2. For DELCO, $\cos^2(\theta_2/2) \sim 1$ for all tagging angles, so $\varepsilon \approx 2(1-x_2)/\left[1-(1-x_2)^2\right]$, which is within experimental errors almost constant and unity over the kinematic region typically of interest. In practice, σ_{LT} cannot usually be distinguished from σ_{TT}, so what one measures is $\sigma_{\mathrm{exp}} = \sigma_{TT} + \varepsilon\sigma_{LT}$, for which the luminosity function simply is $\mathcal{L}_{TT}$. Even then, one must have some way of parameterizing the Q^2 dependence of σ_{exp}, but that problem is deferred to the next section. Here we discuss only how to calculate $\mathcal{L}_{TT}$ without making the assumption used in EPA that Q^2/W^2 is small for both photons.

In Ref. 20 the calculations of Bonneau *et al.*[21] are used to derive a single-tag luminosity function in which the Q^2 dependence of the untagged electron has been integrated out analytically, from the minimum given by Eqn. 2.3 up to the maximum of $4E^2(1-x)\sin^2(\hat{\theta}/2)$, where $\hat{\theta}$ is the minimum tagging angle. As a result, Eqn. 2.12 is approximated by

$$\frac{\mathrm{d}\sigma}{\mathrm{d}x_1\,\mathrm{d}x_2\,\mathrm{d}\theta_2} = \frac{\mathrm{d}\mathcal{L}_{TT}}{\mathrm{d}x_1\,\mathrm{d}x_2\,\mathrm{d}\theta_2}\sigma_{\exp}(k_i, Q_2^2)\,. \tag{2.17}$$

$\mathcal{L}_{TT}$ is the desired tagged luminosity function:

$$\begin{aligned}\frac{\mathrm{d}\mathcal{L}_{TT}}{\mathrm{d}x_1\,\mathrm{d}x_2\,\mathrm{d}\theta_2} &= \frac{\alpha}{8\pi^2}K\cot\tfrac{1}{2}\theta_2\left[\frac{(K-2x_1)^2}{K^2}+1\right]\\ &\times\left[\left(\frac{[K-2(x_2+(Q_2/2E)^2)]^2}{K^2}+1\right)\ln\left(\frac{2E}{m}\frac{(1-x_1)}{x_2}\sin\tfrac{1}{2}\hat{\theta}\right)-2\frac{1-x_1}{x_1^2}\right],\end{aligned} \tag{2.18}$$

where $K \equiv (W^2+Q_2^2)/4E^2$. Electron number 2 is assumed to be the one which is tagged.

It is difficult to estimate the effects of the approximations leading to Eqn. 2.18, but some idea of its validity can be obtained by comparing with the Vermaseren[22] Monte Carlo† calculation of $e^+e^- \to e^+e^-e^+e^-$. The Vermaseren program does an exact calculation of the matrix element for the two QED Feynman diagrams corresponding to Eqn. 2.12 and also includes four more diagrams which contribute to the same final state in leading order QED. Those four additional diagrams, however, play a minor role within the phase space covered by DELCO's acceptance.

This comparison has been made by using in Eqn. 2.17 a formula for $\sigma_{\gamma\gamma\to e^+e^-}$ which really is completely valid only for $Q^2 = 0$. The acceptance is defined such that one of the final-state electrons scatters within 27 mrad of the beam, another is in the tagging range $27 < \theta < 93$ mrad, and the remaining two are within the central acceptance $-0.6 < \cos\theta < 0.6$. Also, the two electrons in the

† Refer to Appendix B for a discussion of how the Monte Carlo calculations are done.

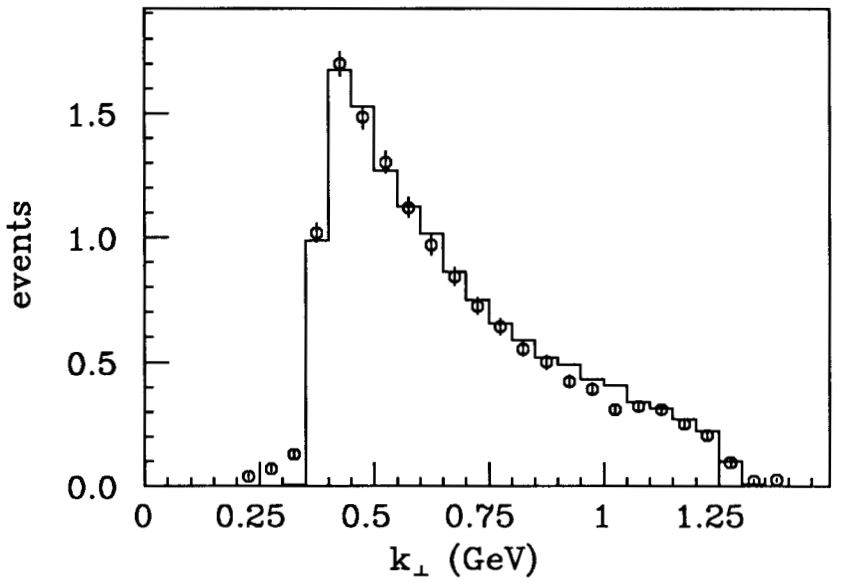

Figure 2.3. The distribution of $k_\perp$ for tagged Monte Carlo events, comparing the simplified calculation (solid line) with that of the Vermaseren Monte Carlo. The two distributions are normalized to contain equal numbers of events total.

central acceptance must have an invariant mass in the range $0.6 < W < 2.6\,\mathrm{GeV}$. Obviously, the approximation used for σ_{TT} is not good since it contains no Q^2 dependence. Nonetheless, the shapes of the invariant-mass and angular distributions for the two electrons in the central acceptance are indistinguishable within the statistical precision available to the experiment. Even the distribution of the total transverse momentum of the two electrons in the central acceptance agrees quite well, as seen in Fig. 2.3. However, the integrated cross section is about 10% higher than that calculated by the Vermaseren program. Such a discrepancy is to be expected, since the Q^2 dependence of σ_{TT} is neglected.

2.5 Extrapolations of Cross Sections to Large Q^2

Some simple models are available to predict the Q^2 behavior of cross sections in $\gamma\gamma \to$ hadrons. We consider just the case in which only one of the two photons has non-negligible q^2, so for example, $Q^2 = -q_2^2$ and $q_1^2 \approx 0$. The vector dominance

model (VDM) predicts that for small Q^2, relative to m_ρ^2, for example, such cross sections are proportional to a ρ-pole form factor:[23]

$$F_\rho(Q^2) = \left(1 + \frac{Q^2}{m_\rho^2}\right)^{-2} . \tag{2.19}$$

This model is extended in Ref. 24 to be valid for somewhat larger Q^2 by including contributions from the ω and ϕ vector mesons plus a term designed to approximate the higher resonances and the continuum. Also, for large Q^2 it is important to include effects from longitudinally polarized photons. That is done by assuming terms for σ_{LT} identical to those for σ_{TT}, only suppressed by a factor of $Q^2/4m_V^2$, where m_V is the relevant vector meson mass. Overall, the prediction for the measured cross section is given by a generalized vector dominance model (GVDM):

$$\begin{aligned}\sigma_{\text{exp}} =& \sigma_{TT} + \varepsilon\sigma_{LT} \\ =& \left[\sum_{V=\rho,\omega,\phi} r_V\left(1+\frac{Q^2}{4m_V^2}\right)\left(1+\frac{Q^2}{m_V^2}\right)^{-2} + r_c\left(1+\frac{Q^2}{m_0^2}\right)^{-1}\right]\cdot\sigma_{\gamma\gamma}(Q^2=0).\end{aligned} \tag{2.20}$$

The five parameters are determined by fitting to lepton-nucleon scattering data, for which this model does give a good fit. The numbers given in Ref. 24 are $r_\rho = 0.65$, $r_\omega = 0.08$, $r_\phi = 0.05$, $r_c = 0.22$, and $m_0 = 1.4\,\text{GeV}$.

The GVDM prediction may be used to extrapolate the measured two-photon partial widths of the f and f' to $Q^2 = 0$. However, a Monte Carlo calculation of the model for $\gamma\gamma \to \pi^+\pi^-$ described in Chapter 7 reveals that the cross section integrated over the acceptance for an untagged experiment decreases by only 1.4% when the form factor of Eqn. 2.19 is introduced, which almost certainly is an overestimate of the effect. Such a correction is less than the typical experimental uncertainty and thus is not critical. It is of interest, however, to compare the prediction of Eqn. 2.20 with the ratio of results from untagged and tagged experiments.

3. Description of the Apparatus

The DELCO experiment is a collaborative effort of groups from California Institute of Technology, Stanford University, and Stanford Linear Accelerator Center (SLAC). The DELCO detector accumulated data in one of the six interaction regions of the 2.5 km circumference *PEP* electron-positron colliding beam storage ring for a period of three years.† The beam energy was 14.5 GeV, and the luminosity ranged from about 10^{30} to $10^{31}\,\mathrm{cm}^{-2}\mathrm{s}^{-1}$, giving a total luminosity integrated over the running time of about $170\,\mathrm{pb}^{-1}$.

Figure 3.1 and Fig. 3.2 show longitudinal and transverse cross sections of the detector. The most important detector components are designed to intercept particles which scatter at large angles ($> 45°$) from the beam line. Travelling outward from the interaction point, such a particle first passes through the wall of the vacuum pipe and into the inner tracking chambers. Just outside of those are Čerenkov counters, followed by additional tracking chambers, a system of time-of-flight counters, and a shower counter system.

The reference coordinates used to describe the experiment assume that the positive z axis is along the beam line in the direction of the positrons (southward). The positive y axis points upward, and the positive x axis points toward the center of the storage ring. The origin is at the detector center, where the beams collide.

3.1 Tracking System

The inner tracking system consists of two concentric cylindrical drift chambers placed between the poles of a dipole magnet. The magnet produces a nonuniform field in the tracking volume. Its coils are operated with a 3000 ampere current, which saturates the steel pole pieces at a level of about 20 kilogauss. The resulting field at the interaction point is 3.3 kilogauss, and the integral $\int \vec{B} \times d\vec{l}$ for a particle produced at the center and travelling outward to infinity is 1.8 kilogauss-meters.

† The running period was divided into three time blocks, which we denote by *1982, 1983*, and *1984*. Actually, each time block includes the Autumn running period of the previous calendar year.

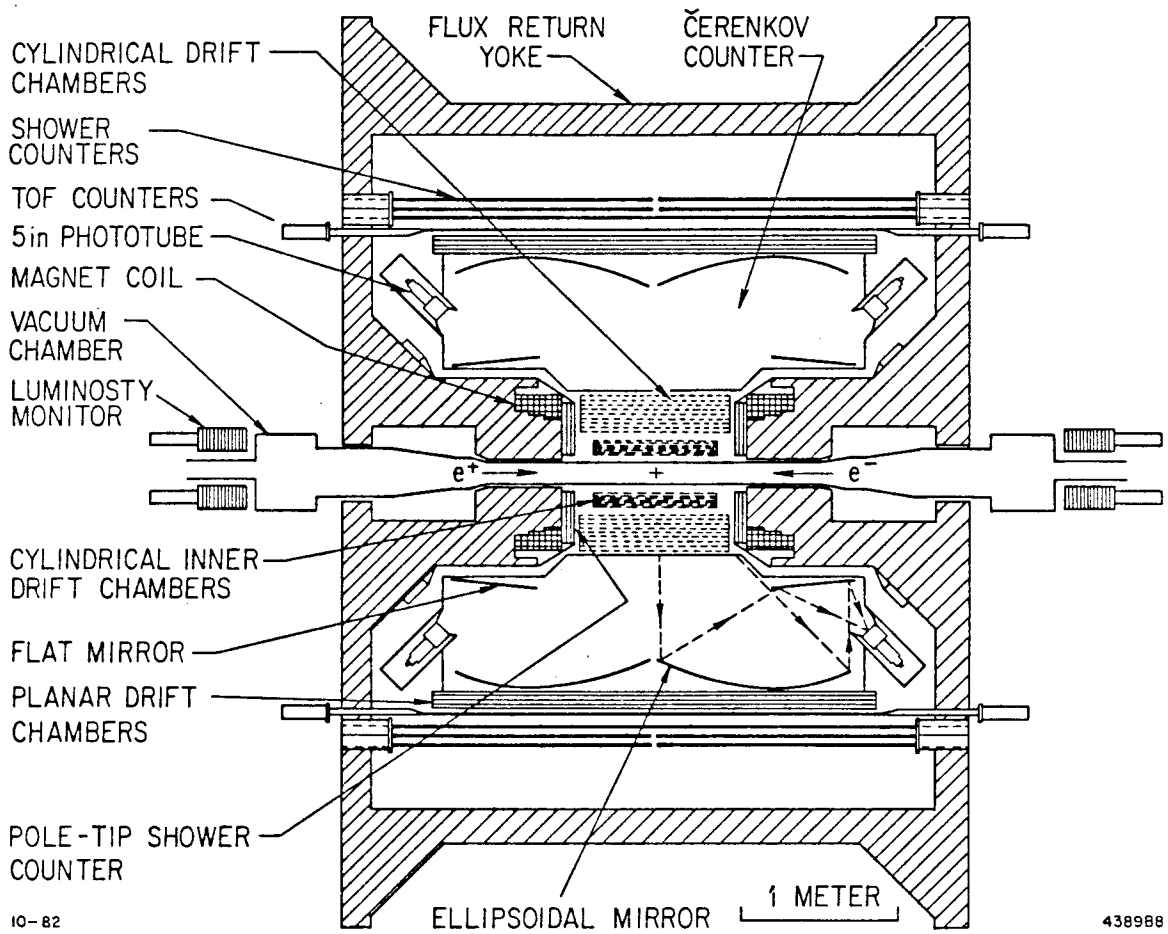

Figure 3.1. Longitudinal cross section of the DELCO detector.

The drift chambers produce a maximum of 16 two-dimensional position measurements for each track. Eight are from layers of cells, called Z layers, arranged parallel to the beam axis, which measure only the coordinates in the transverse x-y plane. Eight more layers consist of stereo cells, arranged with a transverse angle of $\pm 3°$ with respect to the Z cells. They are called U or V layers, depending on the sign of the stereo angle. When used in conjunction with the Z layers, they measure the angle out of the transverse plane (the dip angle λ), as well as giving additional information on the x-y coordinates. The arrangement of the 16 layers is $UUZZVVZZUUZZVVZZ$. The total number of cells is 1214.

Each cell is rectangular in cross section, with boundaries defined by 120 μm

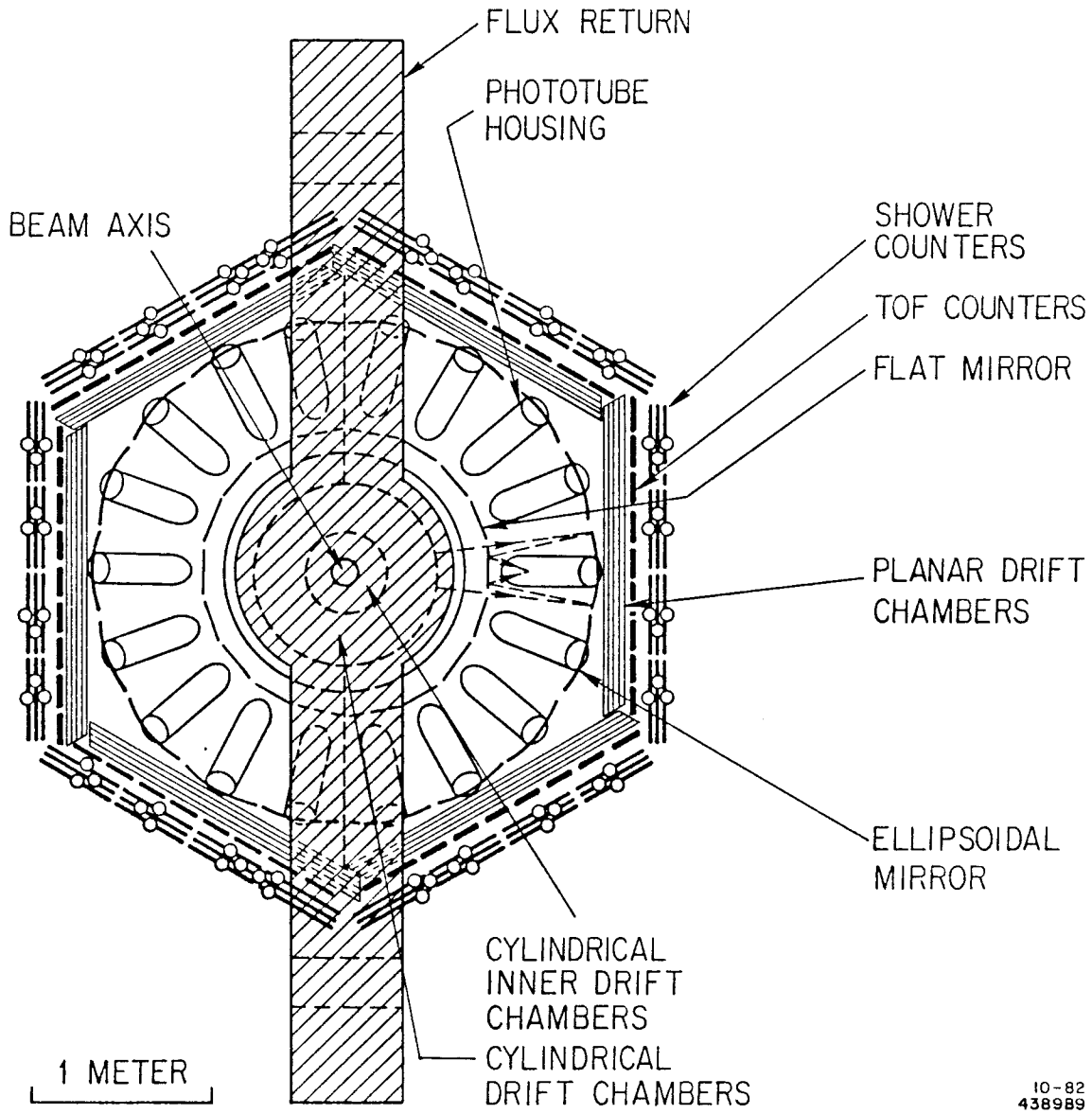

Figure 3.2. Transverse cross section of the DELCO detector.

diameter field wires and guard wires at high voltage. At the center is a thin (30 or 38 μm) gold plated sense wire at ground potential. Figure 3.3*a* shows a cross section of a typical cell. The drift chambers are filled with gas mixtures only slightly above atmospheric pressure. For the first year of running, the mixture was 55% argon and 45% ethane, and thereafter a mixture of 89% argon, 10% carbon dioxide, and 1% methane was used.

A particle travelling radially outward leaves clusters of ionization in the cells along its path. Those which are not too close to the cell boundary drift toward the sense wire along the electric field with a constant velocity of about 5 cm/μsec. The field intensity increases as the wire nears, so close to the thin sense wire an avalanche occurs, giving a gas gain of the order of 10^7. The time of the resulting signal is measured with respect to the beam crossing time to give the drift time. That is converted to a distance by a nonlinear relation determined by an iterative fit to actual data. Whether the track is to the right or the left of the sense wire by that distance must be determined from a global fit of all the individual measurements of a single track. The resulting single-cell resolution varies from layer to layer between 150 μm and 250 μm.

The outer tracking system consists of six planes of six layers each of drift chambers arranged in a hexagon about the Čerenkov counters. Four of the planes have cells parallel to the beam line, and two have large-angle (30°) stereo cells. Each cell is rectangular, as shown in Fig. 3.3*b*, with a solid aluminum perimeter. Typical operating voltages are indicated in the figure. The maximum drift distance of 4 cm is much longer than that of the inner chambers. The single-cell resolution is on average about 500 μm.

Tracking measurements in the x-y plane give the curvature κ of a track, and that combined with the dip angle λ gives the momentum. The full set of parameters used to describe a track are κ and $\tan\lambda$, along with ϕ_0, z_0, and x_t; respectively the ϕ direction, z position, and distance from the beam line at the point of closest approach of the track and beam. A pattern recognition program

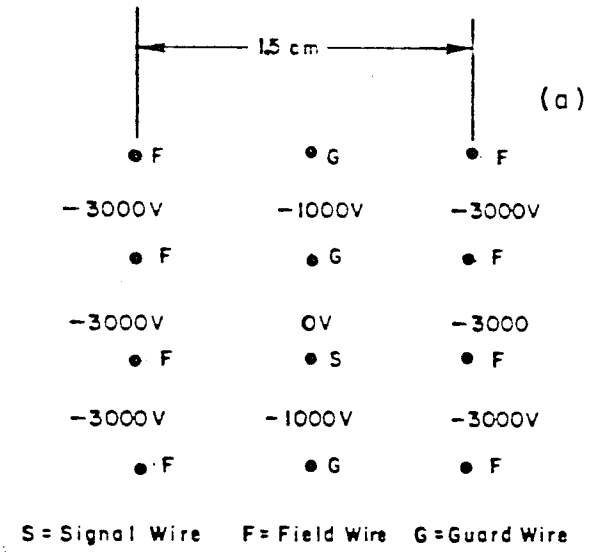

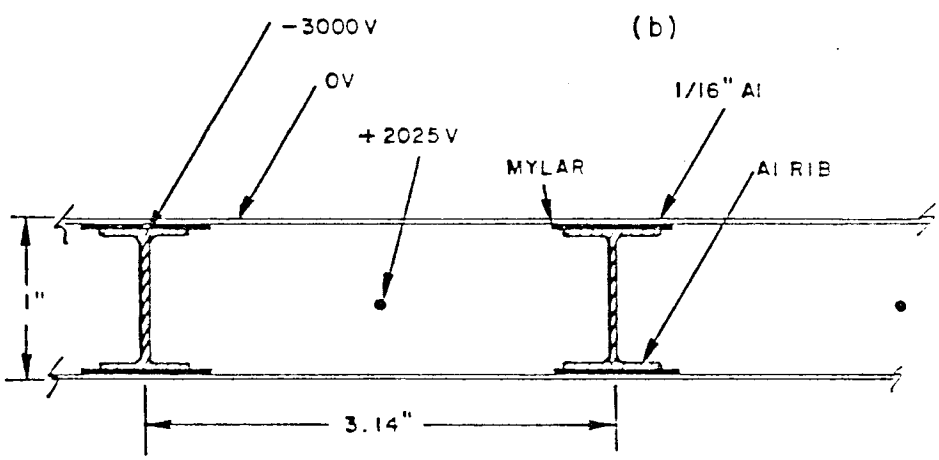

Figure 3.3. Drift chamber cell configurations. (*a*) A typical cell of the inner cylindrical drift chambers. (*b*) A cell of the outer planar drift chambers.

associates the individual measurements, called *hits*, to form a track and does a preliminary fit of these parameters. A track fitting program then does a detailed fit of each track using all the information known about the nonuniform magnetic field. For the events considered in this thesis, this procedure is relatively uncomplicated and error free, because the tracks, being opposite each other, never interfere with one another.

For electrons from Bhabha scattering, the tracking system measures the momenta with a resolution of $\sigma_p/p = 0.02 \cdot p$, where p is in units of GeV. For measuring such high momentum ($p = 14.5$ GeV) tracks, the outer drift chambers are essential, since even at that radius the total track deflection from the magnetic field is only about 2 mm. The errors come from single-cell time measurements and from survey measurements of the positions of the outer drift chambers. The opposite is true for two-photon events, where 0.5 GeV is a typical momentum. For them, the measurement error is dominated by multiple scattering of particles in the detector material. Due to the relatively large amount of material preceding and within the outer drift chambers, those chambers are not useful for momentum measurement in two-photon events. Consequently, their measurements are heavily deweighted in the tracking fit. In fact, no significant change in resolution is observed when they are removed from the fit entirely. They *are* useful for projecting the track into the time-of-flight and shower counter systems, which lie immediately beyond them.

Since the outer drift chambers do not contribute to momentum measurements, the material which causes the multiple scattering limitation to the momentum resolution is that located between the beampipe vacuum and the drift chamber gas, plus the thin wall between the two inner drift chambers. Additional small contributions come from the gas and wires within the tracking volume. The thickness of the beam pipe plus the adjacent inner drift chamber wall was 0.029 radiation lengths of aluminum for the *1982/1983* running period. Before the *1984* run the beampipe was replaced, reducing the thickness to 0.013 radiation lengths.[25]

The wall between the two inner drift chambers was 0.005 radiation lengths thick.

The detector simulation program calculates multiple scattering of individual particles according to a simple gaussian distribution. The angle of deflection in three dimensional space is distributed according to

$$P(\phi,\theta)\,\mathrm{d}\theta\,\mathrm{d}\phi = \frac{1}{2\pi\theta_0^2} e^{-\theta^2/2\theta_0^2}\,\sin\theta\,\mathrm{d}\theta\,\mathrm{d}\phi\,, \tag{3.1}$$

where θ_0 depends on the momentum and the material according to[26]

$$\theta_0 = \frac{14.1\,\mathrm{MeV}}{p\beta} Z_{\mathrm{inc.}}\sqrt{L/L_R}\left[1+\tfrac{1}{9}\log_{10}(L/L_R)\right]\ \text{(radians)}. \tag{3.2}$$

Variables p, β, and $Z_{\mathrm{inc.}}$ are the momentum (in MeV), velocity, and charge number of the incident particle, and L/L_R is the thickness in radiation lengths of the layer of material through which the particle passes. Equation 3.1 is an accurate approximation to the body of the true distribution, but it lacks the small and slowly falling tails which are caused by single hard scattering effects. In the DELCO programs, the material itself is represented by simple concentric cylinders with thin walls. The gas and wires are approximated by the equivalent average amount of material and are treated in the same way as detector boundaries.

Measurement errors for single cells are approximated by smearing the expected drift times according to gaussian distributions of the appropriate width. Bhabha scattering events are used to determine the widths, which works well because the 14.5 GeV tracks suffer very little from multiple scattering.

Such a Monte Carlo simulation of the process $e^+e^- \to e^+e^-\mu^+\mu^-$ predicts the resolutions given in Table 3.1 for the momentum measurement of the muons. These predictions are checked against the data by considering the distribution of the quantity $k_\perp = \left|\vec{p}_\perp^{\,\mu_1} + \vec{p}_\perp^{\,\mu_2}\right|$, which is sharply peaked toward $k_\perp = 0$ and thus highly sensitive to measurement errors. One finds poor agreement; the Monte Carlo prediction is more sharply peaked (smeared less) than the data. If instead

of using the detailed detector simulation, the Monte Carlo generated variables ϕ, $\tan\lambda$, and κ simply are smeared by gaussian distributions of the widths given in Table 3.1, then the same discrepancy is found. In fact, one finds that, for the *1982/1983* data, it is necessary to increase σ_κ/κ to 0.08, with σ_ϕ and $\sigma_{\tan\lambda}$ fixed, in order to achieve good agreement with the data. Various factors besides the momentum resolution, such as radiative effects and the intrinsic $p_\perp$ of the focussed colliding electron beams, have been checked to be sure that they cannot account for the discrepancy, so the problem does seem to lie with the momentum resolution.

Table 3.1. Monte Carlo predictions for the momentum resolution of muons from the process $e^+e^- \to e^+e^-\mu^+\mu^-$

	1982/1983	*1984*
σ_ϕ	0.0058 radian	0.0043 radian
$\sigma_{\tan\lambda}$	0.0077	0.0060
σ_κ/κ	0.056	0.053

A useful process for checking the momentum resolution is $K_s \to \pi^+\pi^-$. A clean sample of 188 such decays, in which the two pion tracks are well separated from any others in the event, were found in the *1982/1983* data by searching for the characteristic decay vertex. The resulting $\pi^+\pi^-$ mass peak, along with a gaussian fit, is shown by Fig. 3.4. The width of the fitted gaussian is $\sigma_m = 19.6 \pm 0.9\,\mathrm{MeV}$. Generating similar decays by Monte Carlo, including the detailed detector simulation, yields a peak with $\sigma_m = 18.2 \pm 0.5\,\mathrm{MeV}$. And when the Monte Carlo resolution σ_κ is increased enough to give good agreement with the $k_\perp$ distribution from two-photon pair production, then the K_s width increases to $21.3 \pm 0.7\,\mathrm{MeV}$. Thus the width from data falls about halfway between the two Monte Carlo assumptions. Unfortunately, there are not enough K_s to make the result highly significant. We conclude that, for low-momentum tracks,

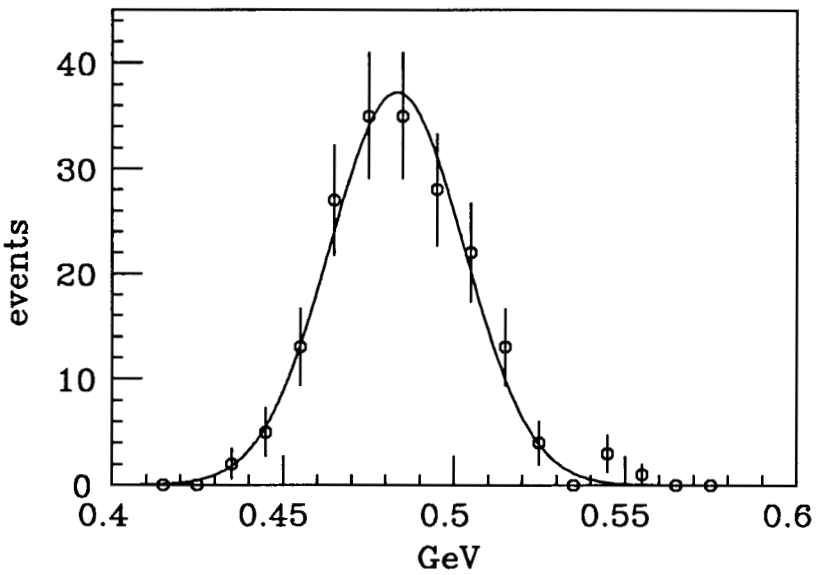

Figure 3.4. The measured K_s mass distribution for *1982/1983* data. The solid curve is a gaussian fit.

$\sigma_\kappa/\kappa = 0.07 \pm 0.01$. This result also is adequate for the *1984* data. Figure 3.5 compares the $k_\perp$ distribution from two-photon produced electron pairs with Monte Carlo predictions for a gaussian resolution of $\sigma_\kappa/\kappa = 0.07$. The angular resolutions are fixed as specified in Table 3.1. It is clear that a gaussian resolution function does not reproduce the shape of the observed $k_\perp$ distribution very well. However, none of the other kinematic distributions of interest are nearly as sensitive to the momentum resolution. The uncertainty of $\pm 1\%$ in the momentum resolution is taken into account when determining the systematic errors in the analyses which follow. With the assumption $\sigma_\kappa/\kappa = 0.07$, the resolution for the invariant mass W of a pion pair in the f resonance region $(0.9 < W < 1.4\,\mathrm{GeV})$ is $\sigma_W = 0.053\,\mathrm{GeV}$.

Finally, one can see from Fig. 3.4 that the K_s peak is as much as 2% low. Measurements of the DELCO magnetic field, however, indicate that the energy scale of the experiment should be accurate to within $\pm 1\%$. In any case, the analysis in this thesis is done in such a way that it is insensitive to any such systematic shifts of the overall energy scale.

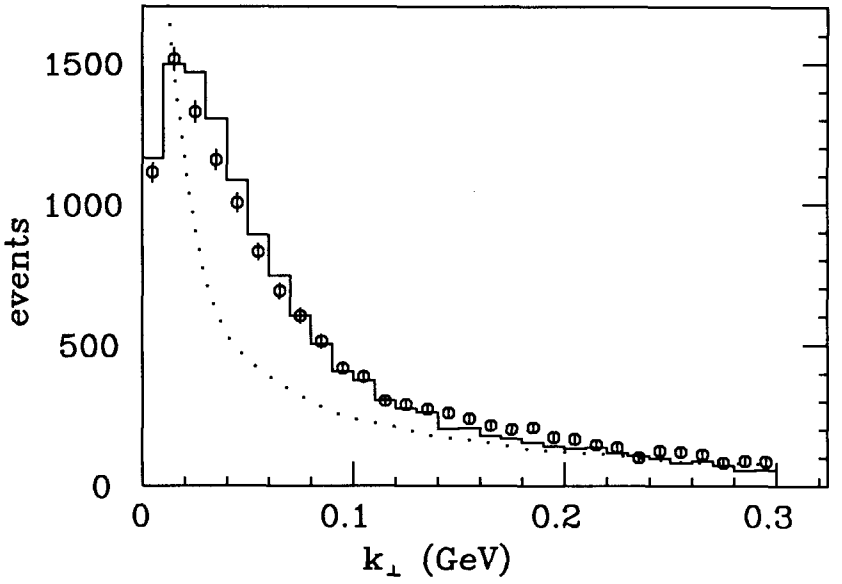

Figure 3.5. The measured distribution of $k_\perp$. The points show *1982/1983* data, which is compared with a Monte Carlo prediction assuming a momentum resolution of $\sigma_\kappa/\kappa = 0.07$. The smooth dotted curve shows the Monte Carlo distribution before adding resolution effects.

3.2 Čerenkov Counter System

The DELCO detector was designed to accommodate a large system of highly efficient gas threshold Čerenkov counters with a minimal amount of material between the beam-beam interaction point and the Čerenkov radiator. This dictates, for example, the configuration of the magnetic field, with the coils placed outside the detector ends. The Čerenkov system consists of 36 cells covering the region $\pi/4 < \theta < 3\pi/4$ and $0 < \phi < 2\pi$, which is about 70% of the full solid angle. There are 18 divisions of the azimuthal angle, and the polar acceptance is divided about the $z = 0$ midplane of the detector.

Two separate data sets were accumulated by the DELCO experiment. In one, the Čerenkov system was filled with atmospheric pressure isobutane. In the other, it was filled with atmospheric pressure nitrogen, which is less dense and therefore gives higher particle thresholds. The radiator path lengths range from 55 to 110 cm. For the isobutane radiator and an incident high momentum electron,

this results in an average of 30 photoelectrons produced at the light detecting photomultiplier tubes. Consequently the efficiency is almost 100% throughout the active volume. Section 4.4 discusses in some detail this question of efficiency as related to the analysis at hand.

The counter optical system is designed for efficient collection of light produced by straight tracks from the origin. That means that if the particle is only slightly above threshold, so that the light is emitted in a cone of large angle about the track, or if the track is at such a low momentum that its curvature in the magnetic field is significant, then the light collection efficiency suffers somewhat. Figure 3.6 is a drawing of the optical system. Large glass elliptical mirrors, one for each cell, are situated such that one focus is at the interaction point and the other is at the face of the phototube. Therefore, all paths from the interaction point to a phototube are of the same length. Winston cones[27] placed before the phototubes aid in the collection of light which is not focussed directly onto the photocathode. Each phototube is protected from the fringe field of the magnetic spectrometer by a small compensating coil and four concentric cylinders of ferromagnetic material.

Both the pulse heights and times of signals from the phototubes are digitized. The system is calibrated by using electrons from the processes $e^+e^- \rightarrow e^+e^-$ and $e^+e^- \rightarrow e^+e^-e^+e^-$. The path length of each track through the counter is known from tracking measurements. The calibration procedure is designed to correct the observed pulse height associated with a given track for the track's path length and the collection efficiency of the particular cell. The resulting corrected pulse heights are normalized to a path length of 100 cm. The time corrections are adjusted such that the mean time is zero. See Ref. 28 for a complete description of the counter design, construction, calibration, and performance.

3.3 Barrel Shower Counters

The barrel shower counters consist of six sextants arranged in a hexagon surrounding the other detector components. Each sextant contains four longitudinal

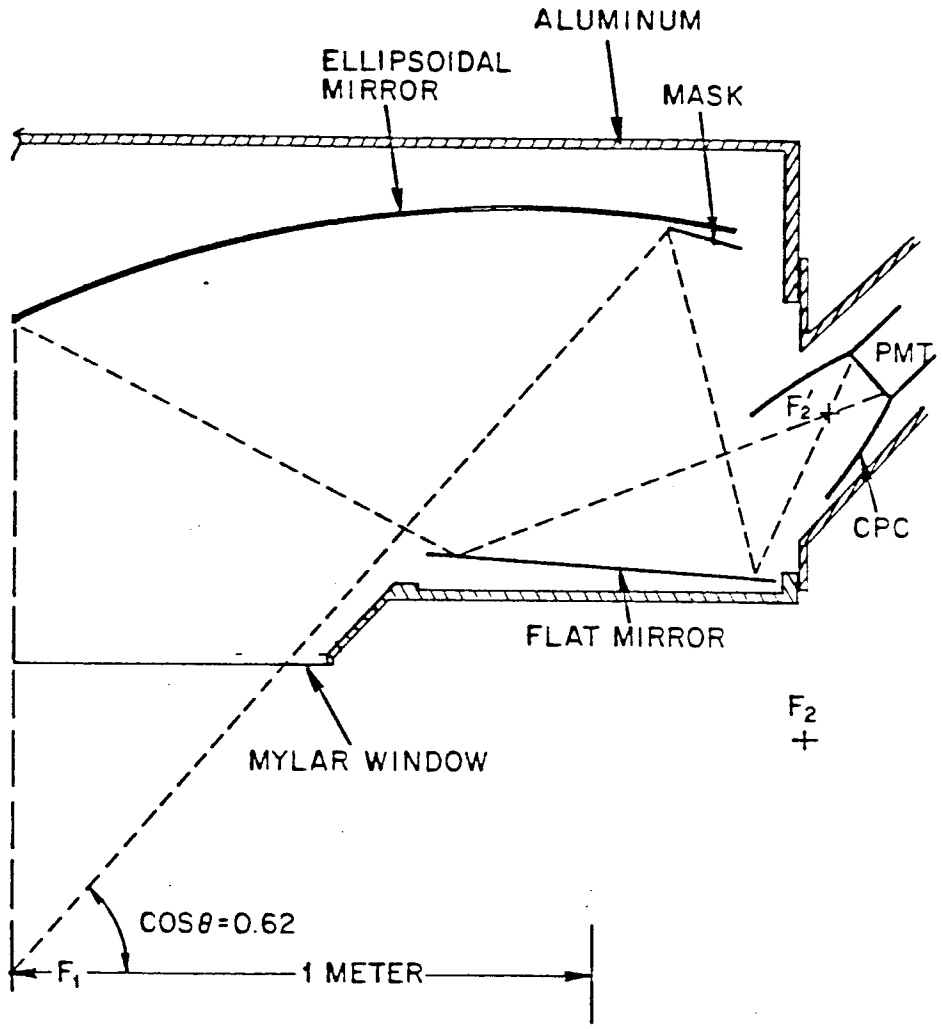

Figure 3.6. The optical system of a Čerenkov counter cell.

counter modules, each with three 1/2 inch thick layers of lead interleaved with three 1/4 inch layers of acrylic scintillator. An aluminum structure supports the four modules with a 1/4 inch thick plane in front facing the interaction point, a 1 inch plane in back, and 1/4 inch thick planes on the sides and between adjacent modules. The first scintillator of each module is read out by phototubes at both ends, while each of the second and third layers are separated by mirrors at $z = 0$ into two counters which are read out at opposite ends of the detector. The total amount of material preceding the last layer of scintillator is 6.9 radiation lengths.

The counter system may be used to distinguish electrons from minimum

ionizing particles, especially at high momenta. However, they are not used for that purpose in the analysis of two-photon events. Such events are low in energy and have widely spaced tracks, which allows identification of electrons by the Čerenkov system. The only purpose of the shower counters in this analysis is to reject background from two-track events with additional particles not detected by the tracking system. Layers 7 through 16 of the inner tracking system have a small dead region at the y-z (vertical) plane which can allow some untracked charged particles into the barrel shower counter region. But for the most part the tracking coverage is more complete than the barrel shower counter coverage, so the main objective of the shower counters is to veto events with photons in the final state.

The barrel shower counters cover the range in polar angle from about $\cos\theta = -0.6$ to $\cos\theta = 0.6$ (the exact cutoff depends on ϕ, since the counters are planar). The azimuthal coverage is broken by 3/4 inch gaps between counters and larger gaps between sextants, so the total solid angle covered is only $0.52 \cdot 4\pi$ steradians. Thus it is possible for many photons to escape detection. However, such background can be estimated, and as we will see, it is not a serious problem.

The only other use of the barrel shower counters which is relevant to this analysis is in the detector trigger. In fact, all of the useful triggers have a shower counter component. That is unfortunate, for such a trigger is inefficient in the detection of low energy, low multiplicity events, and there is little trigger redundancy to exploit in understanding the trigger efficiency. Consequently, the most difficult and most important part of the analysis is to understand the efficiency of the shower counter system.

The individual counters are said to latch when the phototube pulse height is above a low threshold near the beam crossing time. The threshold is a small fraction of the signal expected from a single ionizing particle, so one finds no noticeable inefficiency of the scintillation counters themselves. However, to produce a *shower counter latch*, the trigger logic requires two out of three of the layers in a single module to latch. Therefore, particles must pass through all

of the detector material between the interaction point and the second layer of scintillator before a shower counter latch can occur. That is a total of about 5 radiation lengths or 0.3 interaction lengths.

In later chapters the shower counter latch efficiency is determined for electrons and pions from the data by exploiting what trigger redundancy there is. However, it is important to check the results by calculation. That is done by using the Electron-Gamma-Shower (EGS) Monte Carlo[29] and the High Energy Transport Code (HETC) Monte Carlo[30] to predict the fractions of electrons and pions which will penetrate, in some form, through the material. Special code has been written for this analysis to interface these programs with the detailed geometry of the DELCO barrel shower counters, plus the layers of aluminum, scintillator and glass which precede the shower counters. That in turn is interfaced with the rest of the detector simulation code for the tracking chambers and the Čerenkov counters.

3.4 Poletip Shower Counters

The magnet pole tips are covered by another set of lead-scintillator shower counters consisting of 0.53 cm thick layers of lead interleaved with 1/4 inch thick acrylic scintillator. The total thickness is 5 radiation lengths. Each poletip counter is divided into 18 azimuthal wedge-shaped segments, each of which is read out by BBQ wavelength shifter and a single phototube. There is no radial segmentation. The counters cover the angular range $0.81 < |\cos\theta| < 0.98$, which is 17% of the total solid angle.

In this analysis, these counters are used only as veto counters. No events are accepted which deposit energy above noise level in the poletip counters, whether the energy is from charged particles or photons. Combining the poletip counters with the barrel shower counters gives a total coverage of $0.69 \cdot 4\pi$ steradians for vetoing events with photons and extraneous charged particles.

3.5 Time of Flight Counters

A set of 52 1-inch thick by 8 inches wide acrylic scintillation counters are mounted on the face of the barrel shower counters with 8 or 9 per sextant. Each is read out at both ends by phototubes. They are used in this analysis to reject cosmic ray background (see Section 5.2) and to identify kaons and protons by time-of-flight measurement. The average time resolution for minimum ionizing particles is roughly 330 ps. Refer to Chapter 9 for a detailed discussion of their use and performance in particle identification.

3.6 Luminosity Monitor

The luminosity monitor is made of two sets of six lead-scintillator shower counters, with one at each end of the detector about 280 cm from the interaction point. Each set forms a hexagon about the beam pipe and is segmented into sextants. Each sextant is composed of 16 sheets of 0.56 cm thick lead interleaved with 1/4 inch thick scintillator. All sixteen layers of a sextant are read out by a single phototube by way of a BBQ wavelength shifter bar. In addition there is a scintillator on the front of each sextant which is read out separately. The angular range covered by the counters is roughly 25-90 milliradians with respect to the beam axis.

The counters are designed to monitor beam luminosity by measuring the rate of Bhabha scattering. In this analysis they are used to determine the *relative* integrated luminosity of one run with respect to another, but no attempt is made to obtain from them an absolute normalization. The Bhabha scattering cross section varies like $1/\theta^4$ at these small angles, which necessitates a very accurate knowledge of the counter acceptance in order to predict the integral of the cross section over the acceptance with sufficient accuracy to be used as an absolute normalization. It turns out that it is easier to normalize to measurements of QED processes in the central detector.

An important use of the luminosity counters in this analysis is to tag (or anti-tag) two-photon events by detecting (or vetoing) the scattered beam electrons. They are not used to help veto events with photons in the final state because of the relatively large background of synchrotron radiation from the beams at those small angles. Beam electrons scattered with energies around 14 GeV, however, are well separated from the noise and are relatively easy to detect.† We defer further discussion of the tag analysis to Section 4.9.

3.7 Event Trigger

Signals from the various detector systems are processed by on-line hardware immediately after each beam crossing in order to determine whether anything interesting occurred and the data should be written to tape. This *trigger* process occurs in two stages. The first stage considers only information from the various counters and is fast enough to make the necessary decision between beam crossings (every 2.4 μsec). There are several logical combinations of counters which can produce such a level-1 trigger, and for a high-energy, high-multiplicity event most of them are redundant. For detecting pair production by two photons, however, only three triggers are relevant, and there is not always a redundancy.

Each of the three triggers, which we denote by *KS*, *2S*, and *LS*, includes a barrel shower counter requirement. The KS trigger requires at least one detector sextant to have one or more Čerenkov counters fired in coincidence with one or more shower counter latches. Recall that a shower counter latch is defined to be a coincidence of at least two layers of a single module. The 2S trigger requires at least two different sextants to have one or more shower counter latches, and the LS trigger requires that at least one of the two luminosity counters fire in coincidence with one or more shower counter latches. For all of these triggers, the coincidence time window is centered about the beam crossing time and is sufficiently large to accept all beam related events.

† Such tagging cannot be done with the poletip counters, however, which are too thin to distinguish reliably between such high momentum electrons and photons at much lower energies.

The second stage of trigger processing considers the tracking information from the inner drift chambers and commences only if an event satisfies the level-1 trigger. There also is a level-2 trigger which depends only upon "neutral" energy, but it is not relevant for this analysis. We do not discuss in detail how the hardware defines a "track" but only mention that the definition can accommodate true tracks with momenta as low as 0.1 GeV. The level-2 requirement is for at least one "track" to be found in the inner drift chambers. For the *1984* data, there is also the additional requirement that it must point roughly toward a fired shower counter. If an event satisfies the level-2 requirement, then it is read into the computer and written to tape. The rate of events satisfying the level-2 tracking requirement was typically 1–2 hertz.

The level-2 trigger introduces no loss of efficiency for event types of interest in this analysis—any event leaving two tracks roughly back-to-back in ϕ, through enough cells such that they could be found by the full pattern recognition program, certainly will fulfil this part of the trigger requirement. That is verified by the fact that all such two-track events have *two or more* "tracks" found by the hardware processor.

The level-1 trigger is more of a problem. Aside from the obvious geometric inefficiencies of the various trigger components, the only significant inefficiency which has been found is caused by actual absorption of particles by the material of the detector. That of course depends on the type of particle involved, so we defer all further discussion of trigger efficiency to the sections in which the reaction channels of interest are studied one by one. For a more complete discussion of the hardware of the detector trigger and data acquisition system, one may refer to Ref. 31.

3.8 Data Processing and Reduction

3.8.1 Pass-1 Filter

The first step in off-line processing of data is to analyze all events with a set of programs called the *Pass-1* filter. This filter analyzes all the detector systems, starting with the most simple, and rejects after as little computation as possible those events which cannot possibly be of any use for physics. The cuts made generally cause no inefficiency for physics data beyond what is inherent in the trigger and the detector systems themselves. In this section, only those processing steps which are important to an understanding of the analysis in this thesis are considered.

The first stage of processing considers the information from the shower counters and time-of-flight counters. There must be at least one counter of either system measuring a time-of-flight of less than 11 ns and greater than 3 ns. Such a measurement requires a counter with valid time measurements at *both* ends, but that much is almost certain for events satisfying one or more of the triggers, all of which require shower counter latches. Furthermore, in order to be so identified, kaon pairs and proton pairs must have good timing information from the time-of-flight counters for both tracks. The only potential inefficiency, then, is from the 11 ns cut itself. However, it turns out that kaon pairs and proton pairs with enough energy to satisfy the 2S trigger have times of flight to the counter systems which are short enough not to be affected by this cut.

The next stage of processing considers the hits in the tracking chambers in a simple manner similar to what already has been done by the hardware processor of the trigger. The objective is to eliminate quickly events with not enough drift chamber hits to form at least two separate tracks and to eliminate events caused by large bursts of noise. These cuts introduce no inefficiency.

The following stage involves the detailed pattern recognition necessary to associate drift chamber hits into complete tracks, each with measured curvature and direction. It is important that the preceding stages eliminate as many junk

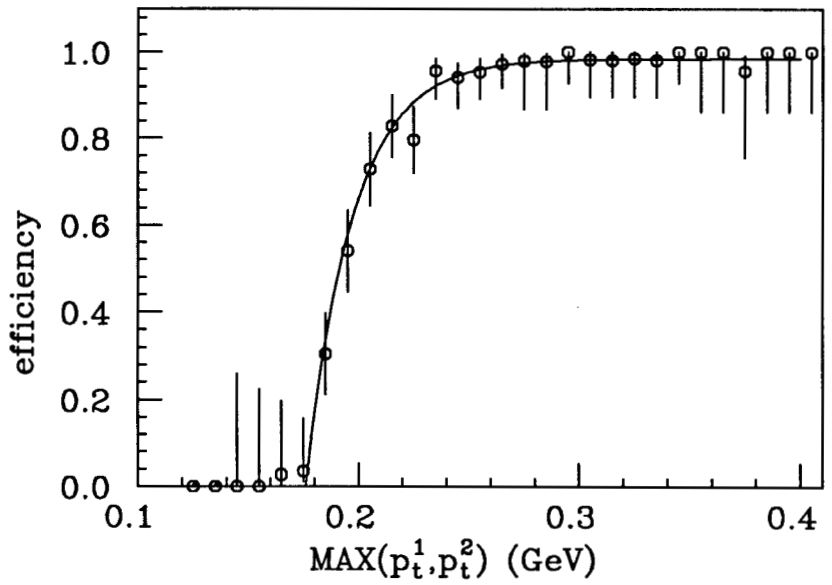

Figure 3.7. The efficiency of the pattern recognition early abort feature used in the Pass-1 filter for two-track events.

events as possible, because the pattern recognition is relatively time consuming. For the same reason, the pattern recognition programs are design to abort early those events which do not look promising. The programs look first for relatively straight tracks coming from close to the origin and having associated hits from both the inner and outer tracking systems. If no such tracks are found in the first pass, then the event is rejected. The result is that events in which no track has a transverse momentum p_t greater than about 0.2 GeV get rejected. Actually, the cutoff is somewhat soft, as shown by Fig. 3.7.

The Pass-1 filter requires that each event have at least two tracks found by pattern recognition. Details of the pattern recognition are not discussed here, because although the procedure is complicated in general, for events with only two tracks it is relatively simple and not problematic. The only problem which occasionally arises is when a large amount of noise overlaps a track or mimics a track.

After pattern recognition is complete, the resulting tracks are extrapolated in order to associate individual Čerenkov, time-of-flight, and shower counters with

each track. At this point, the Pass-1 filter requires that at least one track have an in-time time-of-flight or barrel shower counter associated with it in this manner.

3.8.2 Event Classification

After the Pass-1 filter has been applied, the results are passed through several filters designed to classify and separate the events into several physics and calibration categories. The categories are not exclusive, and the cuts applied generally are very loose. By far the largest physics data set is generated by the two-photon filter, which is the only one of interest here.

All of the cuts of the two-photon filter are superseded by analysis cuts discussed in the following chapters. First, very obvious cosmic rays are rejected, but the cosmic-ray cut discussed in Section 5.2 is more severe. Second, all events with greater than 4 GeV of energy detected in the luminosity counters are accepted as tagged event candidates. The remaining events are subjected to four additional loose cuts, designed to accept charged exclusive events: The total event charge must be no more than 2 in absolute value; the average of the z coordinates of the track origins must be less than 8 cm in absolute value; the sum of the track momenta must be less than 5.5 GeV; and the total transverse momentum $k_\perp$ must be less than 0.6 GeV.

3.8.3 Track Fitting

After classification, events are passed through track fitting programs, which are designed to improved upon the fit obtained in pattern recognition by doing a more complete integration of each track through the non-uniform magnetic field. A track is described by the five parameters κ, $\tan\lambda$, ϕ_0, z_0, and x_t at the point nearest the beam. These parameters describe a helix, but because of the non-uniformity of the field, the overall track is not helical. However, each step of the integration covers a small region in which the field is sufficiently uniform that the track segment is a helix to a good approximation.

After the track has been integrated through the drift chamber regions, for each cell through which it passes the distance of the track from the measured hit position may be calculated. A χ^2 value is formed by the sum of squares of such residuals, with each term divided by the square of the expected error. Correlations between layers are not included, though they can be caused by multiple scattering. For low momentum events, the expected errors for the outer drift chambers are expanded to large enough values that those chambers do not contribute very much to the momentum measurement. That is appropriate for two-photon events, since there is a relatively large amount of material before and within the outer drift chambers. The derivatives of χ^2 with respect to the five parameters are approximated analytically, which allows χ^2 to be minimized in a linear approximation. That gives a new set of five parameters to be used as a starting point of the next iteration. Also, in each iteration the program has some freedom to choose new hits and to change hits from one side of the sense wire to the other, in case such a solution is found which gives a better fit than the one determined by the pattern recognition programs. However, time does not allow all possible combinations of hits to be tried.

When the track fitting results are complete, they are used as a basis for repeating the procedure of associating tracks with counters. That is done because the fit results are more accurate than the pattern recognition results alone. Finally, separate summary tapes are made for the tagged and untagged analyses which include only events with exactly two tracks. The resulting data tapes then are ready for physics analysis.

4. The QED Channels

4.1 Complete Calculations of the Cross Sections

There are two common processes in two-photon physics which involve only electromagnetic interactions. They are

$$\begin{aligned} & e^+e^- \to e^+e^-e^+e^- \\ \text{and} \quad & e^+e^- \to e^+e^-\mu^+\mu^- \,. \end{aligned} \tag{4.1}$$

Figure 4.1 shows examples of the leading order (α^4) diagrams which contribute to these processes. When all possible permutations are made, there are a total of thirty-six amplitudes for the four-electron final state and twelve for the $e^+e^-\mu^+\mu^-$ final state, all of which must be summed together in each case before taking the square to calculate the cross section. It is prohibitively difficult to square the amplitude and reduce the result analytically to a manageable expression, so in practical calculations the amplitudes are summed numerically before squaring. That makes the algebra more straightforward, but care must be taken to avoid numerical instabilities.

The full leading-order calculation for both processes has been done with Monte Carlo integration by Berends, Daverveldt, and Kleiss.[32] The method which they use is described in Appendix B. Their calculations demonstrate that, for the experimental situation where only two of the leptons pass through the central detector, the first two diagrams of Fig. 4.1 (commonly called the *multiperipheral* diagrams) completely dominate the cross section. In Appendix B, another calculation is made which includes the complete multiperipheral amplitudes, except for interference of the beam electrons with those produced by the two photons, plus four t-channel radiative Bhabha scattering diagrams. That calculation is done to a level of statistical significance comparable to that of our data and shows not only that the multiperipheral diagrams alone can fully describe the cross section, but also that for untagged events the equivalent photon approximation can calculate them with sufficient accuracy.

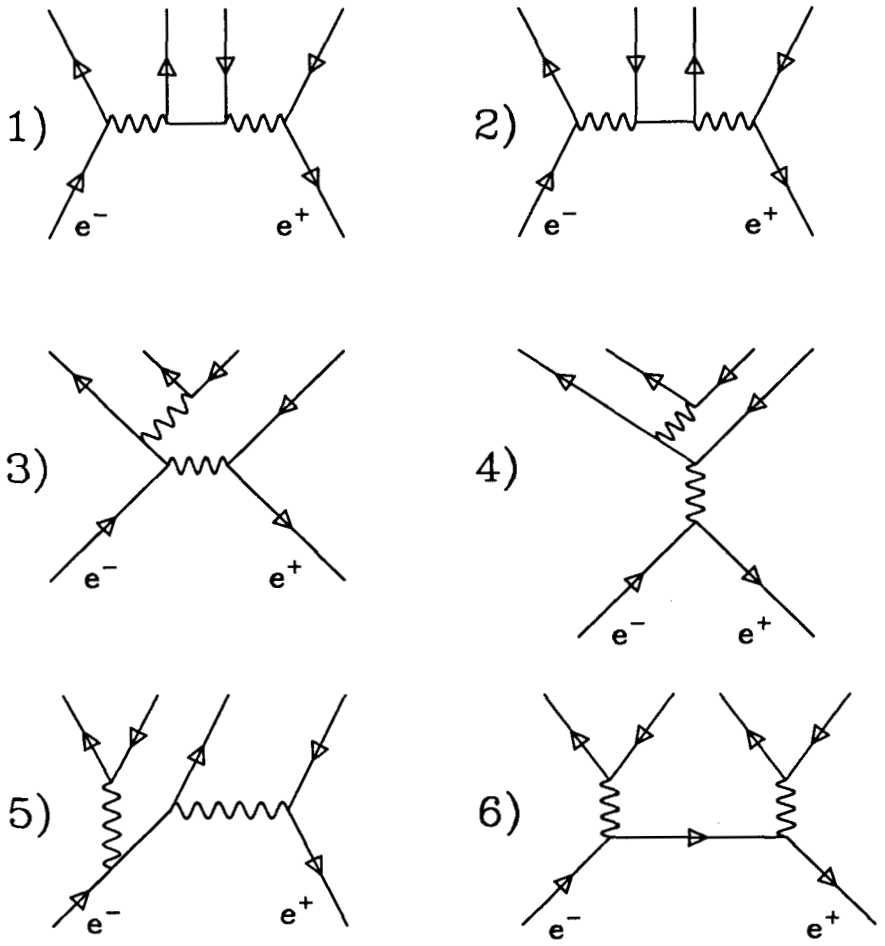

Figure 4.1. The types of diagrams contributing to $e^+e^- \to e^+e^-l^+l^-$. There are a total of 36 diagrams if $l = e$ and 12 if $l = \mu$.

Thus it is clear that an untagged experiment is sensitive to only two of the thirty-six diagrams for the process $e^+e^- \to e^+e^-e^+e^-$. That remains largely true even for an experiment with small-angle ($\approx$ 25 mrad) tagging. These two important diagrams are the type which are important to two-photon physics because they represent the interaction of two photons after each has been radiated by opposing electron beams. Therefore we expect the electron-pairs which are observed in the central detector to have kinematic properties which are similar to those of hadron pairs observed in the same manner. That makes the QED measurement especially powerful for normalization and calibration of the

experiment.

4.2 THE DELCO EXPERIMENTAL ACCEPTANCE FOR $e^+e^- \to e^+e^-e^+e^-$

In the untagged analysis, only two of the electrons are observed in the central detector. For such a configuration, the geometric acceptance is determined by the limits of the barrel shower counters, which are necessary for the trigger, and the Čerenkov counters, which are necessary for identifying the electrons. Actually, any track from the interaction point which hits a barrel shower counter will have passed through a Čerenkov cell, so the shower counters always give a more severe limitation. Their coverage of the polar angle is almost the same as that of the Čerenkov system, but they have many azimuthal gaps. The inner tracking chambers, which also are essential to the measurement, have two azimuthal gaps as well, since layers 7 through 16 separate into two halves along the y-z plane. However, all of the azimuthal gaps have no effect except to cause an inefficiency which is uniform with respect to all of the relevant kinematic variables.

The coverage of the Čerenkov counters is complete within the range $-0.6 \leq \cos\theta \leq 0.6$, which is used in the analysis to define sharply the fiducial volume. The barrel shower counters do not extend quite as far and, in fact, will not intercept all tracks in the interval $0.55 < \cos\theta < 0.60$. Figure 4.2 shows the loss in efficiency incurred by requiring each particle to be tracked into a shower counter. Whether a counter is associated with a track is determined by using the fitted track parameters to provide a starting point for an integration through the magnetic field out to the shower counter module. The exact edge of the counter with respect to $\cos\theta$ will vary from track to track partly because of the spread of several centimeters in z of the beam-beam interaction point, but mostly because the counters are planar—the edge is not at a constant radius from the beam.

Only one electron is necessary for the KS trigger, which requires a Čerenkov cell to fire in coincidence with a shower counter in the same sextant of the detector. Also, it is only necessary to identify one electron before assuming the other particle

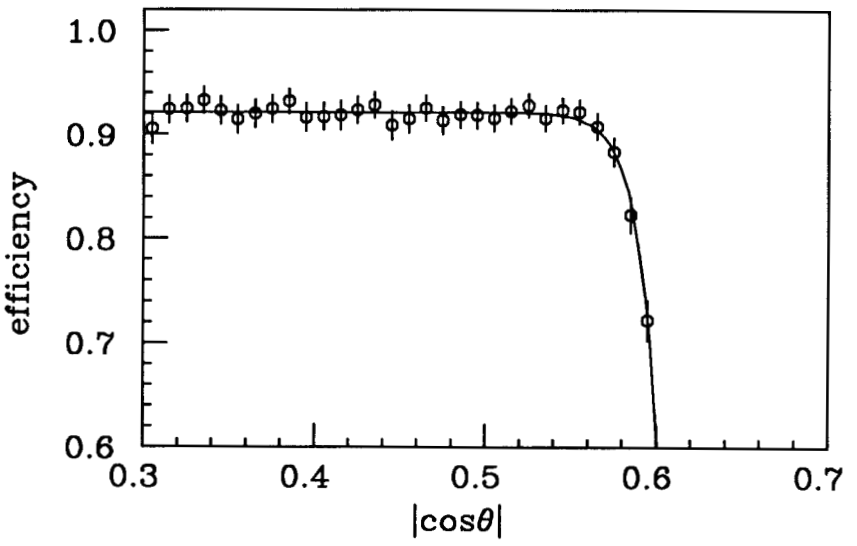

Figure 4.2. The angular acceptance of the barrel shower counters integrated over ϕ. The points shows the efficiency for a track produced near the interaction point at a polar angle θ to strike a shower counter.

also to be an electron, so it would be possible to do the experiment within a fiducial volume which requires only one track to fall within the shower counter and Čerenkov acceptance. However, the trigger is easier to understand if both electrons strike a shower counter module, and the rejection of non-electrons is better if both particles pass through a Čerenkov cell. Since the number of events is so large that the measurement is dominated by systematic rather than statistical uncertainties, we choose to be conservative and require that both tracks fall within the range $-0.6 \leq \cos\theta \leq 0.6$ and that both hit a shower counter.

4.3 Separation of Electrons from More Massive Particles

Electron pairs are selected from the two-track data set by using only the Čerenkov counter information. Separation of electrons from more massive particles is much better for data where isobutane was used as a radiator than for data taken with a nitrogen radiator. That is because the denser gas radiates more light and thus gives a better efficiency for the low-momentum electrons. It does not matter that nitrogen has a higher Čerenkov threshold for muons, because

the isobutane muon threshold is above the momentum range relevant to this analysis. Since the isobutane data itself has a high enough statistical weight that the errors are dominated by systematic effects, there is nothing to be gained from including the nitrogen data, which would only introduce larger systematic errors from background and efficiency corrections. Therefore, the analyses of electron pairs and pion pairs are done with only the isobutane radiator.

With the isobutane radiator, the threshold for muons is about $p = 1.8\,\mathrm{GeV}$. The cross section for any of the particles produced from two photons to have a momentum greater than that threshold within a Čerenkov cell is not large enough to be significant to any of our measurements. Therefore, only electrons will fire the Čerenkov counters, which are used only for separating electrons from all of the heavier particles.

As we will see, the separation of electrons from muons, pions, kaons, and protons is especially good for the events of interest, which consist of a small number of tracks spaced well apart in ϕ. However, the small statistical uncertainty in the experiment requires that the efficiency and rejection be understood at the level of about one percent. To do so, the cuts must be chosen to give optimal efficiency and rejection, and an accurate method of determining the efficiency from the data itself must be found.

The first step of the analysis is to plot the Čerenkov pulse heights and time residuals for both electrons and muons.† Since two-electron events have no ambiguities resulting from multiple particles traversing the same or nearby cells, then it makes sense to include the pulse heights of all cells which the track passes through or nearby. That is especially helpful near the $z = 0$ midplane of the detector. There the efficiency is relatively poor for a combination of reasons. The path length through the radiator is shortest there, the light falls on the mirror edges and is divided between at least two cells, and there is a small dead

† To simplify the discussion, the heavier particles as a group are referred to as muons whenever the distinction between muons, pions, kaons, and protons is not relevant.

region between the mirrors. It also is helpful between cells adjacent in ϕ, where the light tends to be shared between two cells, especially if the track is highly curved. Another important point is that near the edges one cannot be sure from the tracking which cell the particle actually went through. That problem is most severe at the $z = 0$ midplane because the dip-angle measurement is not as good as that of the azimuthal angle. A negative result of adding all associated cells together is that the level of random noise is increased, but the gain in efficiency outweighs the loss in rejection caused by noise.

The events which are used to analyze the identification cuts consist of either two electrons or two muons. The QED process $e^+e^- \rightarrow e^+e^-\mu^+\mu^-$ can produce a muon and an electron within the central detector, but the cross section is relatively minute† and is further suppressed by the requirement of balanced transverse momentum ($k_\perp/W < 0.2$). Another possible background is from $e^+e^- \rightarrow e^+e^-\tau^+\tau^-$, but it is heavily suppressed by the kinematic cuts.‡ Therefore, we assume that in all cases the two particles are of the same type. That allows a strategy to be used which makes the histograms easier to understand. One of the two particles, chosen at random, is classified as an electron or muon (or neither if the result is ambiguous) by the use of cuts which are designed to give high rejection of background at the expense of good efficiency. Subsequent results verify that cuts can easily be found which result in essentially 100% rejection of background. If the particle is in one of the two categories, then the other is assumed to be of the same type, and it is entered into one of two plots, depending on whether it is an electron or a muon.

The Čerenkov time residual is used to reject background noise. Fast charged particles coming directly to the phototube from the interaction point produce times centered about zero, whereas the noise is distributed uniformly in time. Figure 4.3 shows a histogram of the best time of all cells associated with an electron. The

† See Ref. 32 for some example calculations. For an acceptance cut of $25° < \theta < 155°$, for example, they calculate $\sigma_{\mu e}/\sigma_{\mu\mu} = 5 \cdot 10^{-4}$.

‡ The background from tau-pairs is estimated in detail in Section 4.6.

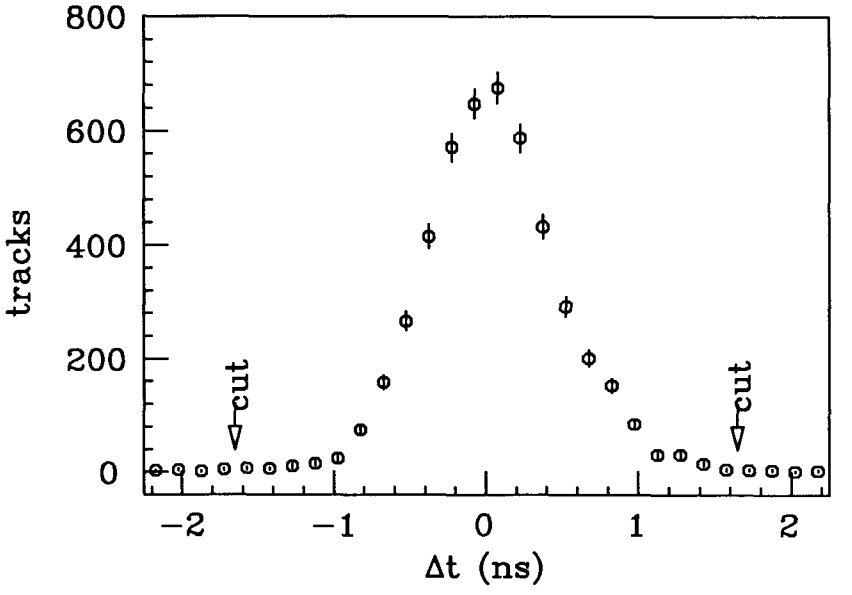

Figure 4.3. The distribution of Čerenkov time residuals from electrons.

cuts for the remainder of the analysis are placed at ± 1.65 ns and reject less than 1.4% of actual electrons.

When the Čerenkov counter is used to select particles with velocities above threshold, it is important for uniformity of the cut to consider the path length of the track through the radiator and the efficiency of the cell in question. On the other hand, if it is used to reject tracks with associated light, then the raw pulse height should be used because the noise level does not depend on the path length. Therefore, when selecting electrons one considers the path-length-corrected pulse height. Figure 4.4 shows the lower end of the distribution for particles which have been assumed to be electrons. About 1% of the particles give essentially zero pulse height. A small number of these may actually be muons, but we will see that the number of zeroes is consistent with the inefficiency near the detector $z = 0$ midplane. That fraction would be rejected by any useful cut, so the best possible efficiency is obtained with a cut requiring the pulse height to be greater than about 1.5 photoelectrons.

When a single track in each event is identified, there is a contamination

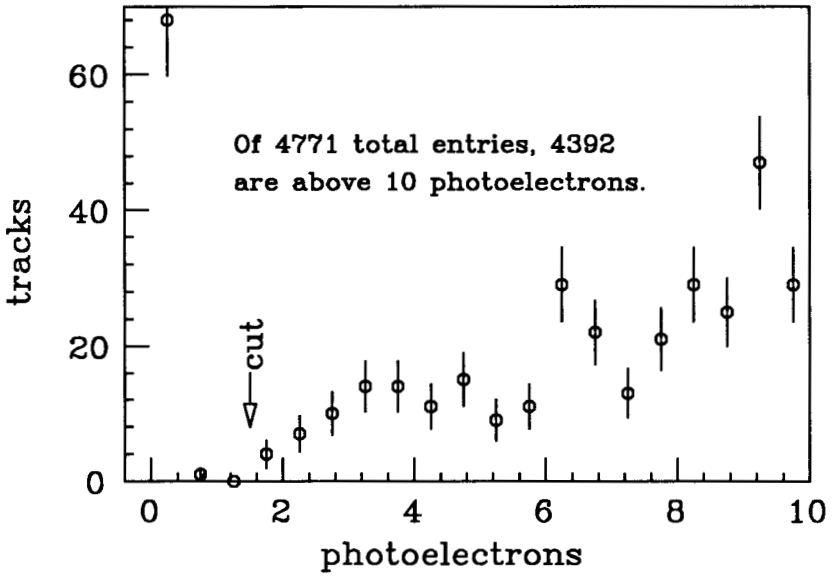

Figure 4.4. The distribution of Čerenkov pulse height for electrons. The pulse heights have been corrected to cancel differences resulting from differing track lengths and different cells.

of muons at the level of one half to one percent due to random noise which forms a narrow peak around a pulse height of one photoelectron. However, when muons with out-of-time raw Čerenkov signals at the level of one photoelectron are used to make a histogram of the path-length-corrected pulse height, the result is that the one-photoelectron noise peak is pushed up to the level of two to three photoelectrons corrected. A cut placed high enough to give complete rejection of muons will seriously compromise the electron efficiency. Furthermore, the analysis requires that both tracks in each event pass the identification cuts. That increases the rejection at the expense of lowering the efficiency. Therefore, the final decision is to require all electrons to have a corrected Čerenkov pulse height, summed over all associated counters with time residuals between -1.65 ns and 1.65 ns, which is greater than 1.5 photoelectrons. Then the contamination of muon pairs is less than 0.01^2, which is completely negligible.

4.4 Electron Identification Efficiency

The efficiency of the cuts chosen for selecting electrons can be measured in a unbiased way directly from data. The method relies on the fact that a cut on the Čerenkov pulse height placed well above three photoelectrons corrected, which is beyond the limit of the background noise, will reject 100% of muons. The analysis proceeds by choosing a random track from each event and rejecting the event if that track has an in-time ($|\Delta t| < 1.5\,\mathrm{ns}$) pulse height of less than six photoelectrons corrected. The remaining events have an insignificant contamination of muon pairs, so the opposite track in each event can be used to study the efficiency of the analysis cuts. The six-photoelectron cut rejects only 3% of electrons overall and introduces no significant bias for the opposite track.

In the following efficiency plots, the points represent for each bin the ratio of the number of electrons which are identified correctly, by the cuts detailed in the previous section, to the total number of electrons. The error bar for a single bin is the statistical uncertainty of the data in that bin only and represents 95% confidence level limits on the ratio. Figure 4.5 shows the $\cos\theta$ dependence of the electron identification efficiency integrated over all momenta within the acceptance. For the isobutane radiator it is about 99.5% in all regions except near the $z = 0$ midplane. The same plot also is shown for the data sample with the nitrogen radiator, so one can see the serious loss of efficiency caused by the less dense gas. There also is some momentum dependence, with most of the inefficiency resulting from low momentum particles. That is a result of the large curvature of the tracks lowering the light gathering efficiency of the optical system, which was designed to focus light coming straight from the interaction point.

Rather than use a smooth two-dimensional parameterization of the efficiency, the angular range is divided into $\cos\theta$ bins and the momentum dependence is parameterized for the central bins by an exponential:

$$\varepsilon(p) = A \cdot \left[1 - 0.6 \exp\left(-\frac{p - p_0}{\tau}\right)\right] . \tag{4.2}$$

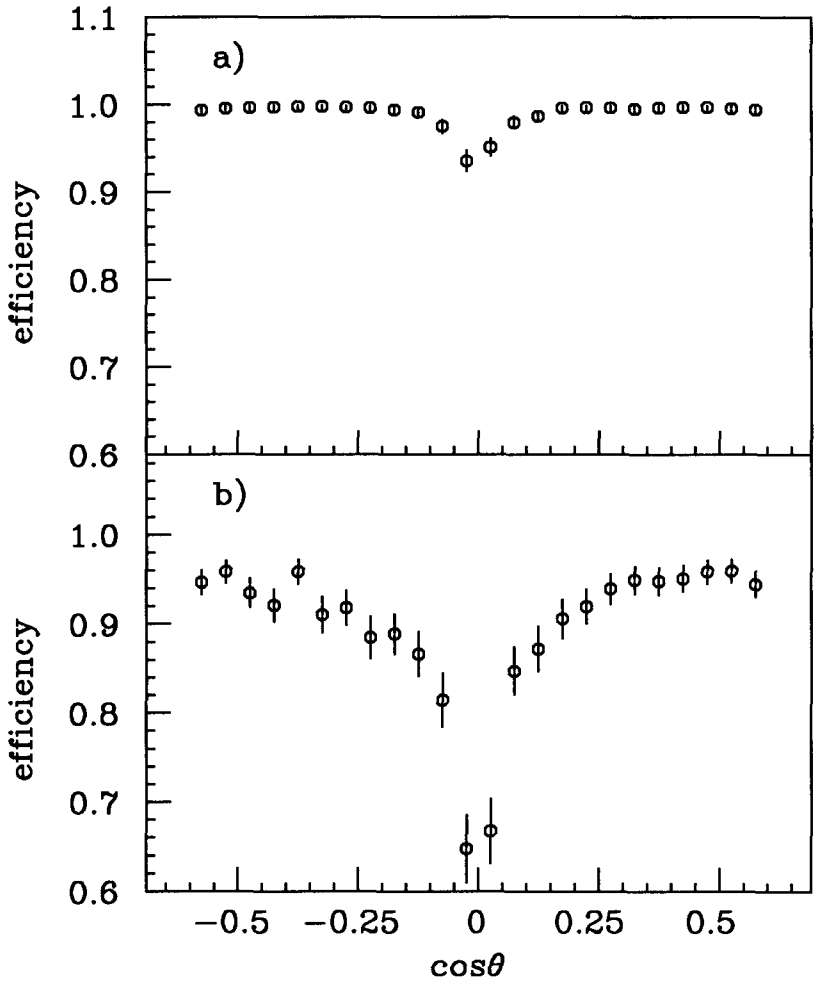

Figure 4.5. The efficiency for electron identification as a function of $\cos\theta$ and integrated over all momenta. (a) with the isobutane radiator. (b) with the nitrogen radiator.

The fitted parameter values are listed in Table 4.1. Note that these parameterizations represent the efficiency for a single track, so the efficiency for both tracks to be identified, as required in the analysis, is lower.

4.5 Trigger Efficiency for Electron Pairs

To determine the efficiency of the KS trigger, one somehow must measure the latch efficiencies of the Čerenkov and shower counters. Judging from the measured electron identification efficiency of the previous section, we expect the Čerenkov

Table 4.1. A parameterization of the electron identification efficiency. The symbols A, p_0, and τ refer to variables in Eqn. 4.2.

$\lvert\cos\theta\rvert_{\mathrm{min}}$	$\lvert\cos\theta\rvert_{\mathrm{max}}$	A	p_0	τ
0.0	0.05	0.975	-0.092	0.15
0.05	0.10	0.990	-0.280	0.15
0.10	0.60	0.995	—	—

latch efficiency to be close to unity except at the $z = 0$ midplane, since the latch threshold is lower than the cuts used for electron identification. However, the shower counter latch, which requires two of three layers to latch, will not fire unless the electron penetrates through at least five radiation lengths of lead. The probability for that is significantly less than unity in the lower end of the momentum range of interest.

The Čerenkov latch efficiency is easily measured from data without any bias from the trigger itself. Only events with a 2S trigger are used. From these, electron pairs are chosen by identifying one particle, chosen at random from the pair, with tight cuts on the Čerenkov pulse height, just as was done for the measurement of the identification efficiency. In this case, though, the identified electron is required to be well away from the $z = 0$ midplane in order to avoid any bias from the identification cut. There is no possibility of bias in the region away from the midplane, because for $|\cos\theta| > 0.10$ the efficiency is essentially 100%.

The particle which is not identified is used to accumulate histograms of the latch efficiency. Figure 4.6 shows the $\cos\theta$ dependence with the full momentum range included. It verifies that the efficiency is essentially 100% when away from the region near $\cos\theta = 0$. Fitting the momentum dependence of the central $\cos\theta$ bins to the parameterization given by Eqn. 4.2 yields the set of parameters presented in Table 4.2.

While we have seen that the Čerenkov latch has only a small and almost

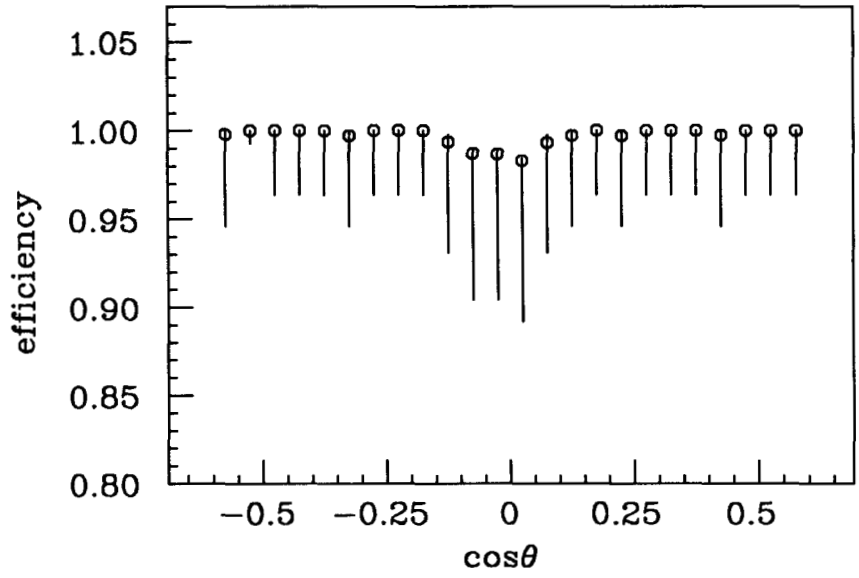

Figure 4.6. The Čerenkov latch efficiency as a function of $\cos\theta$. The full momentum range is included.

Table 4.2. A parameterization of the Čerenkov latch efficiency. The symbols A, p_0, and τ refer to variables in Eqn. 4.2

$\lvert\cos\theta\rvert_{\min}$	$\lvert\cos\theta\rvert_{\max}$	A	p_0	τ
0.0	0.025	1	0.134	0.072
0.025	0.050	1	0.030	0.072
0.050	0.600	1	—	—

negligible inefficiency, that is not the case for the shower counter latch. It is especially important to understand the shower counter efficiency because every trigger requires at least one shower counter to latch. It can be measured from the data because the trigger is redundant; only one of the two electron tracks must fire a shower counter. Therefore, the efficiency can be seen directly by selecting electron pairs in which both particles hit a shower counter and simply accumulating efficiency histograms using the latch information of both hit counters. The result is, however, biased by the trigger, because it is not possible to include in the

histograms any events in which both electrons have failed to latch a shower counter. That bias must be corrected by Monte Carlo calculations.

For the moment we concern ourselves only with inefficiency caused by lack of penetration of electromagnetic showers. Geometric inefficiency is more simple to understand and does not have any momentum dependence. Therefore, histograms are accumulated using only events in which both tracks are projected to hit well within ($\geq 3\,\mathrm{cm}$) the boundaries of a shower counter module.

Figure 4.7 and Fig. 4.8 show the trigger-biased latch efficiencies as functions of the measured electron momenta for the three individual shower counter layers, where only data taken in *1984* are used.† Figure 4.9*a* shows the result for the shower counter latch, which requires two of the three layers to fire. Note that the trigger bias is such that the true latch efficiency is lower than that which is observed. The measured efficiencies are compared with calculations of the same quantities using the EPA Monte Carlo for $e^+e^- \rightarrow e^+e^-e^+e^-$ and a full simulation of detector effects. The shower counter response has been simulated by the EGS Monte Carlo.[29] By using EGS one can do a reasonable job of simulating the propagation and development of the electromagnetic shower through the aluminum, lead, and scintillator. However, when dealing with a sandwich of thin layers of scintillator between sheets of lead it still is difficult to predict with high accuracy how much of the deposited energy actually is collected by the scintillator. Furthermore, there are a number of additional effects which are not handled in much detail. For example, fluctuations in light transmission and phototube response are not simulated at all, and the response of the electronics is treated in a simplistic manner. Therefore, one cannot expect perfect agreement of Monte Carlo with data, and it is the measured efficiency which is used in the ensuing analysis. Nonetheless, the extent of the agreement shown in figures 4.7

† During the summer of *1983*, the gain of the phototubes was lowered to reduce saturation from large pulse heights. The change was compensated by installing amplifiers in front of the latch electronics, but the latch efficiency changed slightly nonetheless.

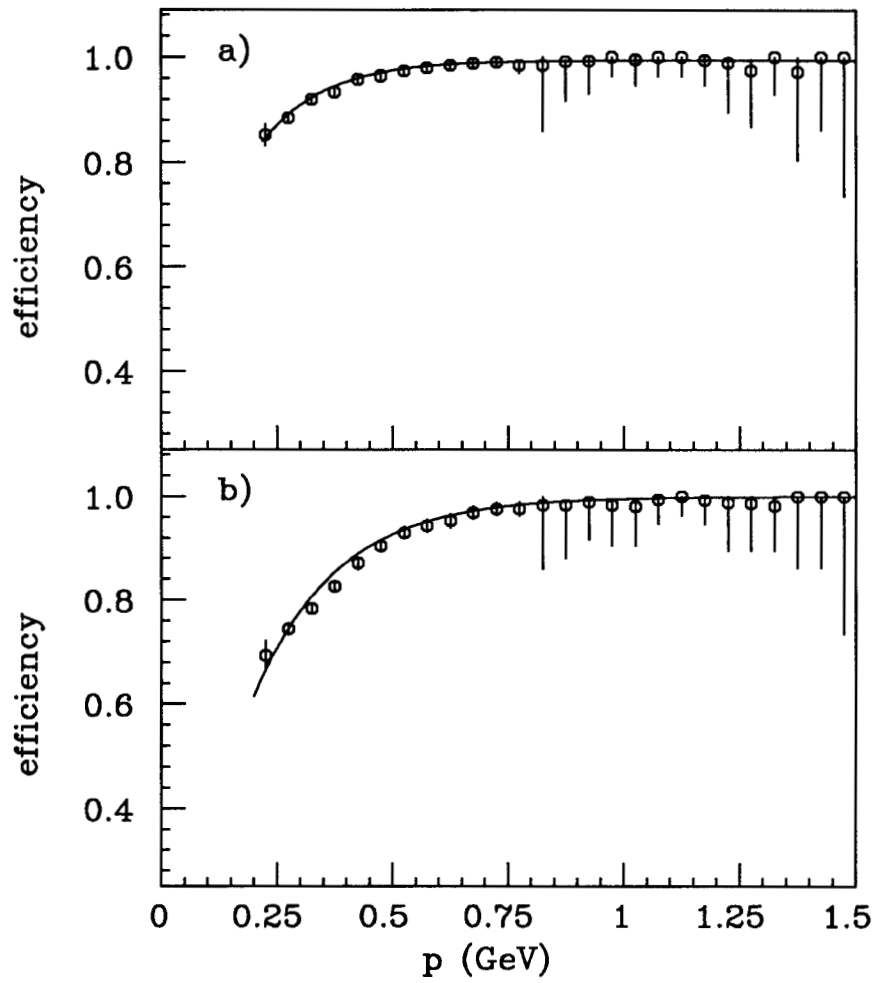

Figure 4.7. The shower counter layers-1,2 biased latch efficiency as a function of the measured momentum for electrons hitting well within the counter boundaries. Figure (*a*) is for layer-1 and (*b*) is for layer-2. The smooth curves represent the EGS Monte Carlo calculations.

through 4.9 is remarkable and indicates that the reason for the inefficiency is well understood and the measurements are correct.

One expects some dependence of the efficiency on the angle of incidence λ of an electron on the counter, because the amount of material that the shower must traverse increases with λ. It is not obvious how much of an effect to expect, however, because once the electron enters the lead, the shower does not propagate only in the original direction of the electron. Further complications are that

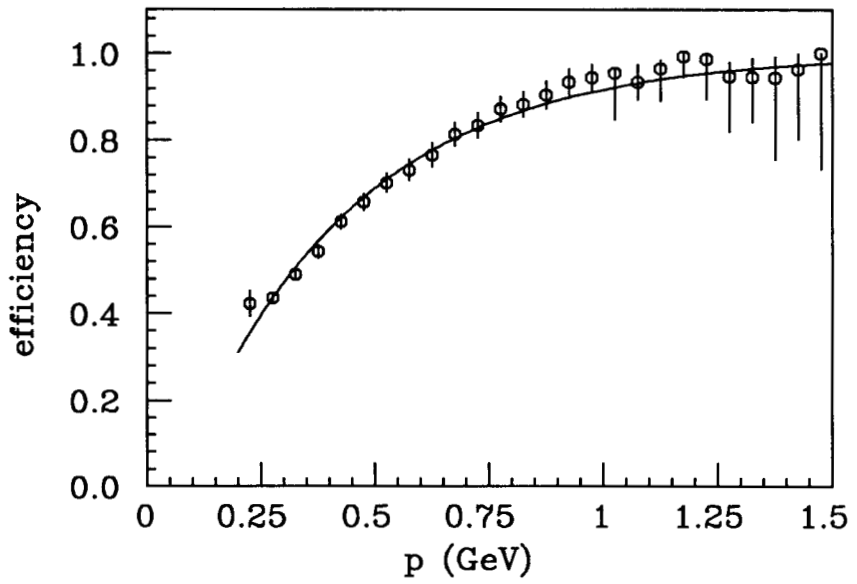

Figure 4.8. The shower counter layer-3 biased latch efficiency as a function of the measured momentum for electrons hitting well within the counter boundaries. The smooth curve represents the EGS Monte Carlo calculation.

the effect may be compensated to some extent by light attenuation and that λ depends on the momentum through the curvature produced by the magnetic field. Figure 4.10 shows the measured efficiency as a function of the angle of incidence. There is only a small deviation from flatness at the largest angles, and in that region the number of events is relatively small. Variations in efficiency with the angle of incidence come from three sources. It varies directly with $\cos\theta$, and it also varies with ϕ because of the hexagonal shape of the shower counter. Then there is some additional variation due to the curvature of the tracks. The latter effect is included in the momentum dependence and must not be double counted. It is not important to include the ϕ dependence of the angle of incidence in detail, but only as an effect uniform with respect to the relevant kinematic variables. That leaves only the dependence on $\cos\theta$ to be concerned with, and in fact no such dependence can be seen in the data or Monte Carlo with the available statistical weight. There is, however, an additional inefficiency of a few percent in the $\cos\theta$

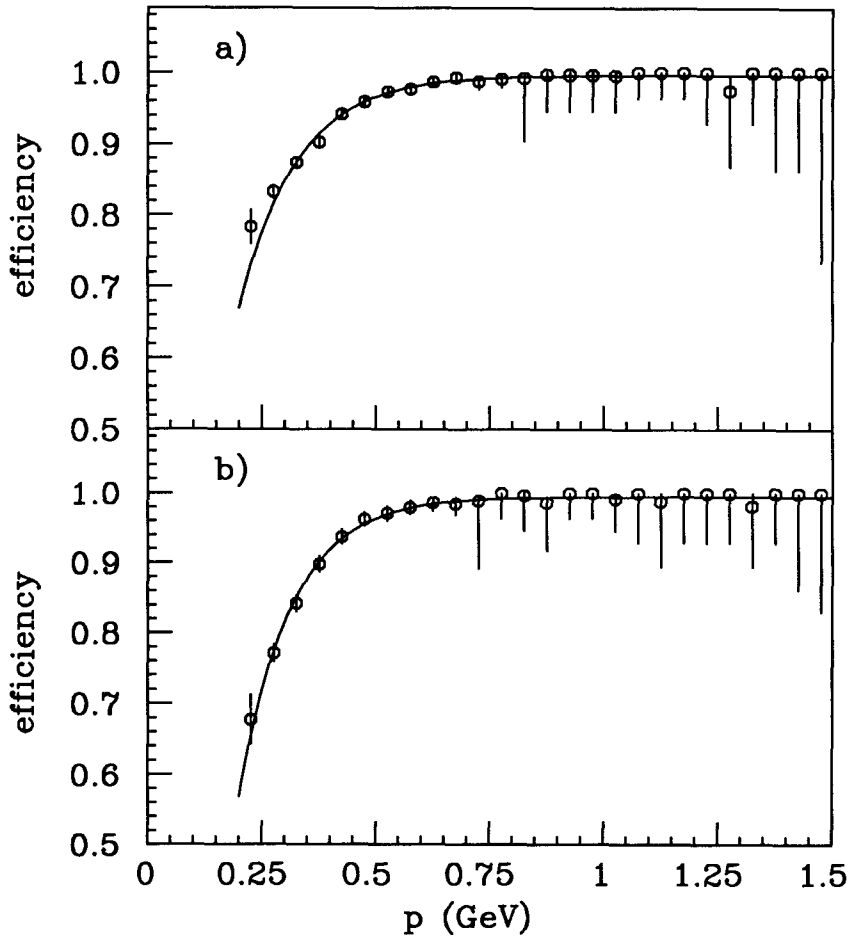

Figure 4.9. The shower counter latch efficiency as a function of the measured momentum for electrons hitting well within the counter boundaries. (*a*) The measured trigger-biased efficiency compared with a smooth curve representing the EGS Monte Carlo calculation. (*b*) The unbiased efficiency as calculated by EGS and fitted to an analytic function.

bins nearest the *center* of the detector. That is understood to be primarily a geometric inefficiency resulting from the small gap at $z = 0$ in layers two and three between the scintillators covering the $+z$ half of the detector and those covering the $-z$ half. It is accounted for by treating separately the regions $|\cos\theta| \leq 0.05$ and $|\cos\theta| > 0.05$.

The Monte Carlo must be used to unfold the true latch efficiency from what has been observed. The goal is to arrive at a parameterization which describes

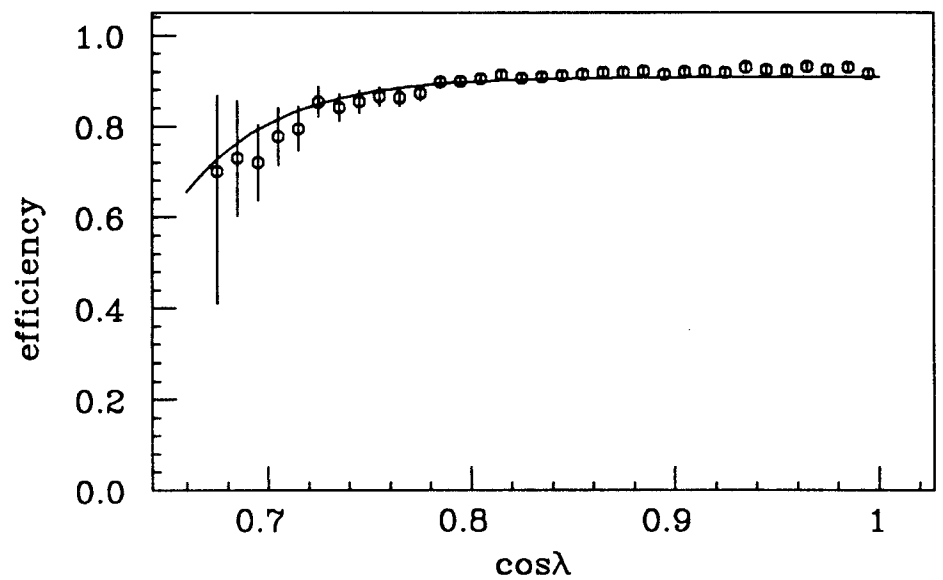

Figure 4.10. The measured trigger-biased shower-counter latch efficiency as a function of the angle of incidence of the electron on the counter. The smooth curve represents the EGS Monte Carlo calculation.

the momentum dependence of the unbiased latch efficiency with an accuracy as good as the statistical precision of the data. That is done in two steps. First, the EGS Monte Carlo is used to calculate the unbiased latch efficiency as shown in Fig. 4.9*b*, and fitting it to the form of Eqn. 4.2 yields the results $A = 0.995$, $p_0 = 0.161$, and $\tau = 0.116$.

To achieve the required precision, the parameterization must be adjusted to give the best possible agreement with the histogram of the biased latch efficiency measured from data. As already mentioned, the efficiency varies slightly in the data over time, so what is done is to adjust the parameterization until agreement is reached with a histogram accumulated using all of the data. Thus the result represents an average efficiency.

The trigger bias in the latch efficiency depends on the momenta of both particles, so it is not trivial to calculate the biased efficiency when given the parameterization of the actual efficiency. What is done is to use the EPA Monte Carlo event generator to produce events with the same momentum and angular

distributions as are observed in the data. For each Monte Carlo electron track, the efficiency parameterization is used along with a uniform random number to decide whether the shower counter will latch. Then a histogram of the biased latch efficiency can be accumulated, just as is done for the data, as a function of the electron momentum. That is done for each of 100 pairs of values for p_0 and τ forming a 10×10 grid about the values obtained from the EGS shower simulation, and the pair is chosen which gives the best fit. Figure 4.11 shows the result, where the Monte Carlo distributions giving the best fits have been plotted over the data. The final values for the parameterization of the shower counter latch efficiency are given in Table 4.3.

4.6 Summary of Cuts Made on Untagged Electron Pairs

Many cuts were made on the data, but only a few are very significant in the sense that they reject a sizable fraction of the events. No background of any sort can be seen in the sample of electron pairs from data, and it is difficult to conceive of any source of background beyond the negligible contamination of muon pairs which sneak in due to noise in the Čerenkov counters. For example, let us consider radiative Bhabha scattering. For the two final-state electrons to be within the angular acceptance, the boost of the final e^+e^- system must have $-0.6 \leq \beta \leq 0.6$. That limit is reached if one of the incoming beam electrons radiates 75% of its energy, and the resulting minimum invariant mass of the final e^+e^- pair is 14.5 GeV—far enough above the 2.6 GeV cut used in this analysis to give absolutely no background. If both beams radiate photons of equal energy, then the final e^+e^- pair could have a mass below the cut. That process is the same order in α as the four-electron final state, but in order for both electrons to be scattered into the DELCO acceptance, the two radiated photons would have to have large and almost equal energies. Although a complete calculation has not been done, the cross section into the DELCO acceptance is believed to be negligible.

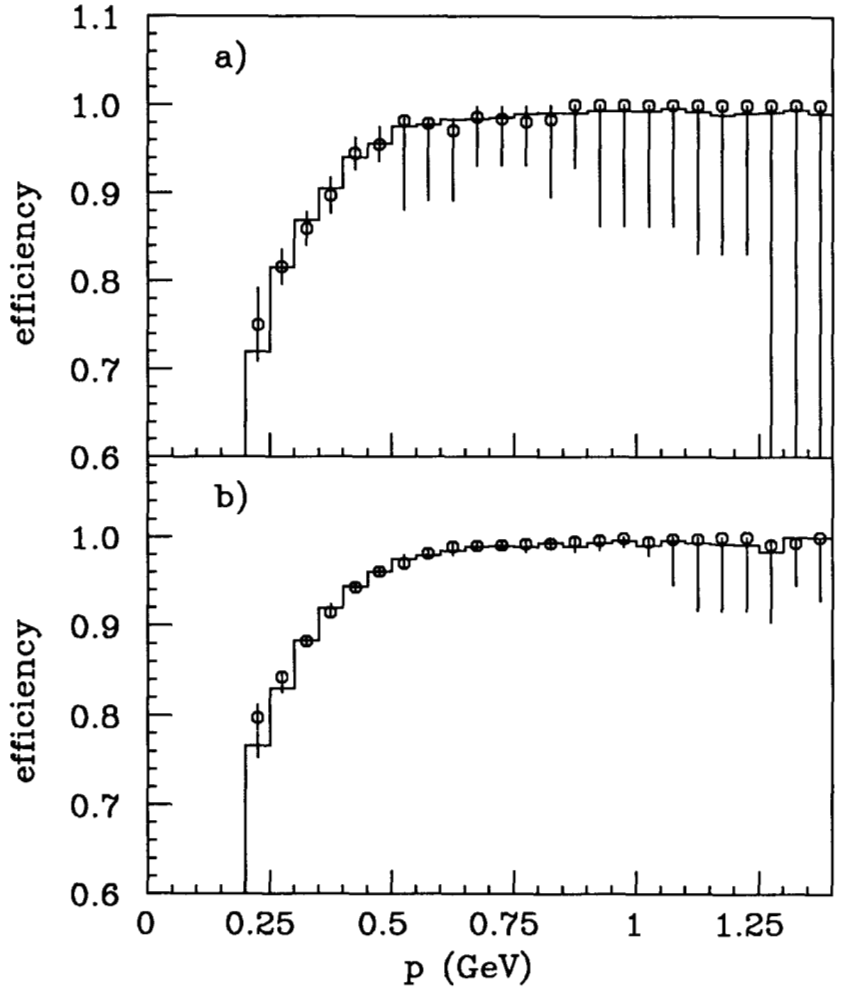

Figure 4.11. The biased shower counter latch efficiency as a function of the electron momentum, including all available data. The solid histograms are from a Monte Carlo calculation including a simulation of the trigger, where the input unbiased latch efficiency is taken to be the parameterization which yields the best fit (a) for $|\cos\theta| \leq 0.05$ and (b) for $|\cos\theta| > 0.05$.

Another possible source of background is tau-pair production. The Monte-Carlo generator used to estimate it includes QED radiative corrections,[33] weak interactions, and all known decay channels for the tau.[34] Of 4508 tau-pairs generated and simulated in the detector, only one produces an electron pair which passes all of the analysis cuts. When normalized to the integrated luminosity of the data, this gives an estimate of only four background events from tau-pair

Table 4.3. A parameterization of the shower counter latch efficiency. The symbols A, p_0, and τ refer to variables in Eqn. 4.2.

$\lvert\cos\theta\rvert_{\min}$	$\lvert\cos\theta\rvert_{\max}$	A	p_0	τ
0.0	0.05	0.995	0.160	0.116
0.05	0.60	0.995	0.154	0.110

production, which clearly is negligible.

Because there is no background, the cuts made after separation of electrons from muons have only two purposes. Most serve to define the kinematic region to be observed and the usable fiducial region of the detector. Then there are some which only discard long, low tails in the distributions of some measured variables in order to avoid events with large, non-gaussian measurement errors.

The last category is comprised of several cuts on the tracking of charged particles. Each track is required to have associated with its fit at least 12 total hits in the inner cylindrical tracking chambers, and track fitting must be completed without any catastrophic errors. Each track must project back to within 0.5 cm of the beamline, and the average of the z-positions of the points on the tracks closest to the beamline must be within 4.0 cm of the interaction point. The cuts on the total transverse momentum, $k_\perp < 0.3\,\mathrm{GeV}$ and $k_\perp < 0.2W$, also reject poorly measured events.

The fiducial volume is defined by requiring each track to have $|\cos\theta| < 0.6$ and to intersect a shower counter module. The cuts on $k_\perp$ along with the requirement that there be no more than 4 GeV of energy measured in the luminosity monitors restrict the measurement to events with quasi-real photons. The Pass-1 filter cut which requires at least one track with a rough p_t measurement, from the first stage of pattern recognition, greater than about 0.20 GeV is superseded for simplicity by a hard cut requiring at least one track to have a fitted transverse momentum greater than 0.25 GeV. Finally, the kinematic range which is accessible without

unreasonably large trigger effects is $W \geq 0.6\,\mathrm{GeV}$. The upper limit on W is roughly determined by the decrease in statistics with higher energies and by the muon Čerenkov threshold and is set at 2.6 GeV. Table 4.4 lists all of the cuts along with the number of events rejected by each. The cuts listed in Table 4.4 have been preceded by those of the Pass-1 filter and the two-photon classification-filter, but in all cases the Pass-1 and classification cuts are superseded by the final analysis cuts.

4.7 The Monte Carlo Simulation

After making the cuts on the data as listed in the previous section, it is possible to simulate adequately all aspects of the detector response relevant to the kinematic distributions without making a detailed simulation of all of the detector apparatus. That has the advantage of requiring far less computer time, which can be significant when so many events are involved, but more important is the fact that no program exists which can properly reproduce, from first principles, the Čerenkov and barrel-shower efficiencies to the accuracy required. Instead, those have been measured from data, and it is a simple matter to put the resulting parameterizations directly into the Monte-Carlo integration.

To proceed, the EPA Monte-Carlo program is used to generate events of equal weight, using the cross section for production of relativistic electron pairs from pairs of real photons:

$$\frac{\mathrm{d}\sigma}{\mathrm{d}u\,\mathrm{d}W} = \frac{2\pi\alpha^2}{W^2} \cdot \frac{1+u^2}{1-u^2}\,, \qquad u \equiv \cos\theta_{\mathrm{cms}}\,. \tag{4.3}$$

The momenta are smeared by gaussian random numbers, using the widths determined in Section 3.1. The trigger is simulated by using the parameterizations of tables 4.2 and 4.3 for the Čerenkov and barrel-shower latch efficiencies. In each case, a uniform random number is generated between 0 and 1, and the event is rejected if it is greater than the efficiency calculated from the parameterization. Similarly, the electron identification efficiency is simulated according to the

Table 4.4. List of the final cuts for $e^+e^- \to e^+e^-e^+e^-$. A total of 398,936 events were read from the tape of skimmed two-particle events, and 41,328 pass all of the cuts. Excepting the first and the last two cuts, the fourth and fifth columns give respectively how many events would be killed by the cut before all other cuts and how many would be killed after all others. "BSC acceptance" refers to the requirement that both tracks pass through barrel shower counter modules, as determined by the drift chamber tracking.

Quantity	Lower limit	Upper limit	Failures when first	Failures when last	Failures in order
Čerenkov ph.	1.5 pe	∞			217405
$\bar{z}$	−4.0 cm	4.0 cm	408	86	408
impact parameter	0	0.5 cm	5823	234	5773
fit errors	0	0	220	22	150
inner DC hits	12	16	3950	883	3129
$\mathrm{MAX}(p_t^1, p_t^2)$	0.25 GeV	∞	50120	1	47304
$k_\perp$	0	0.3 GeV	7541	257	6714
$k_\perp/W_{ee}$	0	0.2	50184	7273	29346
$\cos\theta$	−0.6	0.6	29011	11598	15398
W	0.6 GeV	2.6 GeV	105743	23155	23695
p	0	1.7 GeV	815	3	3
BSC acceptance					8253
$\sum_i Q_i$	0	0			2

parameterization of Table 4.1, and the effect of requiring each track to intercept a shower counter is reproduced by the parameterization

$$\varepsilon(p) = 0.092 \cdot \left[1 - 0.6 \exp\left(-\frac{(0.65 - \cos\theta) - 0.043}{0.012}\right)\right], \tag{4.4}$$

which is obtained from a fit to Fig. 4.2.

Finally, kinematic cuts are made just as they were for the data. In summary, both particles must have $-0.6 \leq \cos\theta \leq 0.6$, and at least one particle must have a transverse momentum greater than 0.3 GeV. The vector sum of the transverse momenta must satisfy $k_\perp < 0.3\,\mathrm{GeV}$ and $k_\perp/W < 0.2$, and the electron-pair invariant mass is restricted to the range $0.6 \leq W \leq 2.6\,\mathrm{GeV}$. The histograms resulting from simulated events may be compared directly with those from data. As examples, Fig. 4.12 shows the electron-pair invariant mass distribution, and Fig. 4.13 shows the angular distribution of the electrons in the laboratory and $\gamma\gamma$ center-of-mass systems. Also, in Fig. 4.13, $\cos\theta_{\mathrm{lab}}$ for each entry is multiplied by the measured charge to demonstrate the charge symmetry. There are 41,328 events from the data sample and twice that from Monte Carlo. To compare the distributions, the Monte Carlo result simply is renormalized to the same number of events as in data, because there is no process by which the integrated beam luminosity can be measured accurately enough to allow an absolute normalization. In fact, it is this QED process which is used to normalize all other measurements in this study.

Figures 4.12 and 4.13 indicate that the data do agree well with the theory. However, it is desirable to present the final results in a way which is independent of the many small details of the acceptance which are peculiar to this experiment.

4.8 Unfolding Detector Effects

It is useful to present the measured spectra with corrections made for systematic detector effects. However, we do not wish to go to extremes and

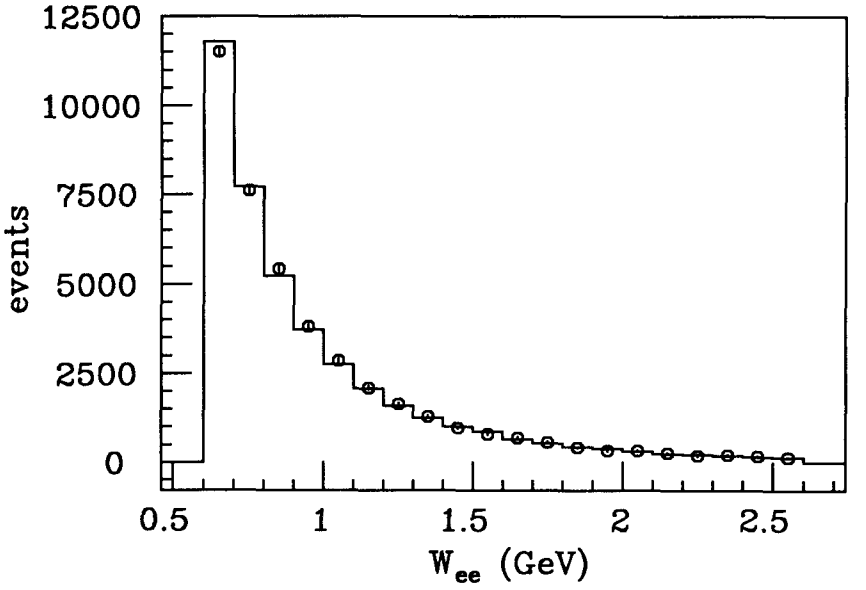

Figure 4.12. The electron-pair invariant mass distribution with all detector effects included. The points are from data, while the line represents the Monte Carlo simulation.

try to extrapolate the data to an acceptance of 4π steradians or down to the minimum invariant mass, for what has been measured is only a very small part of the total cross section of 10^7 nb. Instead, it is appropriate to specify only a minimal number of acceptance cuts within which the theoretical distributions are to be calculated. Then by correcting for all detector effects except for those acceptance cuts, the desired distributions are unfolded from the data. Since there is no absolute normalization which can be used, the results simply are normalized to the areas under the distributions. Therefore, the absolute scale of cross section displayed on a plot does not represent a measurement but only the theoretical calculation. Only the shapes of the distributions have been measured to high precision.

For untagged electron-pair production, there are only five independent kinematic variables, which are taken to be the set Q_i^2, W, y, and $\cos\theta_{\rm cms}$. The Q_i^2 contribute significantly only to the distribution of $k_\perp$, but that one is very sensitive to resolution effects which are difficult to understand and dominate over

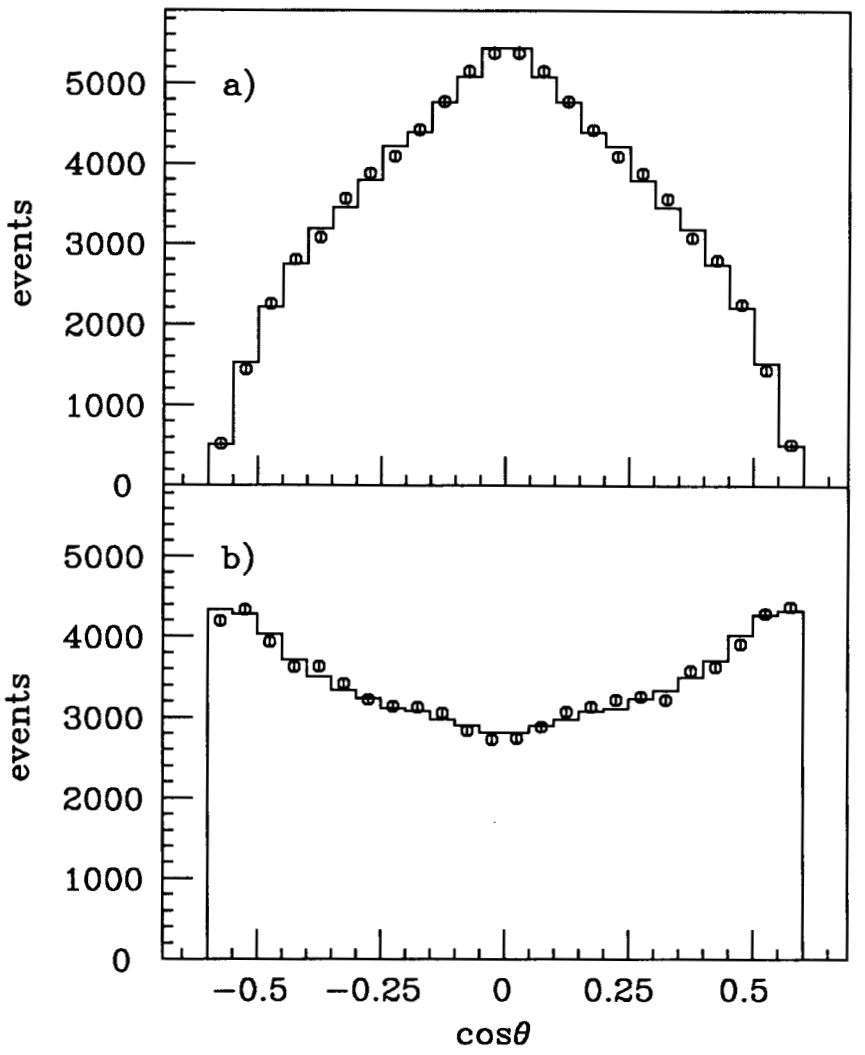

Figure 4.13. The electron-pair angular distributions in (*a*) the $\gamma\gamma$ center-of-mass system and (*b*) the laboratory system, with all detector effects included. The points are from data, while the lines represent the Monte Carlo simulation.

the Q^2 contribution.† Therefore, no attempt is made to unfold the Q^2 dependence from the $k_\perp$ distribution.

It is convenient to use instead of the rapidity, y, a related variable defined by

$$\tilde{\beta} = \frac{\cos\theta_1 \sin\theta_2 + \sin\theta_1 \cos\theta_2}{\sin\theta_1 + \sin\theta_2} . \tag{4.5}$$

† See section Section 3.1 for a complete discussion of this problem.

For the case of minimal Q^2 and ultra-relativistic electrons, $\tilde{\beta}$ is the velocity of the $\gamma\gamma$ system, and $y = \tanh^{-1}\tilde{\beta}$. It has the advantage of being defined only in terms of angles, which DELCO can measure much better than momenta.

The W and $\tilde{\beta}$ distributions are unfolded into the acceptance defined by

$$\begin{aligned} 0.6 \leq W \leq 2.6\,\mathrm{GeV} \\ -0.6 \leq \cos\theta_{\mathrm{lab}} \leq 0.6 \\ k_\perp < 0.3\,\mathrm{GeV} \\ k_\perp/W < 0.2\,. \end{aligned} \tag{4.6}$$

The EPA Monte Carlo and simulation discussed in the preceding section are used to generate an unfolding matrix for each kinematic variable. Each column of such a matrix describes the effects of the experimental resolution and acceptance on a single cubic basis spline. The unfolding program uses the matrix and the corresponding experimental histogram as input and produces the unfolded distribution from those.‡ The results are compared with QED predictions obtained by running the EPA Monte Carlo (identical results are obtained from the Vermaseren Monte Carlo[22]) with only the cuts defined by Eqn. 4.6. The data points which result from the unfolding procedure do not directly correspond to the bins used to accumulate the histograms of Monte Carlo or data and are not even equally spaced. So to compare with data, the Monte Carlo histogram first is interpolated by cubic splines and then integrated over each of the regions defined by the spacing of the points of the unfolded data. That produces Monte Carlo points which directly correspond to those in the data, and from these the χ^2 is calculated to give a measure of the agreement. The difference of the data and Monte Carlo is plotted to give a visual display of the agreement, and the data points also are shown with an overlay of the smoothed Monte Carlo distribution.

‡ See Appendix C for a detailed description of the unfolding procedure.

Figure 4.14 shows the final results for the electron-pair invariant-mass distribution. Note that for all such plots, the horizontal bar associated with a point represents only the region spanned by the point and is not an error bar. The vertical bars give estimates of statistical errors, which vary from about 1% at $W = 0.6\,\mathrm{GeV}$ to 10% at $W = 2.6\,\mathrm{GeV}$. For this case, χ^2 is 19.4 for 14 degrees of freedom (one degree of freedom is lost because of the normalization), which is at the 85% level of the cumulative χ^2 distribution. If the QED calculation is assumed to give the correct description of the data and the errors truly have gaussian distributions with widths given by the error bars, then there is a 15% probability for the χ^2 value to be larger than what has been measured.

For the shape of the invariant mass distribution, the dominant systematic error comes from the correction necessitated by the trigger inefficiency. That error is limited by the statistical accuracy to which the trigger efficiency can be measured by using all of the data and is about 1% for the first invariant-mass bin. That is, not surprisingly, the same as the statistical error on the first bin of Fig. 4.14. In fact, it is a good approximation to obtain the total error for each invariant-mass bin by adding in quadrature with each statistical error an equal systematic error. The agreement between Monte Carlo and data is fairly good even with only statistical errors included, so it is clear that after adding systematic errors there is no evidence for any discrepancy between the data and QED.

Figure 4.15 shows the final results for $\tilde{\beta}$, the velocity of the electron-pair system along the beam axis. This quantity is, to an excellent approximation, uncorrelated with the invariant mass, so it makes sense to quote a value of χ^2 in addition to and independent of that already given for the invariant mass. For 14 degrees of freedom, the χ^2 is 10.4, which is at the 27% level of the cumulative distribution.

For the $\cos\theta$ distribution in the laboratory system, there are some systematic errors in the shape near the center and the two ends due to corrections for the

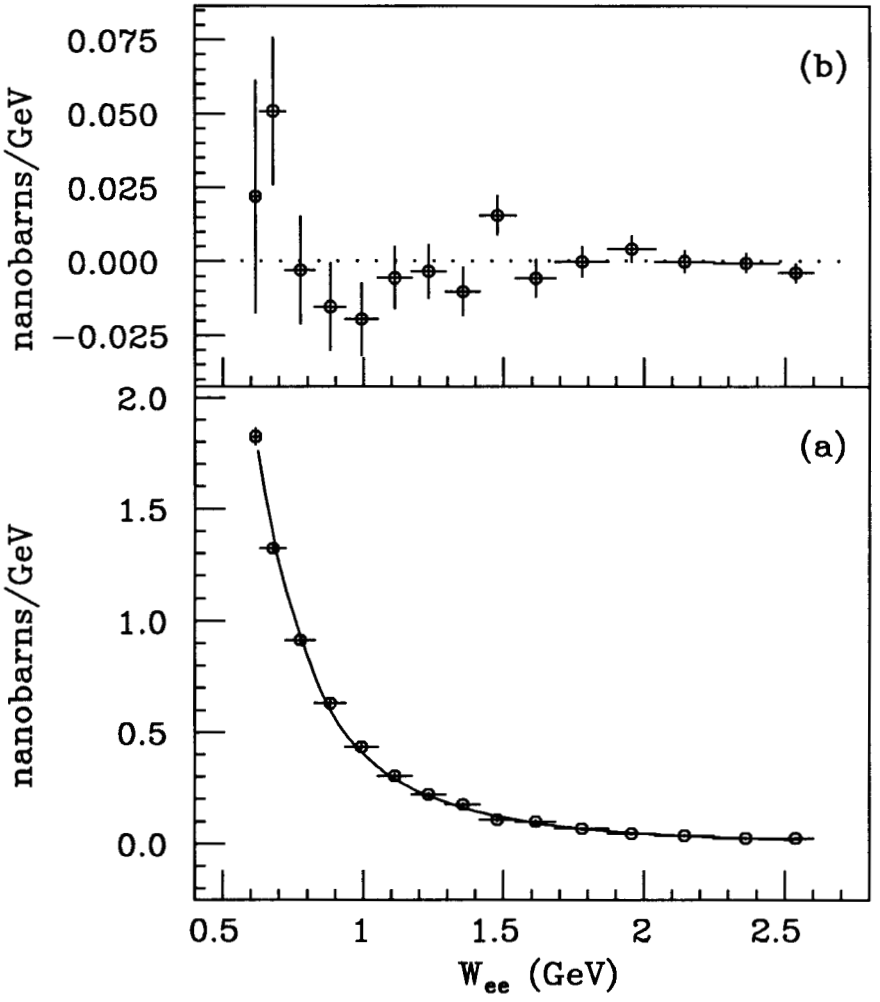

Figure 4.14. The electron-pair invariant-mass distribution with most detector effects unfolded. (*a*) The difference of the data and the QED prediction calculated by the EPA Monte Carlo. (*b*) The data points compared with a smooth curve representing the QED prediction.

detections efficiency, which has significant variations in those regions. The errors in the corrections are only about 2% in the center ($|\cos\theta| \leq 0.05$) and 1% at the ends ($|\cos\theta| > 0.55$). Such errors have no observable effect on the shapes of the angular distribution in the center-of-mass system and the distribution of $\tilde{\beta}$, since the limited region of error in $\cos\theta$ gets mapped over a large region of the other variables. Therefore, we expect that the $\tilde{\beta}$ distribution should agree well with QED after considering only statistical errors, and that is indeed the case. Again

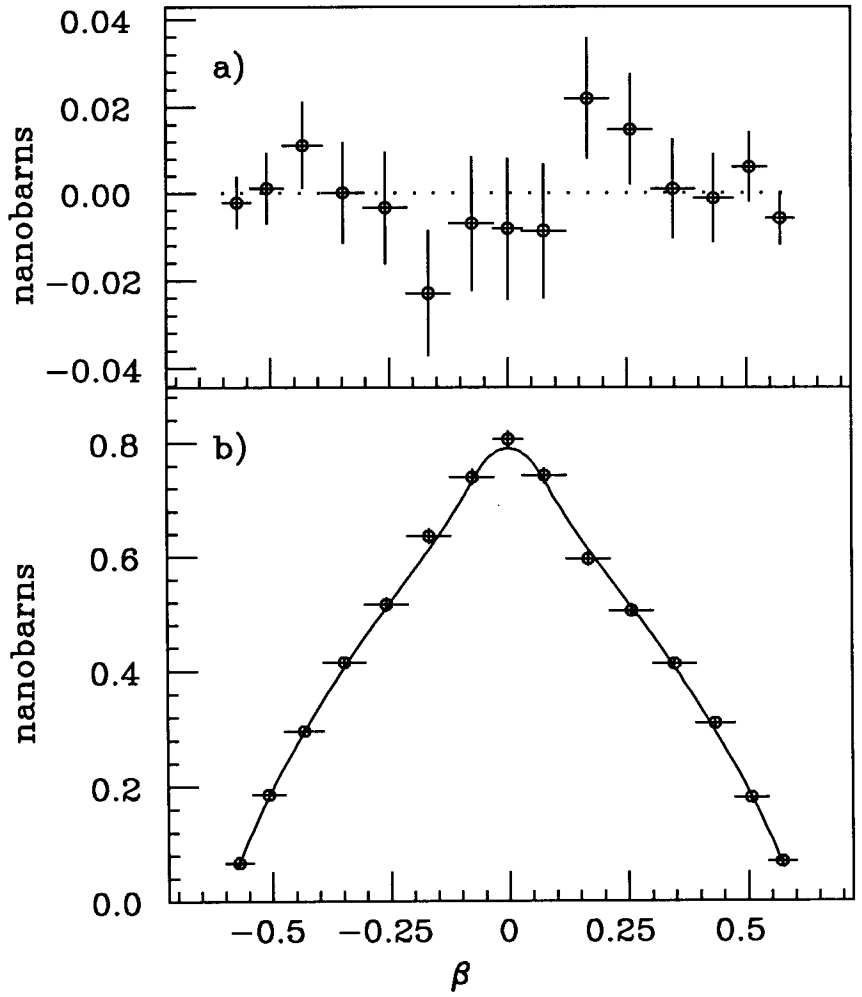

Figure 4.15. The velocity, $\tilde{\beta}$, of the $\gamma\gamma$ electron pair with most detector effects unfolded. (*a*) The difference of the data and the QED prediction calculated by the EPA Monte Carlo. (*b*) The data points compared with a smooth curve representing the QED prediction.

there is no evidence for any discrepancy between the data and QED.

The last result to present is for the center-of-mass angular distribution. For this case it is desirable to see the results free from the effect of the acceptance cut made on the laboratory angle. Therefore the results are unfolded into an acceptance the same as defined in Eqn. 4.6, except that the cut on the laboratory angle is replaced by a cut on the center-of-mass angle: $-0.6 \leq \cos\theta_{\rm cms} \leq 0.6$. Figure 4.16 shows the result, which is compared with the theoretical shape given

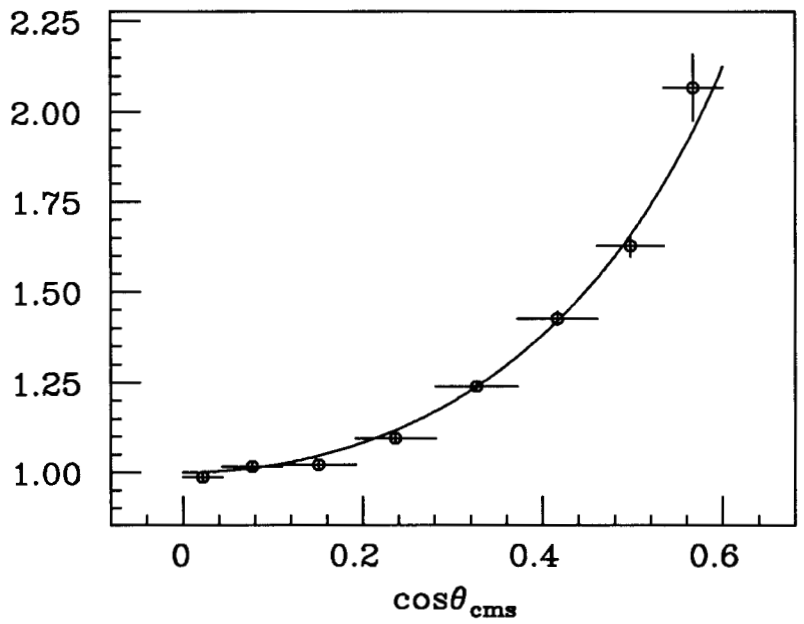

Figure 4.16. The center-of-mass electron-pair angular distribution with most detector effects unfolded from the data. The smooth curve is given by $(1+\cos^2\theta)/(1-\cos^2\theta)$.

by Eqn. 4.3. It is clear that even with a severe acceptance cut made in the laboratory frame, the high statistics available allows us to see quite clearly the center-of-mass angular distribution, which is in excellent agreement with QED.

4.9 Measurements of Tagged $e^+e^- \to e^+e^-e^+e^-$ Events

The sample of untagged events is dominated by collisions of quasi-real photons with Q^2 not much larger than the square of the electron mass. In order to study collisions of more virtual photons without any contribution from pairs of quasi-real photons, it is necessary to be able to detect at least one of the scattered beam electrons. Because of the factor of $1/q_1^2q_2^2$ in the cross section given by Eqn. 2.12, to get a reasonable level of statistical precision, the analysis is restricted to events with a single luminosity counter tag.

4.9.1 *Analysis of the Luminosity-Counter Energy*

In DELCO, the only devices able to detect particles at very small angles with respect to the beam are the counters of the luminosity monitor. The inner and outer counter surfaces parallel to the beamline form hexagons about the beam pipe, and the counter surface into which the scattered electrons are incident is perpendicular to the beamline and subtends a range of polar angles, with respect to the interaction point, from 27 mrad to 94 mrad.† That corresponds to a range of Q^2 from $0.13\,\mathrm{GeV}^2$ to $1.9\,\mathrm{GeV}^2$. However, each counter is a lead-scintillator sandwich segmented into six azimuthal segments with no radial segmentation, and there is no tracking information in front of the counters. Therefore, it is not possible to measure from the luminosity-counter tag what is the Q^2 of the radiated virtual photon, except to say that it is between the above limits.

There is some noise background in the luminosity counters, primarily from synchrotron radiation, but even without any charged-particle tracking, the signal is well separated from the noise. The algorithm used to analyse the luminosity counter energy deposit is simple. For each counter, one at each end of the detector, a search is made over the six sextants to find the one with the largest energy deposit. The energy then is summed over that sextant plus the two adjacent sextants to give the quantity used in the analysis. Figure 4.17 shows a histogram of the luminosity counter energy deposit for four-electron events. The counters have been calibrated such that the position of the peak remains constant with time, but the absolute energy scale is somewhat arbitrary. In fact, the Vermaseren QED Monte Carlo[22] predicts that the median energy of the scattered electrons, for tagged events within the DELCO analysis acceptance, is 13.7 GeV, with 95% of the energy deposits within 0.6 GeV of that value. A Monte Carlo calculation for Bhabha scattering, including radiative effects,[33] predicts that the median energy deposit for Bhabha electrons is 14.45 GeV, with 95% of the energy deposits above

† These limits refer to the inscribed and circumscribed radii of the scintillation counter covering the entire shower counter face into which the electrons are incident.

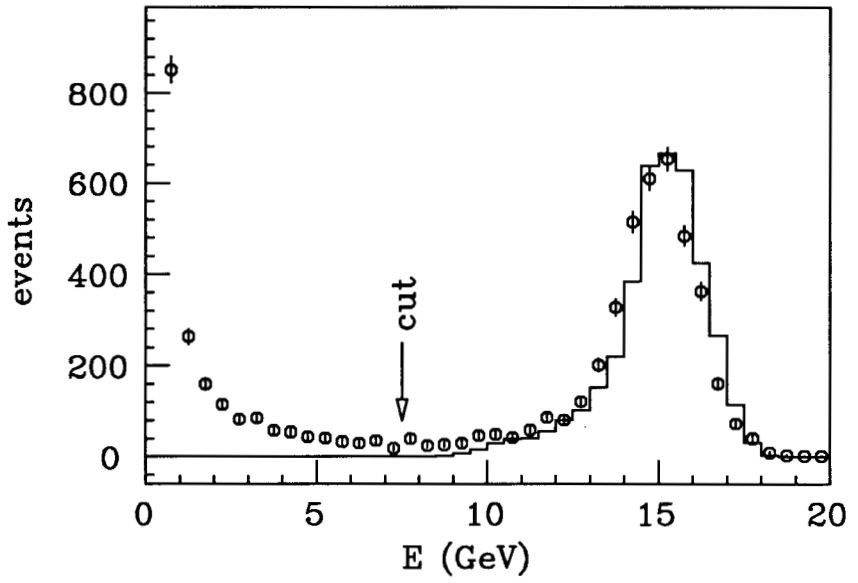

Figure 4.17. The luminosity counter energy deposit. The points are four-electron events, while the solid line is from Bhabha scattering.

13.45 GeV. Bhabha events do not suffer from much contamination of synchrotron radiation because they all have two back-to-back luminosity counter hits, while only a small fraction of the four-electron events have even one luminosity-counter hit. Therefore, the Bhabha events give some idea of what the low-energy side of the tag peak should look like. In Figure 4.17, a histogram of the measured Bhabha-electron energy, multiplied by 0.95, is plotted as a solid line over the points from the four-electron data.

Tagged events are defined as those with *one* luminosity counter with energy greater than 7.5 GeV. Judging from the histogram of Fig. 4.17, we estimate that there is a maximum background from the tail due to noise of about 60 events and a maximum loss of about 50 events from the signal. There are 4051 entries above the cut (the histogram includes only about half of the data), so the conclusion is that the cut causes an uncertainty in the absolute normalization of no more than $\pm 1.5\%$. However, the relative normalization of pions, muons, and electrons is not affected, because all of the tagged events are analyzed with the same cut.

4.9.2 *Measured Kinematic Distributions*

Once the cut on luminosity counter energy has been chosen, the remainder of the analysis of tagged four-electron events proceeds almost the same as the untagged analysis. All other analysis cuts are the same, except that there is no cut on the total transverse momentum, $k_\perp$, for the tagged events. In this section we compare only the shapes of the measured distributions with those generated by the Vermaseren Monte Carlo program.

The acceptance of the luminosity counters is not well known, both because of inaccurate positioning and edge effects of electromagnetic showers, so there is some error in the Monte Carlo program due to integrating over an incorrect range of Q^2. In fact, the shapes of the invariant-mass and angular distributions for the two electrons observed in the central detector are not sensitive to that effect within the available statistical resolution. One distribution for the two electrons which is very sensitive to Q^2 is that of the total transverse momentum $k_\perp$. In fact, $k_\perp^2$ is approximately proportional to Q^2 for single-tag data. For untagged data, the $k_\perp$ distribution is dominated by the detector resolution, but that is not the case for the single-tag data, where most events have $k_\perp$ greater than 0.4 GeV.

Figure 4.18 shows the measured $k_\perp$ distribution compared with QED predictions for two assumptions about the luminosity-counter acceptance: (*a*) using the measured size and location of the face of the counter, and (*b*) using the same geometry, but with the inner and outer edges moved radially inward by 0.9 cm. One can see that the *effective* inner edge is almost a full centimeter inside the nominal edge of the counter face. This acceptance, which gives the best reproduction of the observed $k_\perp$ distribution, is used for the following analysis. There is a change of 14% in the cross section when going from the acceptance of Fig. 4.18*a* to Fig. 4.18*b*, but the shapes of all distributions other than that of $k_\perp$ are not significantly affected.

To reproduce the lower edge of the $k_\perp$ distribution in detail would require a complete modeling of the luminosity-counter response, which has not been

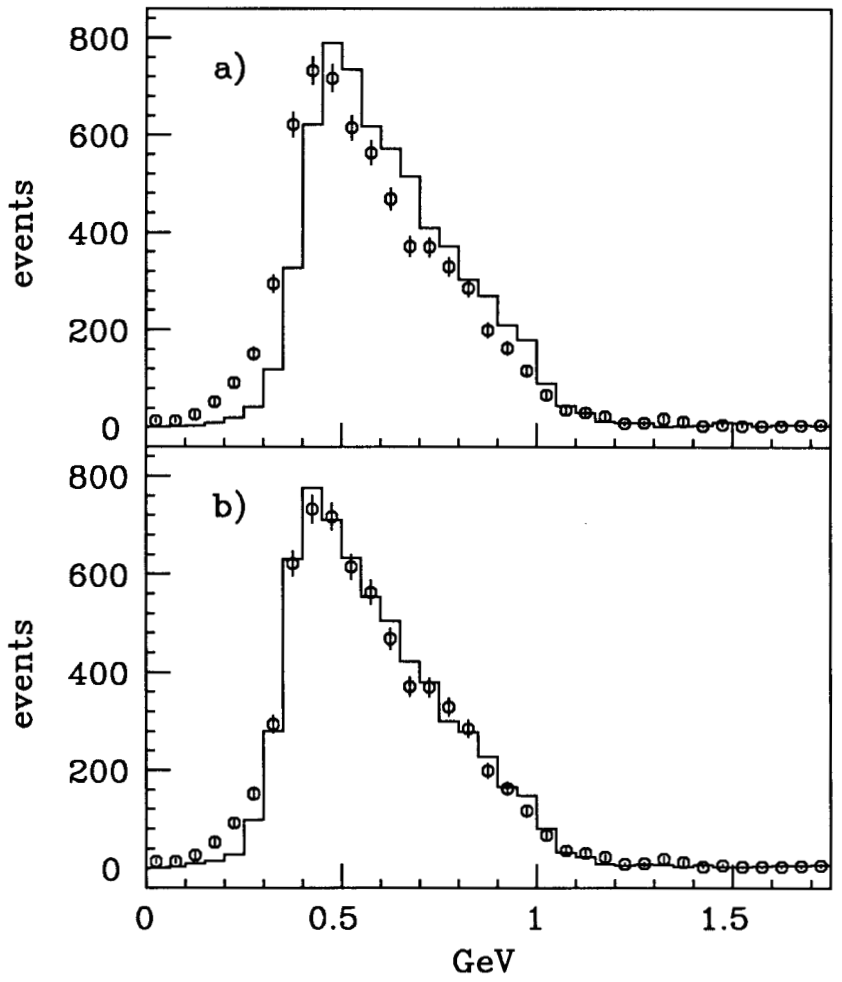

Figure 4.18. The $k_\perp$ distribution for tagged events. The points show the measured distribution of $k_\perp$ of two electrons in the central detector for tagged four-electron events. No corrections are made for detector effects. The solid lines in (*a*) and (*b*) show the QED prediction for two assumptions about the luminosity counter acceptance.

done. Also significant are measurement errors on the counter locations and QED radiative effects. It is important to emphasize that such a detailed analysis is not necessary for anything except to reproduce in detail the $k_\perp$ distribution. In particular, the relative normalization between events with electron pairs in the central detector and those with muon or hadron pairs in the central detector is not at all affected by the lack of detail in modeling the luminosity counters.

Figure 4.19 shows a comparison of the measured electron-pair invariant-mass

distribution with the QED prediction from the Vermaseren Monte Carlo. The points are unfolded from the measured distribution, into an acceptance defined by $0.6 \leq W \leq 2.6\,\mathrm{GeV}$ and $-0.6 \leq \cos\theta_{\mathrm{lab}} \leq 0.6$ for the pair of electrons in the central detector. Also, one of the scattered beam electrons must pass through a plane perpendicular to the beam, 282 cm from the interaction point, within the region between two hexagons concentric with the beam, where the inner hexagon has an inscribed radius of 6.82 cm, and the outer hexagon has a circumscribed radius of 23.08 cm. Figure 4.20 shows the comparison for the laboratory-system angular distribution of the two electrons observed in the central detector. Both distributions are in complete agreement with the QED prediction within the statistical error bars. The systematic errors are the same as for the untagged analysis, and in this case they are completely negligible compared with the statistical uncertainty.

4.10 Measurement of the Integrated Luminosity

Up to this point, the discussion has been limited to comparing the measured shapes of various distributions with QED predictions. It also is possible to measure absolute cross sections as long as there is an independent measurement available of the colliding-beam time-integrated luminosity (hereafter often referred to simply as luminosity or represented by the symbol $\mathcal{L}$). For DELCO, the best independent measurement of the luminosity comes from the process $e^+e^- \rightarrow \mu^+\mu^-$. In this section, the luminosity is measured using untagged events from the process $e^+e^- \rightarrow e^+e^-e^+e^-$ and compared with the result from a measurement of $e^+e^- \rightarrow \mu^+\mu^-$.

The error in such a measurement is completely dominated by systematic effects, so it is of no advantage to choose cuts which allow in the maximum number of events. Nor is there any advantage even to use all of the data, so this discussion is restricted to the data accumulated during *1983*. Some systematic effects differ slightly for other data, so it is more confusing to consider all of the

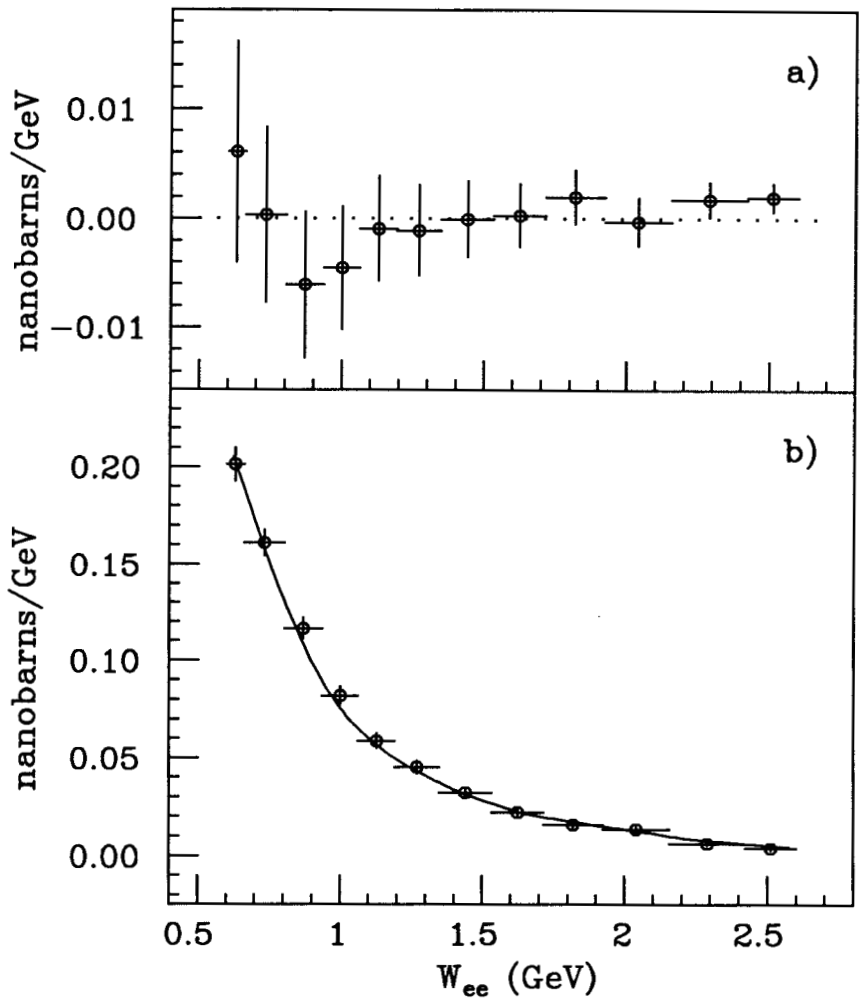

Figure 4.19. Electron-pair invariant mass for tagged events The data points are corrected for most detector effects. (*a*) The difference of the data and the QED prediction. (*b*) The QED prediction plotted as a smooth curve over the data.

data simultaneously. The other data have been checked separately, and the results are consistent with those presented here. The *1983* data are specifically chosen because for them the most complete information is available on the $e^+e^- \to \mu^+\mu^-$ measurement.

Most of the cuts used are identical to those of Section 4.6. The most important exception is that here only those events are kept in which both tracks extrapolate to a point at least 1 cm inside of the edge of a shower counter, rather than just

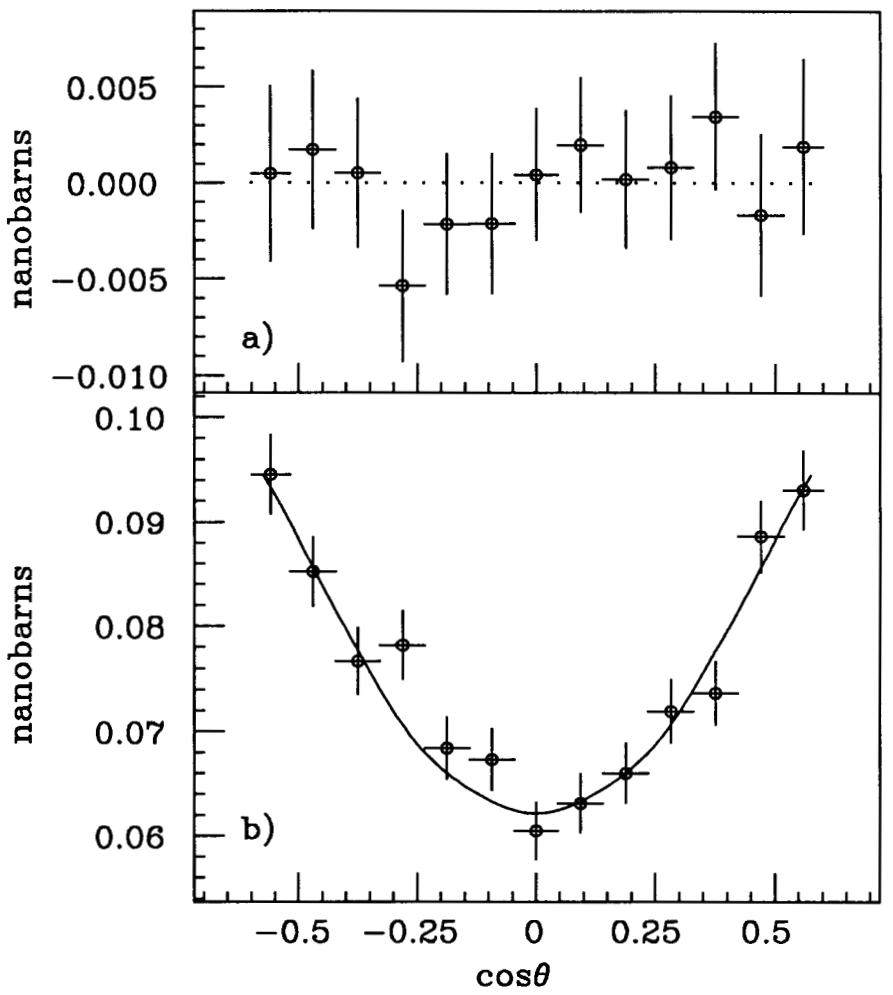

Figure 4.20. Angular distribution for e-pairs from tagged events. The data points are corrected for most detector effects. (a) The difference of the data and the QED prediction. (b) The QED prediction plotted as a smooth curve over the data.

inside. That is done in order to eliminate errors due to the detector survey or to the simulation by EGS of the edge effects. Also, the lower limit for W is taken to be 0.7 GeV, rather than 0.6 GeV, in order to avoid the region of the worst trigger problems, and events with either track within the region $|\cos\theta| < 0.05$ are discarded to avoid large corrections for the electron identification efficiency. The latter two changes are not essential, since the known corrections are adequate, but they are safe and do not harm the statistical accuracy.

After removing seven short runs for which no information is available from the luminosity monitors, the number of events from data which pass all cuts is 10,380. Several Monte Carlo tapes have been generated using the EPA Monte Carlo and a full simulation of the detector, including the use of EGS for the beam-pipe and drift chamber material and for the shower counter. The total generated luminosity is $26.5\,\mathrm{pb}^{-1}$, which yields 4621 events after all analysis cuts are made.

Before quoting the measured luminosity, a number of small corrections must be made. They are due to various effects which are seen in the data but are not simulated in the Monte Carlo. The first concerns the requirement that exactly two tracks be seen in the inner drift chambers. Occasionally, extra tracks are produced either by noise hits in the drift chambers or by low momentum electrons from electromagnetic interactions in the beam pipe and drift chamber material. Such events can be found by considering all those with greater than two tracks and making pictures of those in which a subset of two tracks passes all of the analysis cuts. When that is done, 90% of the resulting events clearly are due to the hypothesized effects, and the remainder are consistent, but not certain. One finds that $0.7 \pm 0.2\%$ of the signal is lost due to extra tracks being produced in the beam pipe, compared with 0.65% in the Monte Carlo. Another 0.7% is lost due to tracks being produced from noise hits. That effect is not simulated at all, so a correction to the luminosity of $+0.7 \pm 0.3\%$ is necessary.

The electron identification has not been simulated in the Monte Carlo. Excluding the bins for $-0.05 < \cos\theta < 0.05$, which are not included in this analysis, the efficiency found from Fig. 4.5 is 0.994. Since both tracks in each event in the data must be identified, then that efficiency must be squared. To account for this effect, the luminosity is corrected by $+1.2 \pm 0.5\%$.

The noise in the luminosity counters is not simulated in the Monte Carlo, while there is in the data a small loss of events due to noise greater than the 4 GeV cut imposed to reject tagged events. That loss has been estimated by extrapolating the observed distribution, which yields a correction to the luminosity of $+1.0 \pm 1.0\%$.

As discussed in Section 3.1, the Monte Carlo appears to give a better momentum resolution than seen in data. That can cause less events to be cut in Monte Carlo by the $k_\perp$ cuts than in data and also may affect the lower cut on the invariant mass. To reproduce the $k_\perp$ distribution seen in data, a gaussian resolution function of width 0.04κ, where κ is the measured track curvature, must be convolved with the curvature measured after the usual drift chamber simulation. When that is done, the number of Monte Carlo events passing all cuts drops to 4576, resulting in a correction to the luminosity of $+1.0 \pm 1.0\%$.

The cuts on the impact parameter and the average z-position each reduce the data by only about 1%, but even fewer events are cut from the Monte Carlo. There is no known background which can be contributing to the tails, so one must assume that the lost events are really part of the signal. These effects are accounted for by applying a correction of $+0.6 \pm 0.6\%$ to the luminosity.

In addition to these corrections, there are a number of other sources of systematic error. The largest is due to uncertainty about the absolute momentum scale of the experiment, which is determined from measurements of the magnetic field. The scale is believed to be accurate to within 1%. Since the invariant-mass spectrum falls like $1/W^3$, and since the luminosity is proportional to the area under the curve and above the lower cut, then the resulting uncertainty in the luminosity is $\pm 2\%$.

A related uncertainty is due to the EGS simulation of the beam pipe and inner drift chamber material. One finds that the calculated effect of bremsstrahlung and other radiative processes in the beam pipe and other material between the interaction point and the tracking chamber volume in which the momentum is measured is to lower the detection efficiency by 13%. Only an insignificant part of that loss is due to such things as the cut on the track impact parameter. About 10% of the loss is due to worsening of the momentum resolution, resulting in more events being cut by the $k_\perp$ cuts. But the major effect is just a downward shift of the average momentum, causing more events to fail the lower cut on

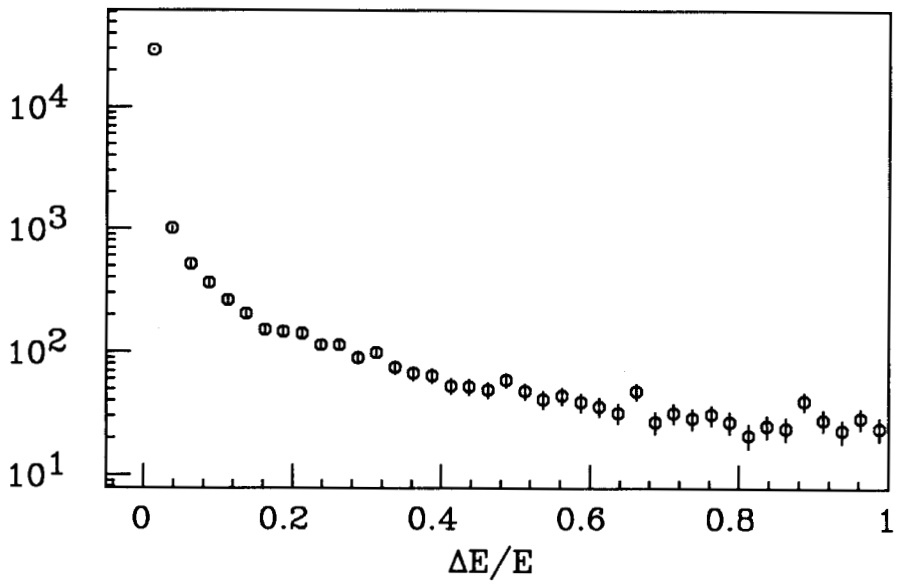

Figure 4.21. The fractional energy loss of electrons passing through 0.029 radiation lengths of aluminum between the beampipe vacuum and the innermost drift chamber gas volume, as calculated by the EGS Monte Carlo simulating *1983* data.

invariant mass. Figure 4.21 gives an idea of how that is possible. It shows the fraction of energy lost by electrons in the Monte Carlo when passing through the 0.0294 radiation lengths of aluminum between the beampipe vacuum and the gas volume of the inner drift chamber. Seven percent of the electrons lose greater than ten percent of their energy, and that is not including the additional 0.0054 radiation lengths of aluminum between the two inner drift chambers. We make a conservative assumption that the EGS calculation is good to at least 15%. Since the correction is 13%, then the systematic contribution to the uncertainty in the luminosity is only ±2.0%.

There is some uncertainty in the simulation of the drift chamber wire efficiency. After all of the other cuts have been made, the distributions of the numbers of hits look closely alike for data and Monte Carlo. In fact, the cut requiring at least 12 hits in the inner chambers reduces the data by 5.2% and the Monte Carlo by 6.3%. It seems safe to assume that the uncertainty from this cut

is no greater than $\pm 1\%$.

There is an additional source of systematic error due to theoretical considerations. All calculations have been done only to leading order (α^4) in QED perturbation theory. The two multiperipheral graphs by far dominate the calculations, so it is important to consider possible radiative corrections to those graphs. Unfortunately, no calculations or Monte Carlo programs are available for the entire set of graphs for the order α^5 corrections. Those corrections include radiation of real photons from any of the seven electron propagators of the leading order graphs, which gives amplitudes of order e^5, and all of the vertex corrections, electron self-energy corrections, and vacuum polarization corrections, which interfere with the leading order graphs to give α^5 contributions in the cross section. Also, there are some entirely new graphs, with five-point functions, which should be included to be completely consistent, but those have been shown to contribute very little to the correction.[35]

The most thorough calculation of these corrections has been done for the related process $e^+e^- \rightarrow e^+e^-\mu^+\mu^-$.[36] Even that calculation neglects the graphs with five-point functions and those with three vertices on the muon line.† As long as no cuts are made which depend heavily on the energies of the scattered beam electrons or on the total neutral energy, which is the case for this analysis, then the differential cross section at each value of $W_{\mu^+\mu^-}$ is found to increase by less than 1% when the corrections are introduced. It is not surprising that the corrections are small, because the Q^2 of the photons are very small, and the momentum transfer is only the order of one GeV. Due to the impracticality of doing the complete calculation, we do not apply any radiative correction, but simply assume that the resulting error is $\pm 1\%$.

Table 4.5 summarizes all of the luminosity corrections and systematic errors. After adding the systematic errors in quadrature with each other and the $\pm 1.8\%$

† Twenty-six diagrams are included, so even with the approximations which are made, the calculation is far from simple.

statistical uncertainty, we arrive at the result:

$$\mathcal{L}^{1983} = 62.2 \pm 2.5\,\mathrm{pb}^{-1}\,. \tag{4.7}$$

Carrying through the exercise for the full data set taken with the isobutane Čerenkov radiator gives a total integrated luminosity of $122.4 \pm 4.5\,\mathrm{pb}^{-1}$.

Table 4.5– List of the sources of error in the luminosity measurement from untagged four-electron data and the associated corrections.

Source of Error	Percent Correction
two-track cut	+0.7 ± 0.3
electron identification	+1.2 ± 0.5
luminosity-counter cut	+1.0 ± 1.0
momentum resolution	+1.0 ± 1.0
impact parameter and z	+0.6 ± 0.6
momentum scale	± 2.0
EGS simulation	± 2.0
wire efficiency	± 1.0
radiative effects	± 1.0
statistical uncertainty	± 1.8

For each of the runs which have been analyzed, there is a luminosity measurement from the small-angle luminosity monitors. Those measurements are not absolute in themselves because of difficulty with understanding the luminosity monitor acceptance. But that acceptance is constant over each run-block, so the measurements do give the relative luminosity for each run. Using them and applying a correction determined from the measurement of $e^+e^- \rightarrow \mu^+\mu^-$,[37] one find that the luminosity to compare with Eqn. 4.7 is $\mathcal{L}^{1983}_{e^+e^-\rightarrow\mu^+\mu^-} =$

$69.8 \pm 3.5\,\mathrm{pb}^{-1}$. If the error estimates for these two results are added in quadrature, then it appears that they disagree by 1.8 standard deviations. However, so far all the contributions to the error estimates have been added in quadrature, and that almost certainly gives an underestimate of the error, even though the individual contributions listed in Table 4.5 are conservative estimates. Adding all the errors in Table 4.5 linearly ($\approx 11\%$) is certain to give an overestimate of the error but would bring the two results into good agreement. It also is interesting that if it is true that the experimental momentum scale is in error by -2%, as indicated by the measurement of $K_s \to \pi^+\pi^-$ (see Section 3.1), then the result in Eqn. 4.7 must change by $+4\%$, which would bring it into reasonable agreement with the muon-pair measurement. These difficulties only underscore the important fact that when using electron pairs to normalize the pion-pair sample, most of the errors listed in Table 4.5 no longer contribute. In particular, any error in the momentum scale cancels. Obviously, none of the errors inherent in the measurement of $e^+e^- \to \mu^+\mu^-$ contribute in that case either.

4.11 Integrated Luminosity from Tagged Events

The measurement of the luminosity can be repeated with tagged events, although then the error is dominated by the lack of knowledge of the luminosity counter acceptance. The analysis of tagged four-electron events is repeated with the same changes that were made to the untagged analysis: the barrel shower counter acceptance is restricted, the center of the detector in $\cos\theta$ is cut out, and the lower limit on the e^+e^- invariant mass is moved up to 0.7 GeV. For the *1983* data, 1826 events pass all the cuts.

Most of the corrections which apply to the untagged analysis apply here as well. One exception is that because no cut is made on $k_\perp$, the uncertainty in the momentum resolution has very little effect. Also, the cut on luminosity counter energy obviously is changed, and it is appropriate to use the systematic error estimated in Section 4.9.1. Table 4.6 gives a list of the necessary corrections

and errors. Note that the error due to the luminosity counter acceptance is not included.

Table 4.6. List of the sources of error in the luminosity measurement from tagged four-electron data and the associated corrections.

Source of Error	Percent Correction
two-track cut	$+0.7 \pm 0.3$
electron identification	$+1.2 \pm 0.5$
momentum resolution	-0.4 ± 0.4
impact parameter and z	$+0.6 \pm 0.6$
luminosity-counter cut	± 1.5
momentum scale	± 2.0
EGS simulation	± 2.0
wire efficiency	± 1.0
radiative effects	± 1.0
statistical uncertainty	± 3.5

When the measured location and size of the face of the luminosity counters is assumed for the acceptance, the measured luminosity is $76.3 \pm 3.7\,\mathrm{pb}^{-1}$. However, we have seen that it does not seem reasonable to assume that acceptance. When, instead, the acceptance is used which gives the best fit to the measured distribution of $k_\perp$ of the two electrons in the central detector, then the measured luminosity changes to $\mathcal{L}_{\mathrm{tag}} = 65.4 \pm 3.5\,\mathrm{pb}^{-1}$. The latter result agrees with the untagged measurement. In spite of the uncertainty about the luminosity counter acceptance, we have seen that everything is in agreement if a reasonable assumption is made about that acceptance. The matter will not be pursued any further, because it is not relevant to the use that will be made of tagged events in the remainder of the analysis.

5. Measuring the Pion-Pair Spectrum

After electron pairs have been removed from the two-track data sample, most of the remaining events are muon pairs and pion pairs produced by $\gamma\gamma$ interactions. DELCO has no capability of distinguishing between pions and muons, but the majority of the events are in fact muon pairs. It is essential to be able to predict their contribution to all of the distributions in order to subtract it. The QED Monte Carlo programs are used with complete confidence to generate the theoretical spectrum of muon pairs. The only remaining problems are to simulate the detector response and normalize the theoretical calculation.

Fortunately, the detector response is easy to understand for muons, compared with electrons or hadrons. In particular, the only trigger effects which must be understood are the geometric limits of the shower counters and the effect of electromagnetic energy loss. The latter is easy to predict for massive particles and simply results in a sharp momentum cutoff, at about 180 MeV for muons.

The normalization requires a knowledge of the luminosity of the colliding beams. That can be predicted from knowledge of the storage ring optics and the measured beam intensity, but not to sufficient accuracy to be of any use to most physics measurements. What generally is done instead is to measure a physics process, resulting from the beam collision, which can be predicted theoretically to the desired accuracy. The obvious candidates are simple QED processes. For studies of e^+e^- annihilation, Bhabha scattering and muon-pair production commonly are used. Those processes, however, result in electrons or muons with energies close to 14.5 GeV at *PEP*, compared with energies of less than 0.5 GeV for most particles resulting from two-photon production. As a result, the systematic effects involved in measuring the two-photon events are completely different from those encountered with Bhabha scattering or muon-pair production, and one can expect uncertainties when extrapolating from high to low energy which will greatly dominate all other errors involved in the pion-pair measurement.

DELCO has the unique ability to use the $e^+e^- \rightarrow e^+e^-e^+e^-$ process for normalization. The results of Chapter 4 demonstrate complete agreement of measurements of several kinematic distributions from this process with QED predictions. One general advantage gained is the similarity of the energy and angular distributions of the electron final state to those of the processes which require normalization. That is especially true for normalization of the process $e^+e^- \rightarrow e^+e^-\mu^+\mu^-$, since when well above the $\mu^+\mu^-$ threshold, the cross section is almost identical to that of the four-electron process. Another important advantage is that the initial state is the same for all processes considered.†

As a result, there are many specific sources of systematic error in the normalization which cancel. If the process $e^+e^- \rightarrow \mu^+\mu^-$ were used for normalization, there would be all of the systematic errors associated with the measurement of the high energy muon pairs plus all of the systematic errors listed in Section 4.10 for the measurement of the luminosity from untagged electron pairs. Instead, one finds that it is not necessary to understand completely many effects. For example, radiative effects related to the $e^+e^-\gamma$ vertices largely cancel. Plus, for normalization of the muon-pair channel, any final-state radiative effects differ only by small mass-dependent terms. Any errors in the knowledge of the detector acceptance cancel, and the efficiencies of the various noise cuts and tracking cuts need not be well known because they are almost the same for all channels. There is no need to worry about the momentum scale being slightly wrong, either, because the energy spectra for all of the processes behave almost the same and thus would be affected by the same amount. In summary, using a two-photon channel for normalization greatly reduces the error estimate and decreases the likelihood of additional errors from effects not considered.

Of course, not all systematic effects cancel, but those which remain are small and relatively easy to pinpoint and understand. They result from differing

† That is true to the extent that only the multiperipheral diagrams contribute to the QED cross sections. Refer to Section 4.5 for a more complete discussion of this point.

responses to electrons and muons of some parts of the detector. The most important problems involve the shower counters, and hence the trigger. First of all, the latch efficiency depends on the particle type. It has been measured† for electrons and is easy to predict for muons, so the necessary corrections can be made. Second, the geometric acceptance of the trigger is larger for electrons than muons because of the lateral spread of electromagnetic showers. That problem can be avoided by doing the normalization with only those events far from the shower-counter edge and then extrapolating to the full acceptance. Also, there is a small amount of material between the beam-beam interaction point and the drift chambers where the momenta are measured. As a result, electrons can lose a significant amount of energy through bremsstrahlung before being measured, while that is not possible for muons and pions. That effect can be corrected for by use of the EGS Monte Carlo. The only other significant problem is with the different efficiencies for particle identification by the Čerenkov counter. Those are measured from the data and may be corrected for with minimal error. The remainder of this chapter concentrates on understanding these corrections and applying them to obtain the subtracted pion spectrum.

5.1 Rejection of Four-Electron Events

Events with no electrons in the central detector are easily selected by requiring that there be essentially no signal from any Čerenkov counter associated with a track. Since both of the muons or pions are required to pass through the acceptance region of the Čerenkov system, then the rejection of electrons is close to 100% . In fact, a simple calculation using the efficiencies in Table 4.1 quickly shows that the electron background is completely negligible. There is, however, a small loss of efficiency due to random noise in the Čerenkov counters at the one-photoelectron level. Such signals must be rejected as possibly being from electrons if they have time residuals close to zero.

† Refer to Section 4.5 for a discussion of the electron shower counter latch efficiency.

Figure 5.1 shows distributions of the total in-time raw Čerenkov pulse height associated with each track, where *in-time* means those cells with time residuals less than 1.65 ns. The first histogram includes all particles, while the second includes only particles for which the opposing one has been unambiguously identified as a muon or pion.† Such identification is accomplished by accepting only particles which pass through the highly efficient regions of the Čerenkov system with momenta greater than 0.3 GeV and have an associated raw pulse height of less than 0.1 photoelectrons. The noise peak in the pion-muon data overlaps with the electron data, so a cut at 0.2 photoelectrons is chosen such that it is rejected. Figure 5.2 shows distributions of the total out-of-time raw pulse height associated with each track. Note that a single track may have entries in both figures 5.1 and 5.2, so the efficiencies cannot be simply read from the histograms, though they do give a reasonable first estimate. The cut on the out-of-time pulse height is placed above the noise peak at 1.5 photoelectrons.

There are a few "muons" with quite large pulse heights. They are not likely actually to be electrons, but probably are pions passing through Čerenkov cells which have otherwise unseen photon conversions within. In that case they would have to be considered as background events, not as contributions to the identification inefficiency. To do this analysis, all possible cuts‡ have been included to reject background from processes with multiplicities greater than two, except for those which could bias the identification itself. The very low incidence of overlap with photon conversions is evidence in itself of the resulting cleanliness of the data, and, in fact, there are few enough such events that one need not be concerned about them giving a significant error to the measured identification efficiency. With that in mind, the efficiency, as determined from those particles whose partner has been unambiguously identified as a muon or pion, is 99.5% for each track and has no angular or momentum dependence.

---

† There are, of course, also a few kaons and protons, but the distinction is of no relevance here.
‡ The cuts are listed in Section 5.2.

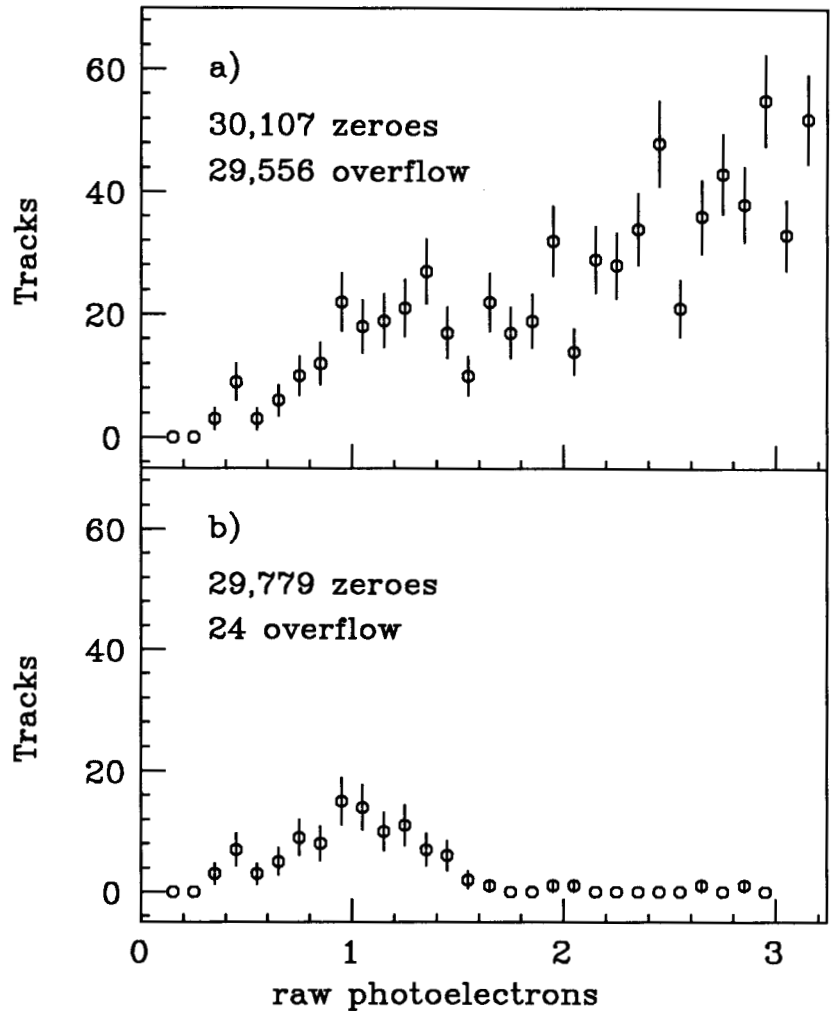

Figure 5.1. The Čerenkov in-time raw pulse height distribution for (*a*) electrons and muons and (*b*) for muons only.

5.2 Analysis Cuts for the Untagged $\pi^+\pi^-$ Signal

The analysis cuts used on the untagged sample of pion and muon pairs are much the same as those used on electron pairs, with the addition of several cuts necessary for reducing background in the hadronic channel. The kinematic cuts are unchanged except that pion, rather than electron, masses are used for computing the two-particle invariant mass. There is only a slight change in the definition of the angular acceptance. Recall that for electrons, the ϕ acceptance is defined by requiring the *measured* tracks to pass through where the shower-counter modules

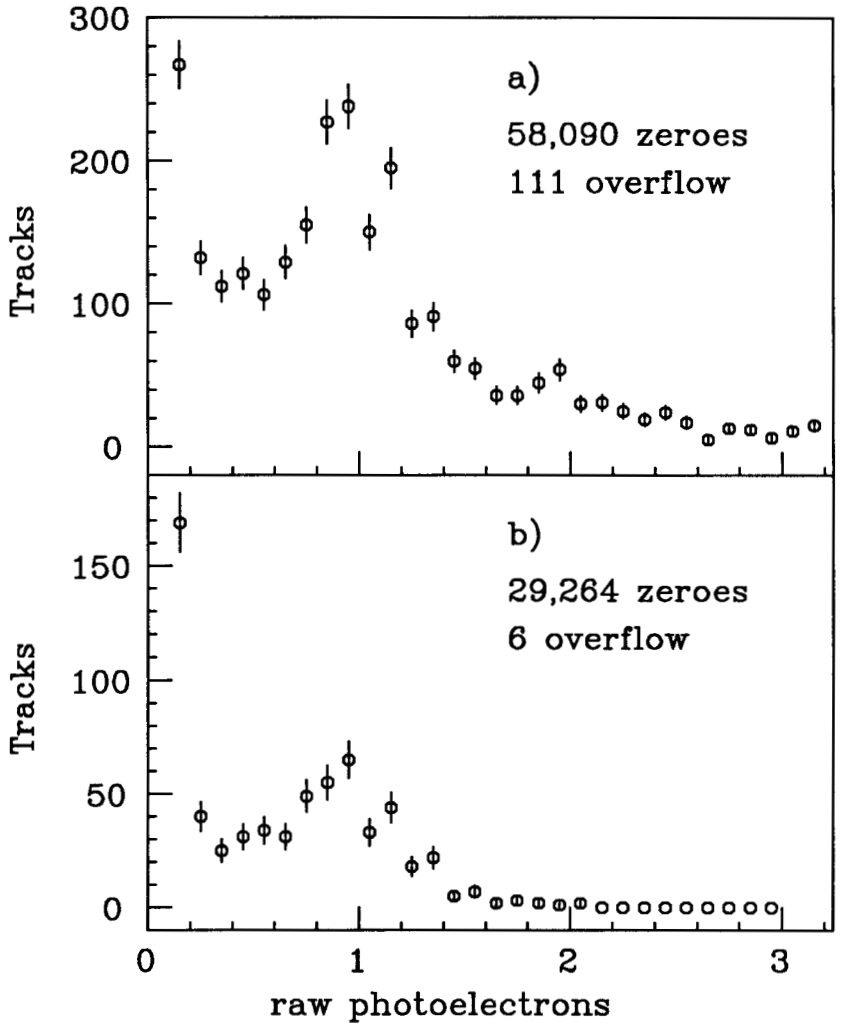

Figure 5.2. The Čerenkov out-of-time raw pulse height distribution for (*a*) electrons and muons and (*b*) for muons only.

are believed to be. However, the trigger for muon and pion pairs already requires that both tracks latch a shower counter, a requirement which is enforced in the analysis by ensuring that no other incidental triggers (from noise, for example) are allowed to contribute events in which one of the tracks has failed to latch a shower counter. An additional cut on the tracking and survey information is not made because it would only confuse the understanding of the pion detection efficiency, due to lack of understanding of the effect of nuclear scattering on the extrapolation of the measured track. This point is discussed further in Chapter 6.

The cuts which are used in the electron analysis for selecting events with well measured tracks are used here without change. However, many of them also serve to reject background processes, none of which are present in the electron-pair sample. All of the remaining cuts serve only to reject background.

The first background to consider comes from cosmic-ray muons. If they happen to pass near the detector center within about 20 ns of the beam crossing, then they can mimic colinear pairs of muons produced by the beams. Simply rejecting pairs which are almost colinear is not a desirable solution because pairs from untagged events already are nearly colinear in the transverse plane, and such a cut would be applied just where the detection acceptance is a maximum. The 0.5 cm impact-parameter cut and the cut on the average z of the tracks near the origin immediately remove a large fraction of the cosmic-ray events present on the data tapes. The rest can be tagged effectively by measuring with the time-of-flight counters and shower counters the time required for the muon to pass from one side of the detector to the other.

The timing information is considered only if the angle between the two tracks is greater than 168.5 degrees. A time-of-flight counter is used on a given side if one is hit and has times at both ends which are consistent within three standard deviations.† Otherwise, a shower counter is used if one is found which passes the same requirements. Only 0.5% of the events considered have no usable timing information; they merely are assumed not to be cosmic rays. Figure 5.3 shows the distribution of the time difference, made before most of the analysis cuts, including vertex cuts, are applied. The separation of cosmic rays from the signal is clear; the cut is chosen to reject all events with a time difference greater than 8.0 ns.

Another background source is scattering of beam electrons on residual gas inside the beam pipe. Such events have a flat distribution of the z position of their origin, while the beam-beam interactions occur within about 3 cm of the detector center. Figure 5.4 shows the distribution of the average z of the track

† Refer to Chapter 9 for a detailed discussion of the time-of-flight analysis.

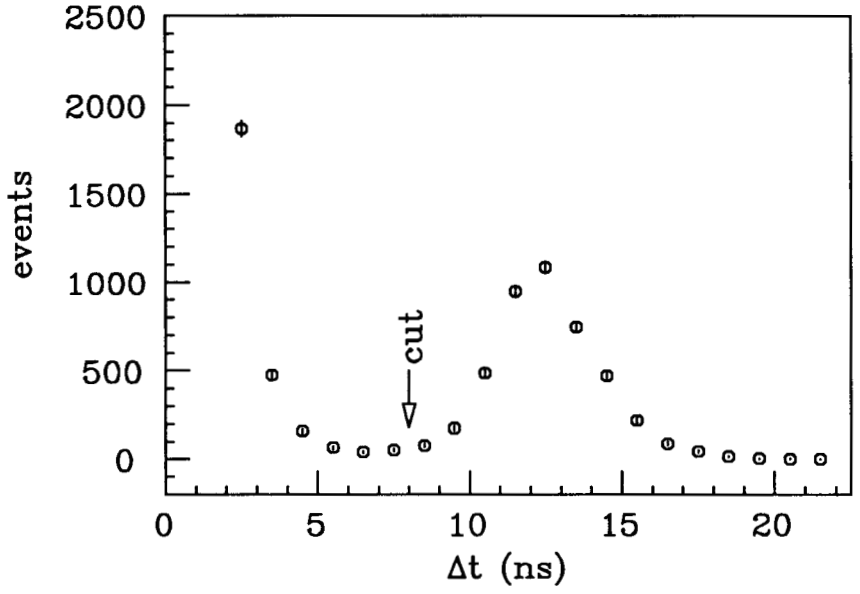

Figure 5.3. Cosmic-ray rejection. Δt is the difference in time of a time-of-flight or shower counter associated with one track and that associated with the second track. The total number of events entered is 58,940. 51912 fall in the bins from zero to two nanoseconds. Events which have an angle between tracks less than 168.5 degrees are entered with a zero time difference.

points closest to the beam line in each event. All other analysis cuts have been made—in particular, cosmic rays have been rejected. A cut rejecting events with $|\bar{z}| > 4.0\,\mathrm{cm}$ eliminates the flat tail without cutting appreciably into the signal. The tail itself gives an upper limit on the contamination from beam-gas scattering in the signal region, because the detection efficiency for tracks a few centimeters outside of that region is approximately what it is within.

The remaining background is from genuine beam related events, either by $\gamma\gamma$ production or e^+e^- annihilation. Many hadronic final states can mimic a pair of pions if all other particles in the final state escape detection. The analysis must rely on the cut on $k_\perp$ to reduce such background to a low level. The tracking resolution does not allow a cut on $k_\perp$ any tighter than what has been used for the electron analysis without causing an unacceptable loss of the signal. Therefore, some background remains, and its level must be estimated.

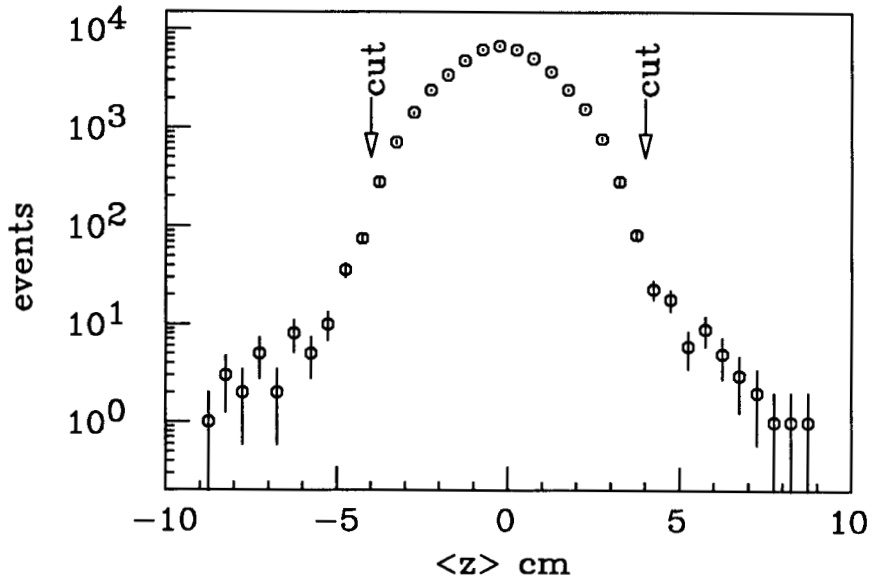

Figure 5.4. The z position of the interaction point. It is calculated by averaging the z coordinates of the points of closest approach of the tracks to the beam-line. Only events with two non-electron tracks which have passed all of the $\pi^+\pi^-$ analysis cuts, except for the cut on $\bar{z}$, are used.

It is important that if any extra particles are detected by any means that the event be rejected. Therefore, cuts are made on the pulse heights of shower counters and Čerenkov counters which are not associated with either of the two tracks. The total pulse height of the pole-tip counters must be less that 0.1 GeV, and the pulse height of the barrel shower counters, summed over all counters not hit by a track and not adjacent to one hit by a track, must be less that 0.15 GeV. Any event with a Čerenkov counter which has a time residual less than 1.65 ns and a raw pulse height greater than 3.0 photoelectrons is rejected. Finally, a search is made for track stubs in the planar drift chambers. If a stub is found with at least one stereo wire, two axial wires, and four total wires and has a χ^2 per degree of freedom less than 4.0 from fitting a straight line to the hits, then the event is rejected, unless the stub is found to be sharing wires with one of the two tracks or using any wires adjacent to one used by a track.

These noise cuts are designed primarily to detect photons, which may leave a signal in a shower counter or convert in material in the Čerenkov counters or planar drift chambers. They also serve to reject events in which a charged particle has been missed by the tracking system but still hits a shower counter. The cut values have been tuned and tested by looking at single-event displays as well as histograms. Their effect on the actual signal can be checked by applying the same cuts, except for cuts on Čerenkov pulse height, to electron pairs, since there is no significant background to the four-electron channel. After all other analysis cuts have been made, the noise cuts reduce the e^+e^- sample by only 1.2%.

The analysis commences with summary tapes including two-track events with no cuts on particle type, since the electron-pairs must also be present to provide the normalization. A total of 398,936 events are input, and the trigger requirement eliminates 2,969. Before separating the particle types, most of the other cuts are made. Those cuts and their effects are listed in Table 5.1. Of the 138,590 remaining events, 61,798 are positively identified as electron pairs and 75,094 as pairs of non-electrons. The 1698 events which fail the cuts for both categories are rejected.

Considering now only the category of non-electron events, the requirement that each track at least pass near to a shower counter rejects 1180 events. The cuts on planar drift chamber stubs and barrel-shower and Čerenkov noise reject 1413 events, and requiring both tracks to latch a shower counter rejects 1670 events. The latter cut is made in order to ensure that both tracks are within the barrel-shower acceptance and that the trigger for the event is not from some random source. That is necessary if the acceptance and the trigger response are to be understood. Finally, 72 events are rejected because the two tracks are of the same charge. The result is a sample of 70,759 events, including muon and pion pairs with a small fraction of background from kaon and proton pair production and other hadronic processes. To produce the pion-pair spectra, the corresponding muon-pair spectra must be calculated and subtracted, and the level of the other backgrounds must be estimated.

Table 5.1. List of some of the cuts for the $\pi^+\pi^-$ analysis. The remainder are listed in the text. The fourth and fifth columns give respectively how many events would be rejected by the cut before all other cuts and how many would be rejected after all others.

Quantity	Lower limit	Upper limit	Failures when first	Failures when last	Failures in order
poletip E	0	0.1 GeV	18389	3112	18389
inner DC hits	12	16	21938	3779	18892
fit errors	0	0	3537	92	822
$\overline{z}$	−4.0 cm	4.0 cm	6149	427	2996
impact parameter	0	0.5 cm	24786	1370	11327
$\cos\theta$	−0.6	0.6	74593	33699	62128
$W_{\pi\pi}$	0.6 GeV	2.0 GeV	156867	24206	114480
$k_\perp/W_{\pi\pi}$	0	0.2	96288	27134	27140
$k_\perp$	0	0.3 GeV	23080	241	250
$\mathrm{MAX}(p_t^1, p_t^2)$	0.25 GeV	∞	85606	782	783
cosmic	0	0	4626	170	170

5.3 Subtraction of the $\mu^+\mu^-$ Background

Once the proper normalization has been determined, it is straightforward to calculate how many muons are present in each bin of any distribution. QED is used to calculate the physical distributions, by means of the Vermaseren Monte Carlo, or in the untagged case, equally well by the EPA Monte Carlo.† We continue here with the untagged sample, but the methods also apply to the tagged sample.

† For the case of muon-pair production, as well as the four-electron final state, the EPA program has been checked to give results identical to those of the Vermaseren program when an untagged analysis is made.

Detector effects are especially simple to simulate for muons. The identification efficiency has no kinematic dependence within the fiducial volume, and the shower counter latch efficiency is affected only by electromagnetic range-out. The amount of material traversed by muons going in various directions does not vary greatly, and range fluctuations are small (they actually are neglected in the Monte Carlo), so the result of the electromagnetic effects is simply a rather sharp cutoff where the efficiency drops to zero below a particular value of the initial momentum. This cutoff can be predicted by using the full simulation of the detector, including the program for detailed simulation of the shower counter geometry and materials.

To check the program, the calculation is made for a combination of tagged Monte Carlo muon pairs and pion pairs in approximately the proportion found in the data. Only tracks which pass through a counter well away from the edge are used, so the histogram shows the probability of the particle actually stopping in the material before the second layer of scintillator. Tagged events are used because their LS trigger, which requires a coincidence of a luminosity counter and a barrel shower counter, allows events to be seen in which one particle fails to latch the shower counter. Therefore, the Monte Carlo can be compared directly with the data as long as the trigger is simulated. Figure 5.5 shows that the sharp edge seen in the Monte Carlo agrees well with that seen in the data, although, as expected, the data show an additional and more slowly varying inefficiency due to nuclear interactions of pions.

Electron pairs are used to provide the normalization, but care must be exercised to correct for differences in acceptance of the trigger for electrons and muons. It is of no help simply to require the same trigger for the two types, because the 2S trigger has a dramatically different response for electrons as compared to muons. Instead, electron events with only a KS trigger still are accepted, and the inefficiency caused by ranging out of electromagnetic showers is corrected for by using the measurements of Chapter 4. Likewise, the effect of range-out on the muons is corrected for by using the curve in Fig. 5.5. There is the additional

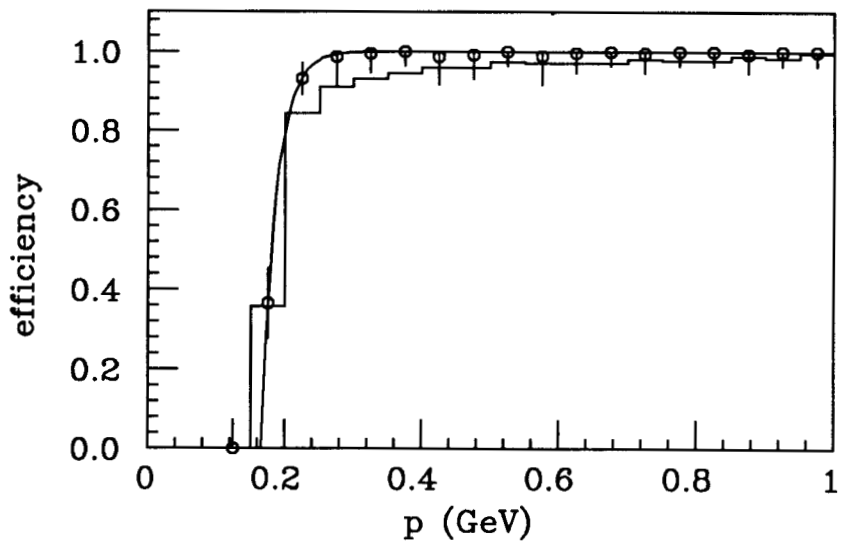

Figure 5.5. The Monte Carlo shower counter latch efficiency for a mixture of tagged pion and muon pairs (points) is compared with that measured from tagged data (solid histogram). The Monte Carlo does not include nuclear interactions. The smooth curve represents Eqn. 4.2 with the parameters $A = 1$, $p_0 = 0.177$, and $\tau = 0.0219$.

problem of edge effects, however. Electrons have a larger acceptance in the shower counters than do muons, because showers in the aluminum surrounding the counters can spread into the scintillator. To some extent, that is simulated by EGS, but it is best not to rely on a complicated Monte Carlo calculation. It also is not a good idea to try to use the tracking information to specify when a particle is within the shower counter edge, because of inherent tracking and survey errors. The approach that is taken is to define a muon or pion as being within the acceptance if it latches a shower counter. That means that the few events must be discarded which rely on triggers from some source besides the two shower counters actually hit by the muons or pions. Electron pairs, on the other hand, are kept only if both tracks are determined by tracking to pass through a shower counter at least 4 cm from the edge. That gives a large enough margin for error that the survey and tracking errors do not affect the acceptance (see Fig. 5.6). The only remaining problem is to determine the difference in geometric acceptance for muon

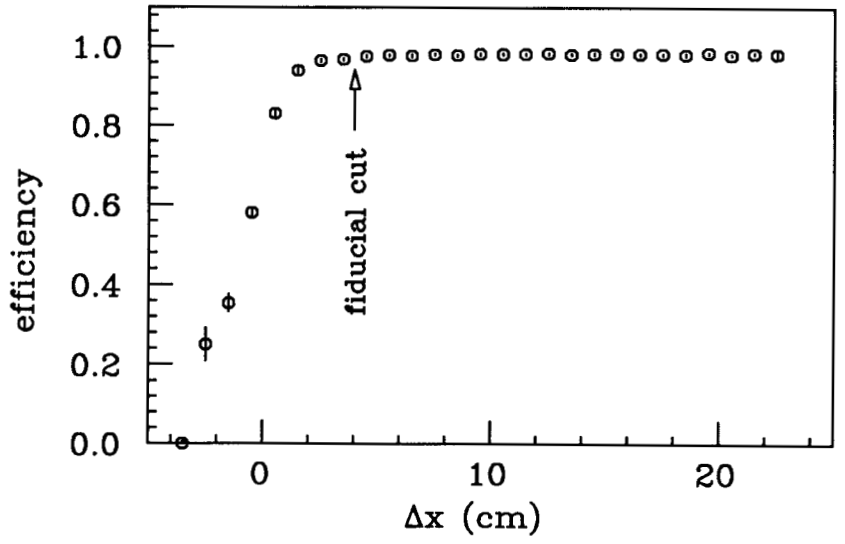

Figure 5.6. The resolution of the shower-counter edge for electrons. The efficiency for the first layer of the shower counter to latch is plotted as a function of the distance from the nearest edge of the counter.

pairs between the case where the 4-cm cut is made as for the electron pairs and the case where only two latches are required. After making all of the analysis cuts, the muon-pair Monte Carlo with full detector simulation gives an acceptance ratio of 1.469±0.020, while the non-electron data gives 1.450±0.007. The fact that the two agree shows that the width of the counters is correct in the Monte Carlo and that there is not much of an edge effect from pion-nucleus interactions; the more precise value is used for the analysis. Note that the corresponding ratio for electron pairs is found to be 1.493 ± 0.010. Thus the edge effect from electromagnetic showers could cause as much as a 3% increase in acceptance.

Of the 61,798 electron pairs, 6455 are rejected because one track does not have an associated shower counter. The cuts on planar drift chamber stubs and barrel-shower and Čerenkov counter noise reject 678 events, and 20,366 are rejected in order to satisfy the 4-cm fiducial cut in the shower counters for each track. Of the remaining events, 14 have two electrons of the same charge and are rejected. Since the final $\pi^+\pi^-$ invariant-mass spectrum must be calculated by assuming pion masses for both particles, then the cuts should be made for all particle types

by assuming pion masses. However, the cut of $W_{\pi\pi} \geq 0.6\,\mathrm{GeV}$ is lower than the invariant-mass cut made in the analysis of Chapter 4. For that reason, the region between $W_{\pi\pi} = 0.6\,\mathrm{GeV}$ and $W_{\pi\pi} = 0.7\,\mathrm{GeV}$ cannot reliably be corrected for systematic effects. Only the 23,645 events in the range from 0.7 GeV to 2.0 GeV are used for normalization.

To proceed, the same number of Monte Carlo events are generated, and all detector effects are included as in Chapter 4, including the trigger and identification efficiencies. One finds that the data represent an effective luminosity of $64.07 \pm 0.42\,\mathrm{pb}^{-1}$. It is not the true beam luminosity because not all inefficiencies of the detector have been included in the calculation. In particular, many with only a ϕ dependence are neglected. Effects which differ between electrons and muons, such as the electron identification efficiency and the electron shower counter latch efficiency, have been included. The one exception is the effect of the beam-pipe and drift-chamber material.

We have seen that the material in the shower counters and in front of them affects the normalization by reducing the trigger efficiency for electrons relative to muons. In that regard, the material in the beam pipe and the inner drift chambers is insignificant. However, the innermost material that the particles must pass through is unique in that it affects the particles before their momenta are measured. There are two layers of aluminum which are important in this respect: The first is the material of the beam pipe and the inner wall of the innermost drift chamber, comprising 0.029 radiation lengths for *1982/1983* data and 0.013 radiation lengths for *1984* data, and the second is the material between the two inner drift chambers, comprising 0.0054 radiation lengths. The material between the inner and outer drift chambers is not relevant because the outer drift chambers play little part in the momentum measurement for low-momentum tracks.

Electromagnetic interactions of electrons in the aluminum cause several losses in addition to those incurred by muons. In about 0.3% (in *1984*) to 0.6% (in *1982/1983*) of the events, extra electron tracks are produced with high enough

momentum to be found by pattern recognition. Energy loss from bremsstrahlung causes several other effects. The impact parameter distribution is broadened slightly, as is the distribution of $k_\perp$, resulting in the loss of an additional couple of percent of the events. But by far the biggest effect is simply due to a slight shift in the energy scale caused by the average energy loss incurred by electrons before reaching the region where their momenta are measured. Of all of the cuts made, most are placed well out in the tails of distributions and hence are not very sensitive to any effects. The exceptions are the cuts defining the angular acceptance, which are not affected by the energy loss, and the cut on invariant mass, which is very sensitive to any shift in the energy scale.

The EGS Monte Carlo is used to determine the effect of the material on electrons. Figure 4.21 shows the fractional energy loss of electrons in the first layer of aluminum for the 1983 data. The average loss is 3.3%, and 7% of the electrons lose greater than 10% of their energy. Since the invariant-mass spectrum falls as $1/W^3$, a downward shift by $x\%$ in the energy scale will decrease by $2x\%$ the number of events above any given cut, so one can see that the bremsstrahlung must have a drastic effect on the normalization.

The bremsstrahlung is found not to affect noticeably the shape of the invariant-mass distribution, so all that is necessary is to calculate a constant correction factor for each of the data sets. That is done by taking the ratio of the efficiency found from the Monte Carlo with full detector simulation, including EGS where necessary, for muon pairs with respect to electron pairs. The results are 0.889 ± 0.008 for *1982/1983* data and 0.946 ± 0.009 for the *1984* data, or 0.908 ± 0.008 overall.

There also is some unknown systematic error from the EGS calculation. EGS, along with the rest of the detector simulation software, does predict correctly the number of extra tracks produced by electromagnetic interactions, which is $0.7 \pm 0.2\%$ in the *1982/1983* data. It also has been shown to predict correctly the latch efficiency in the shower counters, but of these two checks, the first

is not very significant statistically and the second is not directly related to the beampipe. However, EGS has generally been found to be reliable, and calculating the energy loss of an electron passing through a thin sheet of aluminum is a relatively simple application of the program. Therefore, it is reasonable to assume that it gets the correction right to at least 15%, and since the correction itself is about 10%, then the resulting error in the normalization is about 1.5%. Including this correction, along with systematic errors from the trigger and electron-identification corrections and the statistical error from the sample of four-electron events, results in a corrected effective luminosity for the four-electron sample of $\mathcal{L}_{\text{eff.}}^{e^+e^-} = \varepsilon_e \mathcal{L} = 70.5 \pm 1.6\,\text{pb}^{-1}$. Here, ε_e represents the part of the detection efficiency, such as gaps in ϕ, which are not included in the Monte Carlo calculation.

The analysis of muon pairs does not require the 4-cm fiducial cut, so including the corresponding correction factor leads to $\varepsilon_\mu = \varepsilon_\pi = 1.450 \cdot \varepsilon_e$ and an effective luminosity for the non-electron sample of

$$\mathcal{L}_{\text{eff.}}^{\pi^+\pi^-} = \mathcal{L}_{\text{eff.}}^{\mu^+\mu^-} = \varepsilon_\mu \mathcal{L} = 102.3 \pm 2.3\,\text{pb}^{-1}\,. \tag{5.1}$$

The quoted error is the sum, in quadrature, of the errors listed in Table 5.2.

Another conceivable source of error is from radiative corrections to the leading-order QED graphs. One may suspect that the corrections could be different for the $e^+e^-\mu^+\mu^-$ final state compared with the $e^+e^-e^+e^-$ final state. It has been shown that the only significant contribution for either final state in leading order is from the two multiperipheral graphs, so we need only consider corrections to those two graphs. Therefore, the only difference in the calculations for the two final states comes from the muon-electron mass difference. The matrix elements are otherwise exactly the same. Now, the part that the mass plays in the result depends on kinematics; at high enough energy it should have very little effect. In fact, for the leading order cross sections, in the energy range and geometric

Table 5.2. Sources of error in the normalization derived from the electron-pair sample.

Source of Error	Percent Error
trigger efficiency	± 0.8 (syst.)
electron identification	± 0.5 (syst.)
pre-tracking radiator	± 0.9 (stat.) ± 1.5 (syst.)
barrel shower counter acceptance correction	± 0.5 (stat.)
size of e^+e^- sample	± 0.7 (stat.)
Monte Carlo	± 0.5 (stat.)

acceptance considered in this analysis, the difference of the two cross sections is only 3.7%. Since the mass effect is so small for the leading order, and since the overall radiative corrections are known to be only of the order of 1%,† then it is reasonable to expect that the difference of the radiative effects for the two processes is much less that a percent and can be neglected.

Monte Carlo muon-pair events are analyzed just as electron pairs are, except that the effect of the Čerenkov identification is simply an overall loss of 1% of the events, and the shower counter latch efficiency is given by Fig. 5.5. The effective luminosity of Eqn. 5.1 yields 49,775 Monte Carlo muon pairs within the analysis cuts. Subtracting those from the data sample of muons and pions leaves a total of 20,984 pion pairs, with some remaining background, as seen in Fig. 5.7. The prominent peak around 1.2 GeV is due to the f (1270), and one can see that there also is a significant number of pion pairs produced in the continuum. In Chapter 8 this spectrum is fit to the theoretical model developed in Chapter 7.

† Refer to Section 4.10 for more discussion of the radiative corrections.

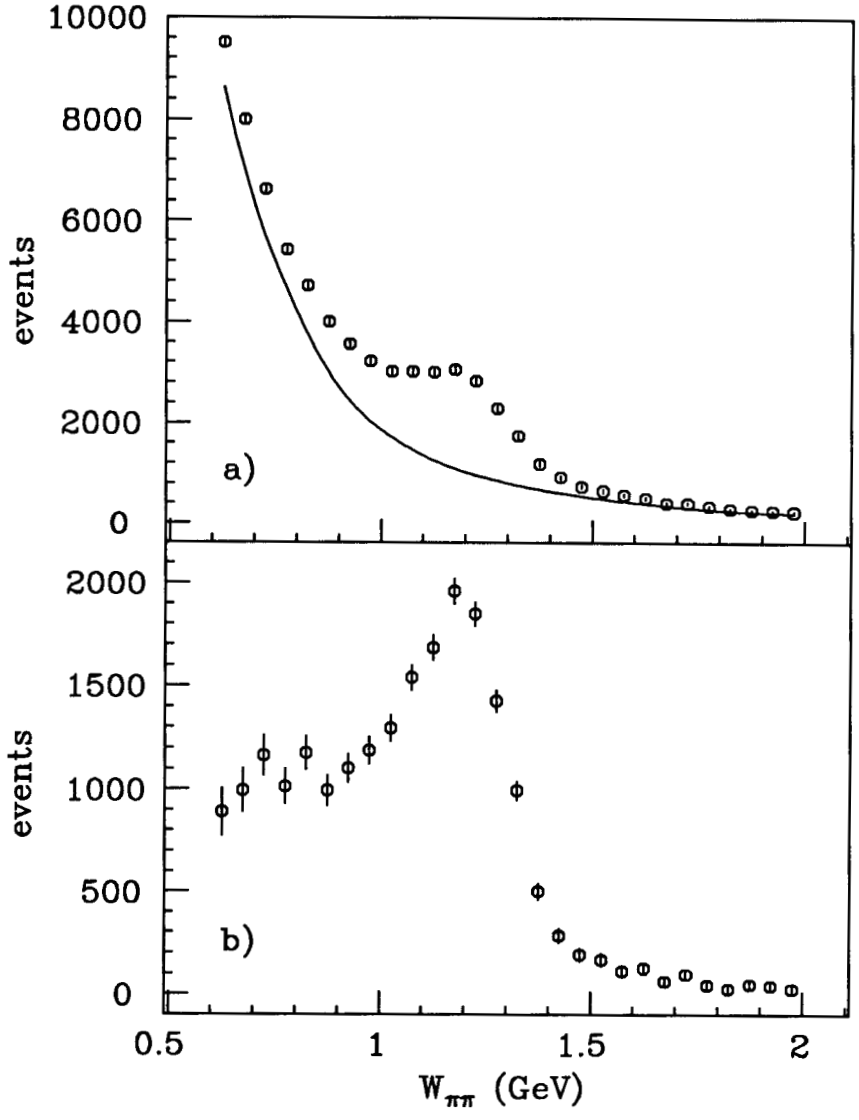

Figure 5.7. The pion-pair and muon-pair invariant mass. (*a*) The data sample of pairs of non-electrons is represented by the points, while the smooth curve shows the predicted muon-pair spectrum. (*b*) The pion-pair spectrum which results after subtracting the muon-pair prediction.

5.4 Consideration of Other Backgrounds to $\gamma\gamma \to \pi^+\pi^-$

Muon pairs are by far the largest background to the selection of pion pairs, but their are a few other minor sources of background which must be considered. First let us consider cosmic-ray muons. Most of them have been removed by cuts on the timing, but due to the resolution of the time-of-flight counters, there is a

small tail toward short times which contributes some background. An upper limit on such background is estimated by roughly extrapolating the lower edge of the cosmic-ray peak below the cut at 8.0 ns. For that purpose, Fig. 5.3 is not useful because it shows the time distribution as it is before other cuts have been made, of which many preferentially reject cosmic rays. To study the background, the same histogram is reproduced, but the data are entered only after making all analysis cuts not related to the timing. The result shows that only 0.31% of the events have times above the 8.0 ns cut, and an upper limit on the cosmic-ray background not removed by the time cut is 15 events. That is an insignificant background, even when considering the distribution of $\widetilde{\beta}$, where all the cosmic rays fall in the one bin about $\widetilde{\beta} = 0$.

Next, we consider the background from beam-gas scattering. It should be characterized by a roughly uniform distribution of the z-position of the interaction. Figure 5.4 shows a histogram of the z-position of the estimated interaction point for events passing all analysis cuts except for the z cut. Note the long, low tails outside the cut at $\pm 4.0\,\mathrm{cm}$. They are partly due to tails in the distribution of the colliding beams and tails in the tracking resolution, but they can be used to give an upper limit on the beam-gas contribution. It is reasonable to assume no more than five events per bin coming from beam-gas scattering, which is a background of no more than 0.6% of the pion pairs.

The background from $e^+e^- \to$ hadrons is estimated by use of the Lund string-model Monte Carlo,[38] with radiative corrections included for the QED vertices.[33] The cutoff energies for photons radiated from the incoming beams are set from $0.8561E_b$ to $0.9801E_b$, depending on the quark flavor produced, and the total cross section is $1.276 \cdot 3 \cdot \frac{11}{9} \cdot \sigma_{e^+e^- \to \mu^+\mu^-} = 0.4817\,\mathrm{nb}$. Of 46,378 events generated and simulated in the detector, only three pass all of the analysis cuts for $\gamma\gamma \to \pi^+\pi^-$. When normalized to the integrated luminosity of the data, that means that the background from this source is only about five events total, which is negligible.

For the same reason that Bhabha scattering does not contaminate the

electron-pair sample, the process $e^+e^- \rightarrow \mu^+\mu^-$ does not contaminate the pion-pair sample. The contamination from tau-pairs is estimated in the same way as for the electron-pair analysis, and it is found to be at only the level of eight events. Again, such a level of contamination is small enough just to ignore.

Probably a larger source of contamination than $e^+e^- \rightarrow$ hadrons is inclusive hadron production, not including exclusive pion pairs, from $\gamma\gamma$ interactions. The $\gamma\gamma$ interactions produce events of low energy and multiplicity, so such events can more easily mimic pion pairs. Unfortunately, there is no simple model which can be used to estimate the background, and the cross section for $\gamma\gamma \rightarrow$ hadrons is not even known in detail empirically. However, one can estimate the background from the combination of all processes which produce at least four charged pions (plus beam-gas scattering) by observing the number of like-sign pion pairs in the data sample after all cuts other than the charge cut have been made. There are 70 such events, so one might expect approximately 70 more from the same source, but with a pair of oppositely charged pions detected. However, there are an estimated 116 beam-gas events in the data sample, which tend to have non-zero charge and might alone account for the 70 like-sign events. In fact, there are more events with charge $+2$ than -2, as one would expect from beam-gas collisions. On the other hand, we have not yet accounted for background events with two charged pions and several neutral pions. There should be fewer of them than events with several charged pions, so it is reasonable to set an upper limit on the total background, including beam-gas events and $\gamma\gamma \rightarrow$ hadrons, of 150 ± 50 events, which is only 0.7% of the sample of pion pairs.

Not yet accounted for are two specific backgrounds, both of which can be accurately estimated and subtracted. The first is resonance production from two photons, where the resonance decays into two pions plus one-or-more photons. The only such resonance which can in that way contaminate the pion-pair data is the η'. In particular, the decay mode $\eta' \rightarrow \rho^0\gamma$ often produces two pions which pass all of the cuts, and the photon usually is of too low energy to be detected, or

else it escapes through cracks in the detector.

The background from η' production is estimated by Monte Carlo, using as input the measurements of $\gamma\gamma \to \eta'$ by the PLUTO collaboration.[39] The η' state is generated as a Breit-Wigner resonance according to

$$\sigma_{\gamma\gamma\to\eta'} = \frac{8\pi W_{\gamma\gamma}}{m_{\eta'}} \cdot \frac{\Gamma_{\gamma\gamma}\Gamma_{\eta'}}{(W_{\gamma\gamma} - m_{\eta'}^2)^2 - \Gamma_{\eta'}^2 m_{\eta'}^2}, \tag{5.2}$$

with $m_{\eta'} = 0.957\,\mathrm{GeV}$, $\Gamma_{\gamma\gamma} = 3.80 \pm 0.26 \pm 0.43\,\mathrm{keV}$, and $\Gamma_{\eta'} = 200 \pm 34\,\mathrm{keV}$. When it is allowed to decay through any of its possible modes by using the decay programs of the Lund Monte Carlo,[38] then one finds that only the $\rho^0\gamma$ channel contributes any background.

The Lund programs do not take into account the large width of the ρ^0 or its polarization, so it is necessary to study that channel in more detail. The ρ^0 has such a large width that a completely accurate description of the η' decay should properly include the three-body phase space. An adequate approximation for this purpose is instead to model the decay as a two-step process. After selecting the ρ^0 mass according to a Breit-Wigner distribution, the ρ^0 and γ are produced in a uniform two-body phase space. The Breit-Wigner simply is cut off at the η' mass, which is another simplifying assumption, but is not a large effect. The ρ^0, which must, like the γ, have helicity ± 1, then is decayed into two pions with a center-of-mass angular distribution of $\sin^2\vartheta$.

Of 6251 such events generated, corresponding to an integrated luminosity of $89\,\mathrm{pb}^{-1}$, a total of 340 pass all of the analysis cuts for pion pairs, giving the mass spectrum shown in Fig. 5.8. The reason that the peak is not centered about the ρ^0 mass is because the efficiency for such events is rising sharply in that energy range. Including the uncertainties of the PLUTO measurement, of the measurement of the pion efficiency, and of the DELCO luminosity ($122.5 \pm 4.5\,\mathrm{pb}^{-1}$), gives a total of 468 ± 87 events to be subtracted from the measured $\pi^+\pi^-$ spectrum.

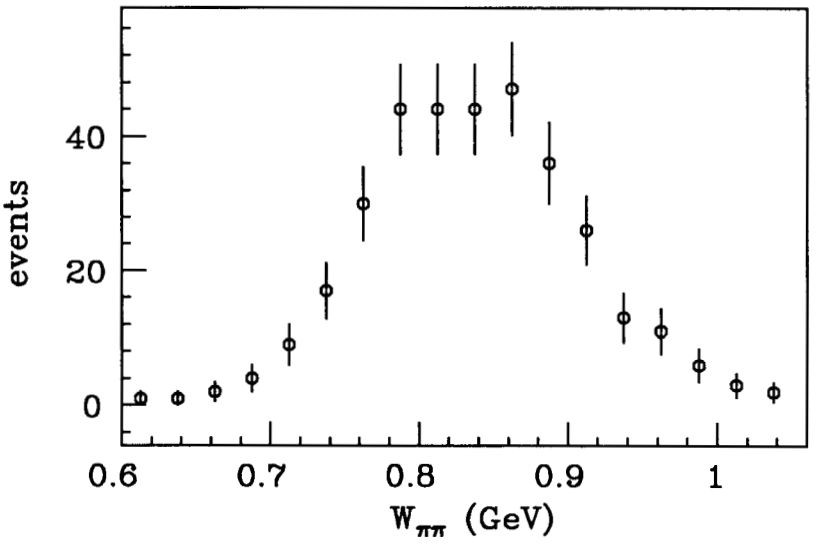

Figure 5.8. The $\eta' \to \rho^0\gamma$ background $\pi^+\pi^-$ mass spectrum corresponding to an integrated luminosity of $86\,\mathrm{pb}^{-1}$.

The last background to consider is that due to the processes $\gamma\gamma \to K^+K^-$ and $\gamma\gamma \to p\bar{p}$. Such events often can be identified by time-of-flight measurements. However, only a fraction of the events in the data have usable timing information for each track. The approach used here is to consider only those events which do have good timing information available for both tracks and measure the fraction of kaon pairs plus proton pairs for each mass bin.† The number found of pairs of heavy particles is corrected for background and inefficiency induced by the timing cuts, and the result is scaled for each bin, by the ratio of the number of all pairs to the number with good timing, to give the background of the whole data set. Figure 5.9 shows the final result for the K^+K^-, $p\bar{p}$ background. Both it and the η' background are subtracted from the data in Chapter 8 when fitting the spectrum to theoretical models. However, these backgrounds are small enough that the change in the spectrum from what is seen in Fig. 5.7*b* is hardly visible.

† Refer to Chapter 9 for a complete discussion of the time-of-flight analysis procedures.

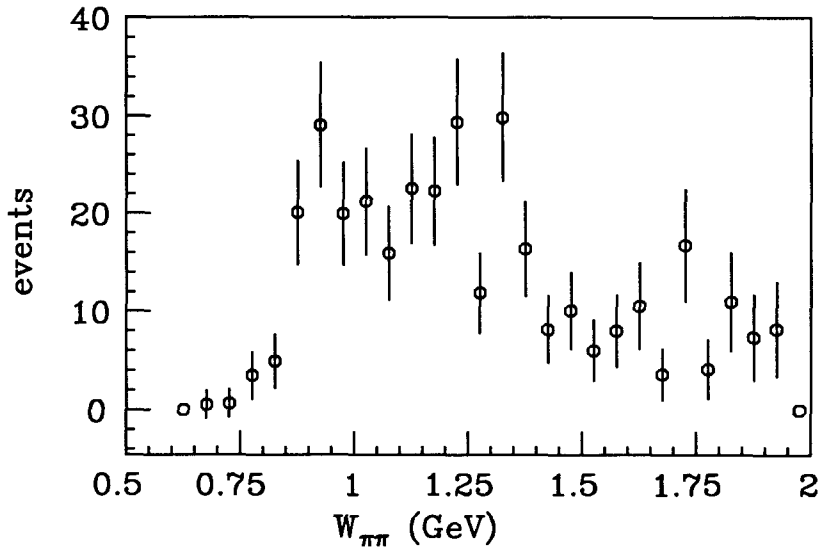

Figure 5.9. The K^+K^- plus $p\bar{p}$ background to the $\gamma\gamma \rightarrow \pi^+\pi^-$ measurement, as measured from the data and corrected for the time-of-flight acceptance and efficiency.

5.5 The Tagged Pion-Pair Spectrum

The tagged analysis proceeds much the same as the untagged, and the analysis of the luminosity counter tags is done exactly the same as for the four-electron channel. The cuts are the same as for the untagged analysis, except for the cut on the luminosity counter energy and the cuts on the total transverse momentum $k_\perp$ of the two tracks observed in the central detector. Because a strict cut on $k_\perp$ cannot be made, the rejection of background is a more serious problem than for the untagged analysis. Therefore, the cuts on noise in various counters and in the outer drift chambers become more important. They reduce the final sample of non-electron pairs by 5.5%. Using the fact that 2.0% of the final sample of electron pairs is eliminated by the same cuts and assuming the same effect on muon pairs, we estimate that the cuts reduce the sample of pion pairs by about 15%.

An attempt is made to use the measurement of $k_\perp$ to reduce the background a little further. Assuming that only one of the beam electrons scatters at a large angle, then the transverse momentum of the tagged electron should balance that of the two particles observed in the central detector. Unfortunately, the luminosity

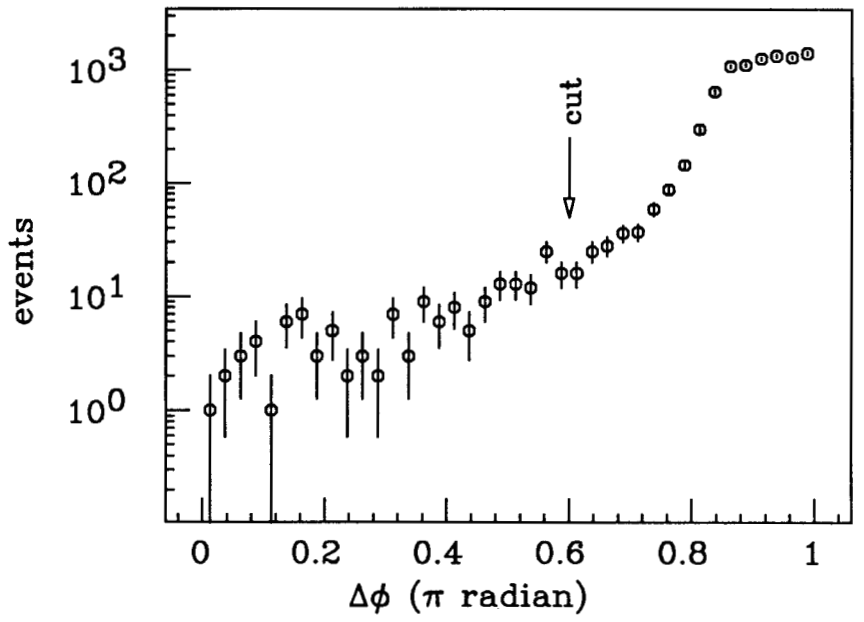

Figure 5.10. Transverse momentum cut for tagged data. $\Delta\phi$ is the angle in the transverse plane between the direction of the sum of the momenta of the two electron tracks and the direction of the center of the hit luminosity counter.

counters do not give a good measurement of the transverse momentum. They tell only whether it is larger than about 0.3 GeV and what the azimuthal angle is within ± 60 degrees. Therefore, the only cuts made are to require that the measured $k_\perp$ be larger than 0.1 GeV and that the angle $\Delta\phi$, between the vector $\vec{p}_t^{\,1} + \vec{p}_t^{\,2}$ measured in the central detector and the ϕ direction of the center of the hit luminosity counter, be larger than 0.6π radians. Figure 5.10 shows a histogram of $\Delta\phi$ for tagged electron pairs, made before any of the noise cuts. Only 1.8% of those events are eliminated by the cut, while it eliminates 3.7% of the tagged non-electron pairs. Thus it is evident that even such a loose cut helps substantially to reduce the background.

Because of the requirement of a high energy tag in the luminosity counters, backgrounds from all sources other than two-photon scattering are greatly reduced. For example, when the time difference from one side of the detector to the other is plotted before other cuts are made, only 5 of the 989 events with an angle

between tracks greater than 168.5 degrees have $\Delta t > 8.0\,\mathrm{ns}$. Thus the cosmic ray background is negligible, and likewise the beam-gas and $e^+e^- \rightarrow$ hadrons backgrounds are negligible. The remaining background, except for that from η' production and charged kaon and proton pairs, is estimated from the number of events found with non-zero charge. There are 227 such events after all other cuts have been made, compared with only four electron pairs of non-zero charge. There should be an equal number of zero-charged events from the same background source, and there could be as much as about half that many again of events from the same background but with extra neutral, rather than charged, pions. The charged background is relatively certain, while we can only guess at the number of neutral pions which may have escaped detection. Hence the background from multi-hadron production is estimated to be 560 ± 112 events.

The backgrounds from η' production and from charged kaon and proton pairs are determined in the same way as for the untagged analysis. In this case, the number of proton and kaon pairs (45 total) is completely insignificant compared with the statistical precision of the pion-pair sample, amounting to no more than four events in any single bin. The calculation of η' production assumes a ρ^0-pole form factor, $1/(1-q^2/m_\rho^2)$, which has been found by the PLUTO collaboration to give an adequate description of their data.[39] The number of η' yielding pion pairs to be subtracted from data is only 72 ± 16.

In order to obtain the normalization for subtracting muon pairs, the tagged electron pairs are analyzed within the trigger acceptance defined by the fiducial cut 4 cm from the shower counter edges. The number found in the range $0.7 < W_{\pi\pi} < 2.0\,\mathrm{GeV}$ is 3719 events. Again, a correction must be made for bremsstrahlung energy loss in the beampipe and drift chamber material. Using again the full simulation of the detector, including the EGS Monte Carlo, the loss of electron pairs relative to muon pairs is 0.931 ± 0.016 for the *1982/1983* data, 0.966 ± 0.017 for the *1984* data, and 0.943 ± 0.016 overall. The effect is less for the tagged analysis than for the untagged partly because for the former there is no cut

on $k_\perp$. In general the two differ kinematically, so some difference must be expected in any case. Comparing the data with a calculation from the Vermaseren Monte Carlo and applying the correction gives an effective luminosity of $62.7 \pm 1.6\,\mathrm{pb}^{-1}$.

For tagged non-electron pairs, the 2S trigger is redundant to the LS trigger, which requires only one shower counter in coincidence with the luminosity counter. Therefore, there are some events in which only one pion or muon has hit and fired a shower counter. But both particles still are required to fall within the shower counter acceptance. In cases where one of the particles does not latch a shower counter, the tracking information is used for that particle to determine whether it is within the acceptance. When the acceptance is so defined, there is an increase of the number of non-electron pairs by a factor of 1.501 ± 0.024 over the number found within an acceptance defined by the 4-cm fiducial cut. Including that correction results in an effective luminosity for the tagged non-electron sample of

$$\mathcal{L}_{\mathrm{eff.}}^{\mathrm{tag}} = 94.1 \pm 3.3\,\mathrm{pb}^{-1}\,, \tag{5.3}$$

where the quoted error is the sum, in quadrature, of the errors listed in Table 5.3.

Table 5.3. Sources of error in the normalization derived from the tagged electron-pair sample.

Source of Error	Percent Error
trigger efficiency	$\pm$ 0.8 (syst.)
electron identification	$\pm$ 0.5 (syst.)
pre-tracking radiator	$\pm$ 1.7 (stat.) $\pm$ 1.5 (syst.)
barrel shower counter acceptance correction	$\pm$ 1.6 (stat.)
size of e^+e^- sample	$\pm$ 1.6 (stat.)
Monte Carlo	$\pm$ 0.9 (stat.)

From the data, a total of 9366 tagged non-electron pairs pass all of the cuts. The invariant-mass spectrum for those events, calculated with an assumption of pion masses, is displayed in Fig. 5.11*a*. Using the luminosity of Eqn. 5.3, the muon-pair spectrum is produced as for the untagged analysis, except that in this case it is essential to use the Vermaseren Monte Carlo generator. The calculation yields 6654 muon pairs, and subtracting those leaves 2712 pion pairs. Subtracting the estimates of the other backgrounds leaves the 2034 events for which the $\pi^+\pi^-$ invariant-mass spectrum is displayed in Fig. 5.11*b*.

As in the $\pi^+\pi^-$ mass spectrum from untagged events, a peak near the f is prominent, and there also is a large amount of continuum production. As far as data analysis is concerned, what remains to be done is to measure also the angular distribution for pions pairs and to correct the observed distributions for resolution and efficiency effects. Then, to finish the measurement, a model must be constructed which includes both continuum and resonance production, and it must be fit to the data. But first, let us finish the analysis necessary for determining the detection efficiency for pion pairs.

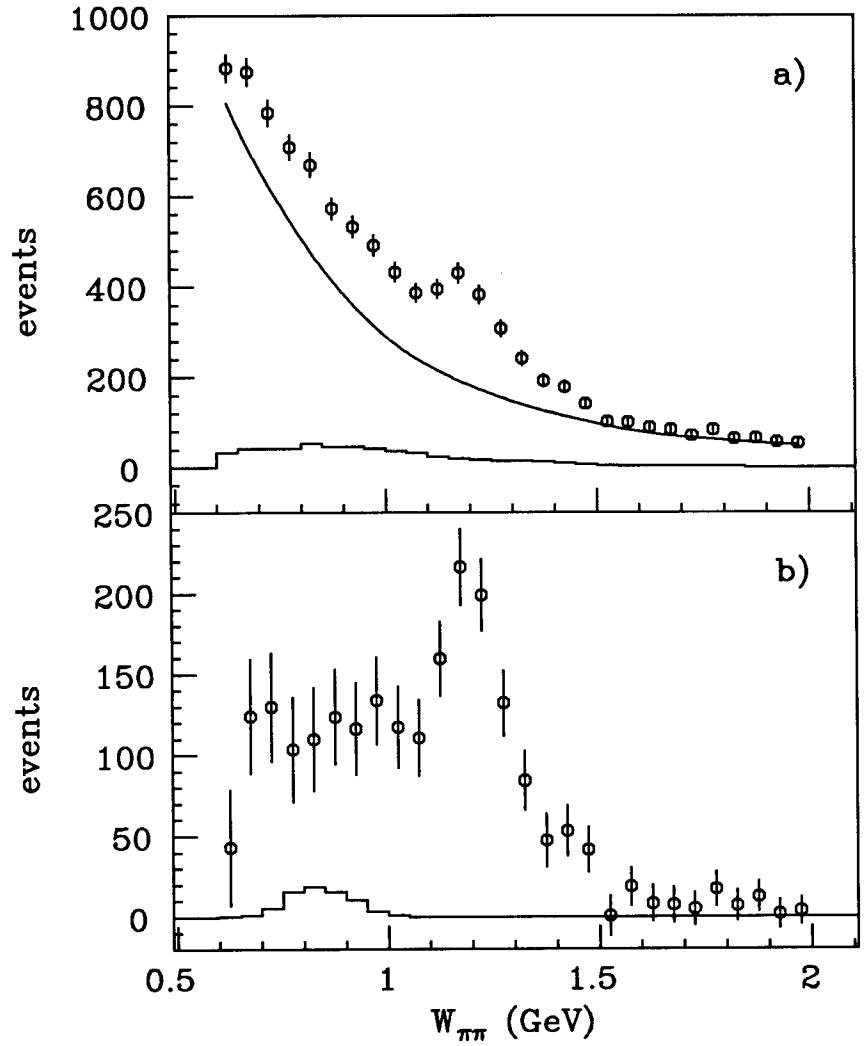

Figure 5.11. The invariant mass spectrum for tagged non-electron pairs. (*a*) The points represent the measured data, the smooth curve is the prediction for the $\mu^+\mu^-$ background, and the histogram drawn as a line is the estimated of the random background, obtained from the spectrum of pairs with nonzero charge. (*b*) The points represent the $\pi^+\pi^-$ spectrum obtained by subtracting all background. The histogram around the ρ^0 mass is the calculated background from η' production.

6. Measurement of the $\pi^+\pi^-$ Trigger Efficiency

A good understanding of the trigger efficiency for electrons and muons has allowed an accurate subtraction of the background from the sample of non-electron pairs. But before any information can be extracted from the resulting $\pi^+\pi^-$ spectrum, it must be corrected for the trigger inefficiency of pion pairs. The necessary correction differs from that calculated for muon pairs because of nuclear interactions of the pions with material between the beam-line and the scintillators of the shower counters. In order to latch a shower counter, an incident pion, or its decay or reaction products, must penetrate, when at normal incidence, roughly 6 cm of aluminum, which is 0.15 nuclear interaction lengths, followed by 2.5 cm of lead, which also is 0.15 nuclear interaction lengths. It is apparent that a significant fraction of the pions must undergo some sort of inelastic nuclear interaction, but it is impossible to make a simple estimate of the effect on the trigger efficiency. The best approach is to try to measure it from data, as has been done for the electron pairs.

6.1 Shower Counter Latch Efficiency from Tagged Data

It is unfortunate that there is no trigger redundancy to exploit in the sample of untagged non-electron pairs, but it is possible to use tagged data for measuring the shower counter latch efficiency, albeit with less statistical significance. The luminosity counter tag in coincidence with a single shower counter latch provides an LS trigger, which is partially redundant to the 2S trigger. Since in all cases at least one shower counter is required to latch, then it is necessary, as in the analysis of the electron pairs, to unfold the true efficiency from the trigger-biased efficiency plotted from data. However, there is an additional problem in this case which even further reduces the statistical significance of the measurement. About 3/4 of the non-electron sample consists of muon pairs, so their contribution must be accounted for when unfolding the pion shower counter latch efficiency from the data.

In this chapter we are concerned only with the inefficiency caused by pions stopping before reaching the second layer of scintillator—inefficiency due to gaps between counters already has been accounted for. It is useful to review why that is so. Recall that for non-electron pairs, no cut is made on the extrapolation of the drift chamber tracking information out to the shower counter region. To do so would cause errors due to limitations of the survey accuracy and tracking resolution and to multiple scattering in material preceding the shower counters. Survey and tracking errors cancel when normalizing pions and muons to the electron measurement, but scattering, which may include nuclear interactions, and electromagnetic showers depend on the particle type.

The problem of electromagnetic showers is resolved by analyzing the electron pairs, for the purpose of normalization, within a fiducial cut placed 4 cm from the edges of the shower counter modules. For that it still is necessary to use the tracking information, but the cut is far enough from the edge that the errors have no effect. For non-electrons, no cut at all is made on the tracking information; the acceptance simply is defined by the trigger, which requires both particles actually to latch a shower counter. Thus,the geometric acceptance is guaranteed to be the same for pions as for muons. Even though pions may scatter more than muons, because of nuclear interactions, just as many must scatter into the acceptance as scatter out, so that is not a problem. There may be a slight difference coming from inelastic nuclear interactions of pions in the aluminum adjacent to the shower counters, but it must be a much smaller effect than for electromagnetic showers. That is because whereas every electron hitting the aluminum produces a shower, only a small fraction of the incident pions produce a nuclear or electromagnetic avalanche. Such effects change the acceptance for electrons by only a couple of percent, so they are believed to be negligible for pions.

Therefore, the effect of nuclear interactions on the pion efficiency can be analyzed completely separate from edge effects. To do so requires making a fiducial cut inside the shower counters, and as one can see from Fig. 6.1, a 4-cm cut is

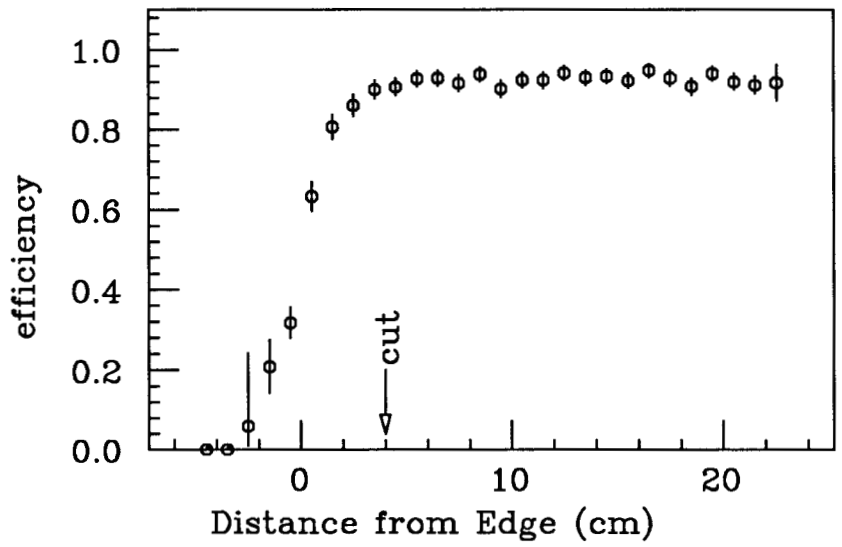

Figure 6.1. Resolution of the shower counter edge for non-electron tracks. The shower counter latch efficiency for each particle from tagged non-electron pairs is plotted as a function of the measured distance from the nearest edge of the counter.

adequate. Except for the region within 4 cm of the counter edge, the efficiency is flat, and the only explanation for the cause of the observed inefficiency is that a fraction of the *pions* in the sample are stopped before traveling far enough to latch a counter.

To produce efficiency plots from data, tagged events are analyzed just as in Chapter 4, except that some cuts are made on the time-of-flight information in order to reject kaon and proton pairs. Since kaons and protons range-out with lower initial momentum than do pions and muons, their presence could confuse the efficiency measurement. Both tracks in each event are required to be within the acceptance of the time-of-flight system, as determined from tracking information. It is not possible to cut on the timing information of all tracks, however, because to do so would require all particles to produce a significant signal in the time-of-flight counters. Since almost half of the material of concern here, in units of nuclear interaction lengths, is in front of the time-of-flight system, that would cause a large bias in the result. However, it is possible to reject those events with

particles which do have good times and are consistent with being kaons or protons, and doing so removes most of the problem. Of the non-electron tracks with good timing information, 2.1% are kaon or proton candidates, compared with 0.06% for the electron sample. The remaining number of kaons and protons is too negligible to have any noticeable effect on the efficiency plot.

From the resulting sample of non-electron pairs, a histogram of the shower counter latch efficiency is accumulated using all those tracks which satisfy the 4-cm fiducial cut, resulting in the 12,175 entries shown in Fig. 6.2. Using the electron pairs for normalization, the fraction of muon pairs in the sample is determined to be $0.72 \pm 0.02\%$. Their contribution to the efficiency plot is calculated by using the Vermaseren Monte Carlo and the efficiency parameterization given in Fig. 5.5. Recall that for muons the efficiency is 100% for momenta well above 0.18 GeV, below which they range out before reaching the second layer of scintillator (see Fig. 5.5). Well above that threshold, the only conceivable source of inefficiency is from light collection and the electronics. That possibility is removed by analyzing events from the reaction $e^+e^- \rightarrow \mu^+\mu^-$, for which the muons always are above Čerenkov threshold and therefore have redundant triggers. Of 3379 such muons which satisfy the 4-cm fiducial cut on the shower counters, only three fail to latch a shower counter. Thus the counters are essentially 100% efficient for single minimum-ionizing particles which actually pass through the scintillators.

In order to model the contribution of pions, the form used to parameterize their shower counter latch efficiency is

$$\varepsilon(p) = 0.995 \cdot \left[1 - 0.6 \cdot \exp\left(-\frac{p - 0.177}{0.0219}\right)\right] \times \left[1 - 0.6 \cdot \exp\left(-\frac{p - p_0}{\tau}\right)\right] . \quad (6.1)$$

The first exponential factor serves to produce the sharp cutoff due to electromagnetic range-out, and the second is adjusted to reproduce the efficiency observed in the data. For the same reasons as in the measurement of the electron efficiency, it is only necessary to parameterize the momentum dependence. However, one must

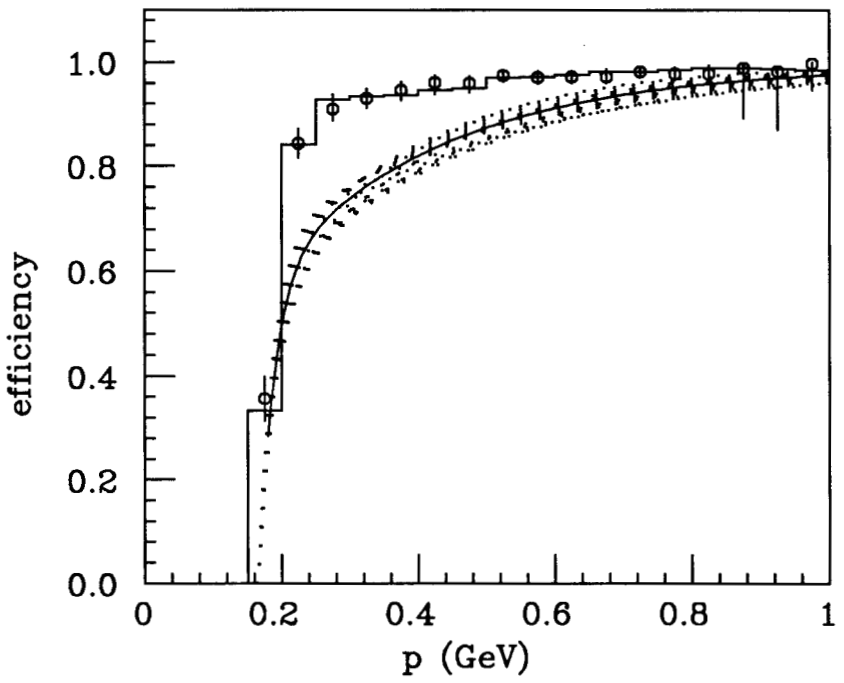

Figure 6.2. The shower counter latch efficiency for non-electrons as a function of the particle momentum. The points with error bars are measured from the tagged non-electron pairs, and the overplotted histogram is the best fit from a Monte Carlo calculation. The solid smooth curve is the parameterization used in the Monte Carlo for the pion shower counter latch efficiency, and the dotted curves show the range of uncertainty in the fit.

be sure that the Monte Carlo reproduces reasonably well the actual momentum distributions for the pions, so that the trigger bias is accurately reproduced. That is accomplished by using the $\gamma\gamma$ luminosity function appropriate for single tagged events in conjunction with the model for $\gamma\gamma \rightarrow \pi^+\pi^-$, which is introduced in Chapter 7.

The fitting procedure begins with generation of an efficiency histogram with 35,000 entries from Monte Carlo muon pairs. Then the pion-pair Monte Carlo is run, and for each of 100 pairs of trial values for p_0 and τ of Eqn. 6.1, an efficiency histogram is produced by adding 13,611 pion entries to the existing muon histogram. Comparing the 100 Monte Carlo histograms with the one from data produces a 10×10 matrix of χ^2 values. Those entries which are no more than

one unit of χ^2 above the minimum roughly form an elongated ellipse, showing an expected large negative correlation between p_0 and τ. The center of the ellipse ($p_0 = 0.070$, $\tau = 0.270$) is taken as the best fit and the resulting efficiency curve is shown as the solid smooth curve of Fig. 6.2. The set of dotted curves represent the pairs of values forming the perimeter of the ellipse and therefore indicate the one-standard-deviation uncertainty limits of the efficiency measurement.

This result includes, in addition to losses from nuclear and electromagnetic interactions, some losses resulting from those weak decays of pions which occur after leaving the inner tracking chambers. However, one expects the effects of such decays to be small. In fact, when pion decays are added to the Monte Carlo simulation, which does not include nuclear interactions, the detection efficiency decreases overall by less than 1.5%. With nuclear interactions included, the effect could be of the opposite sign. Because of the small difference in mass between the pion and muon, such decays usually result in a muon going in about the same direction as the initial pion. Therefore, it is conceivable that decays could actually increase the trigger efficiency, since the latch efficiency for muons is very high. Whatever the case may be, the effect is almost negligible and most of it already is included in the efficiency measurement. The remaining effect from decays which occur within the tracking volume and result in a loss of the track itself is negligible.

6.2 Calculation of the Shower Counter Latch Efficiency

It is worthwhile to attempt a direct calculation of the pion shower counter latch efficiency just to check that what has been measured makes physical sense. However, the result of the calculation cannot be expected to agree with the data to the extent that the EGS calculation reproduces the electron shower counter latch efficiency. In the electromagnetic case the details of the physical processes are well known, but for nuclear interactions one must rely on relatively crude models which try to reproduce features of physical processes which are not so well understood and which are great in variety. Furthermore, a determination of the

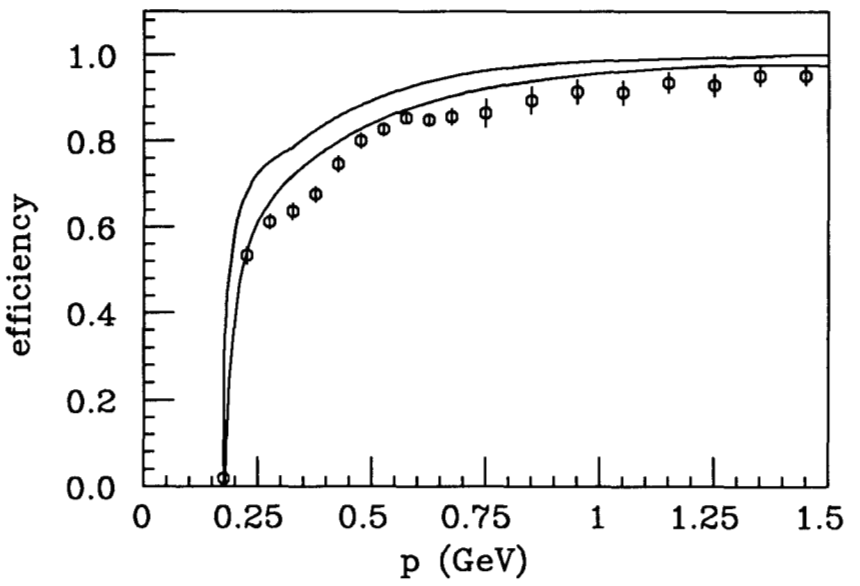

Figure 6.3. HETC calculation of the shower counter latch efficiency for pions. The points show the results of two HETC calculations, covering two momentum ranges, and the smooth curves show the range of uncertainty in the measurement from data, including both the statistical uncertainty and the uncertainty in the normalization of the muon contribution.

latch efficiency requires a very detailed calculation, because it takes only one of many possible charged particles produced from a reaction to latch a counter.

HETC[30] is used along with the EGS[29] code to simulate nuclear and hadronic interactions in the detector material. EGS is called only when a π^0 is produced from a nuclear interaction. HETC uses what is called the *Intermediate Energy Intranuclear-Cascade-Evaporation Model* for pion-nucleus inelastic collisions (except for πp reactions, which are not relevant here). Running the Monte Carlo model for $e^+e^- \rightarrow e^+e^-\pi^+\pi^-$ with the HETC-EGS simulation results in the histogram of Fig. 6.3. The efficiency from the calculation is consistently a little low, but it does show the same trend as what is observed in the data.

Since the HETC calculation does reproduce the general features of the inefficiency seen in the data, it is interesting to look a little more deeply into

the calculation to see what types of physical processes are responsible for the loss of efficiency. One finds that a few of the pions which fail to latch a shower counter have undergone a charge exchange reaction such as $\pi^- p \rightarrow \pi^0 n$, and the resulting electromagnetic shower has not penetrated far enough. Then there are a few other low-multiplicity reactions for which a neutron has carried off most of the momentum. However, most of the cases of latch failure are due to reactions in which several protons and neutrons more-or-less share equally the momentum in the final state. The neutrons seldom produce any interactions in the scintillators, and the protons typically do not have enough momentum to penetrate through much lead. In general, the reactions responsible for the loss of efficiency are, at least in the Monte Carlo, quite complicated, and the result of whether the reaction products can latch the counter depends critically on how the momentum is distributed among the protons and pions of the final state. Therefore, it is enough to conclude that the calculation does verify the momentum dependence, and approximately the magnitude, of the inefficiency seen in the data—the measurement is what is actually used in the following analysis.

6.3 Trigger Efficiency for Pion Pairs

When fitting the invariant mass spectrum of the pion pairs to a model, it is necessary to know the uncertainty in the trigger efficiency as a function of the pion-pair invariant mass. That is obtained by using the Monte Carlo to transform the upper and lower limits on the shower counter latch efficiency, shown in Fig. 6.2 as functions of momentum, into upper and lower limits on the trigger efficiency. It also is necessary to include the uncertainty from the normalization of the muon Monte Carlo, as obtained from the electron-pair measurement. If ε is the efficiency measured for the sum of pions and muons, and f is the fraction of muons, then the efficiency of the pions alone is approximately

$$\varepsilon_\pi = \frac{\varepsilon - f}{1 - f} \,. \tag{6.2}$$

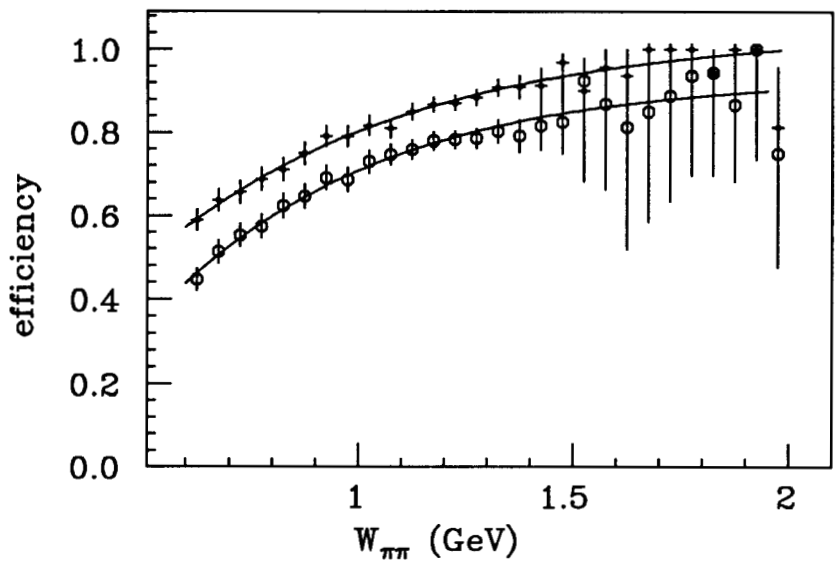

Figure 6.4. The pion-pair trigger efficiency as a function of invariant mass. The upper and lower sets of points, through which smooth curves are drawn, are generated by Monte Carlo, using as input the measured upper and low limits of the shower counter latch efficiency.

Using the predicted fraction f for each momentum bin along with the estimated 2.9% uncertainty in f, this equation is used to find the error in ε_π for each bin. That error actually already is included in the limits shown by the contours in Fig. 6.3, and using those contours in the Monte Carlo produces the result shown in Fig. 6.4. The percent difference between the two curves gives the uncertainty in the efficiency measurement for each invariant-mass bin. It can be adequately parameterized as a parabola with zero slope at the upper end of the mass range:

$$\varepsilon(W) = \varepsilon_1^\pi \left[\frac{a - \frac{a^2}{2b} - W + \frac{1}{2b}W^2}{a - \frac{a^2}{2b} - \frac{1}{2}b} \right] + \varepsilon_2^\pi \left[\frac{-\frac{1}{2b} + W - \frac{1}{2b}W^2}{a - \frac{a^2}{2b} - \frac{1}{2}b} \right], \tag{6.3}$$

where $a = W_1 = 0.6\,\mathrm{GeV}$, $b = W_2 = 2.0\,\mathrm{GeV}$, $\varepsilon_1^\pi = 0.10$, and $\varepsilon_2^\pi = 0.05$. When fitting the model for $\gamma\gamma \to \pi^+\pi^-$ to the $\pi^+\pi^-$ invariant-mass spectrum (Chapter 8), Eqn. 6.1 with $p_0 = 0.070$ and $\tau = 0.270$ is used in the Monte Carlo for the pion shower counter latch efficiency, while Eqn. 6.3 gives the uncertainty in the pion-pair detection efficiency.